GAS BARRIER AND SEPARATION BEHAVIOR OF LAYER-BY-LAYER ASSEMBLIES

A Dissertation

by

PING TZENG

Submitted to the Office of Graduate and Professional Studies of
Texas A&M University
in partial fulfillment of the requirements for the degree of

DOCTOR OF PHILOSOPHY

Chair of Committee,	Jaime C. Grunlan
Committee Members,	David Bergbreiter
	Jodie Lutkenhaus
	Victor Ugaz
Head of Department,	M. Nazmul Karim

May 2015

Major Subject: Chemical Engineering

ABSTRACT

Thin films with the ability to control gas permeability are crucial to packaging and purification applications. The addition of impermeable nanoparticles into neat polymers improves barrier/separation properties by creating a tortuous pathway, but particle aggregation occurring at high filler loading can reduce transparency of these composites as well as barrier/separation improvement. Layer-by-layer (LbL) assembly allows full control of morphology at the nanoscale, so barrier/separation properties can be precisely controlled and the films remain flexible and transparent.

A three component recipe, consisting of polyvinylamine, poly(acrylic acid) and montmorillonite clay was deposited as repeating PVAm/PAA/PVAm/MMT quadlayers (QL) via LbL assembly. By adjusting solution pH and varying the placement of polycation layers, polymer interdiffusion and clay concentration were controlled, as well as oxygen barrier.

Another QL assembly, with a PEI/PAA/PEI/MMT repeating sequence, was deposited using LbL to create light gas barrier films. Transmission electron microscope images revealed a highly-oriented nanobrick wall structure. A 5 QL coating on 51 µm polystyrene (PS) is shown to lower both hydrogen and helium permeability three orders of magnitude relative to bare PS, demonstrating better performance than ethylene vinyl-alcohol (EVOH) copolymer film and even metallized plastic.

Graphene oxide sheets, along with chitosan and PAA were used in a CH/PAA/CH/GO QL assembly. pH deviation between CH and PAA ionizes the counter ion, creating a more interdiffused polymer matrix and resulting in higher GO loading. Thermal reduction of GO, provides improvement in barrier performance under humid conditions and better H_2/CO_2 separation behavior.

Finally, a PEI/PAA multilayer membrane exceeding that of the current state-of-the-art gas separation membranes was performed. This ionically crosslinked assembly exhibits H_2/N_2 and H_2/CO_2 selectivities beyond Robeson's upper-bound limit, which are superior to the properties of most organic, inorganic or mixed-matrix membranes reported in the open literature, making it a significant advance in polymeric membranes for gas separation.

In conclusion, barrier and separation behavior were improved via either a polymer-polymer or polymer-nanoplatelet assembly. Several treatments, including interdiffusion or thermal reduction proved to enhance film performance. Future works focus on applying LbL techniques in Bragg reflectors and CO_2/N_2 separation.

DEDICATION

I dedicate this dissertation to my dearest parents and grandparents. Thank you for keeping me happy and motivated throughout my entire life.

ACKNOWLEDGEMENTS

I would like to thank my committee chair, Dr. Jaime Grunlan, who gives me such a great opportunity to work on gas barrier and separation projects, which furnished my research life with continuous excitement and challenges these past few years. Thanks also go to my committee members, Dr. David Bergbreiter, Dr. Jodie Lutkenhaus, and Dr. Victor Ugaz, for their guidance throughout the course of this research.

Thanks also go to my colleagues in the Polymer Nanocomposite laboratory. Former graduate students Morgan Priolo, You-Hao Yang, Amanda Cain and the rest of the current PNC group members for giving me great help and support in both work and life. Most importantly, I would like to acknowledge four of my talented undergraduate students (Cale Maupin, Travis Wilson, Garret Mai and Ian Devlaming). Without their contributions I could not finish my degree in such an efficient and successful manner. I am also grateful for the opportunity to collaborate with Dr. Benjamin Wilhite's group, including Dr. Daejin Kim, Elva L. Lugo, Xiaohong Cui and Stuart Powell.

Finally, I want to give my greatest appreciation to my family and friends who support me with endless love and encouragement, especially my roommate Chao-Cheng Shiau who I spent most of my time with. I would also like to thank my friends Yan-Ru Lin and Min-Chi Hsieh, for supporting me through my ups and downs, may dear Emily grow up as a kind and honest soul like you two. Without all the people mentioned above, I would not be able to finish this journey in pursuit of the Ph.D. degree.

NOMENCLATURE

AFM	Atomic Force Microscopy
Al_yO_z	Aluminum Oxide
ARS	Angle Resolved Spectrophotometry
ASTM	American Society for Testing and Materials
BAHF	Fluoroisopropylidene Dianiline
BL	Bilayer
BTDA	Benzophenonetetracarboxylic Dianhydride
CH	Chitosan
CMS	Carbon Molecular Sieves
CNCs	Cellulose Nanocrystals
DOI	Degree of Ionization
EVOH	Ethylene vinyl alcohol
FDA	Fluoroisopropylidene Diphthalic Anhydride
FTIR	Fourier Transform Infrared Spectroscopy
GO	Graphene Oxide
LB	Langmuir-Blodgett
LbL	Layer-by-Layer
MMM	Mixed Matrix Membrane
MMT	Montmorillonite
MOFs	Metal Organic Framworks

MRT	Magnetic Resonance Imaging
OPP	Oriented Polypropylene
OTR	Oxygen Transmission Rate
PAA	Poly(acrylic acid)
PAH	Poly(allylamine hydrochloride)
PAm	Polyacrylamide
PBI	Polybenzimidazole
PC/pNA	Polycarbonate/p-nitroaniline
PDA	Phenylenediamine
PDDA	Poly(dimethyldiallylammonium chloride)
PDMS	Polydimethylsiloxane
PE	Polyethylene
PECVD	Plasma-Enhanced Chemical Vapor Deposition
PEG	Polyethyleneglycol
PEI	Branched Polyethylenimine
PEN	Polyethylene Naphthenate
PEO	Poly(ethylene oxide)
PET	Poly(ethylene terephthalate)
PI	Polyimide
PIM	Polymer of Intrinsic Microporosity
PLA	Poly(lactic acid)
PMAA	Poly(methacrylic acid)

PMP	Poly(4-methyl-1-pentene)
PP	Polypropylene
PS	Polystyrene
PSS	Poly(styrene sulfate)
PTMSP	Poly(1-trimethylsilyl-1-propyne)
PVAm	Polyvinylamine
PVC	Polyvinylchloride
PVD	Physical Vapor Deposition
PVDC	Polyvinylidene Chloride
QCM	Quartz Crystal Microbalance
QL	Quadlayer
RI	Refractive Index
Room Temperature	RT
SEM	Scanning Electron Microscopy
SiO_X	Silicon Oxide
SiO_2	Colloidal Silica
SPM	Scanning Probe Microscopy
TEM	Transmission Electron Microscopy
T_g	Glass Transition Temperature
VMT	Vermiculite
WPO	World Packaging Organization
WVTR	Water Vapor Transmission Rate

TABLE OF CONTENTS

Page

LIST OF FIGURES

Page

LIST OF TABLES

Page

CHAPTER I

INTRODUCTION

1.1 Background

Polymer membranes are used in various technological areas such as water filtration,[1-3] fuel cells,[4-6] antireflection coatings,[7-9] optoelectronic devices,[10-12] tissue repair,[13-15] food packaging[16-18] and gas separation.[19-21] One of the most important properties of these membranes is the ability to control gas permeation rate, with the driving force being pressure or concentration. While conventional gas separation techniques (e.g., cryogenic distillation or an adsorption process) involve tremendous energy consumption, membrane gas separation does not require a phase change, making it more energy efficient.[22, 23] Membranes also allow gas separation to be performed in remote locations due to the absence of moving parts.[22] This growing technological area is competitive because of its simplicity, low energy cost, portability, reliability and space efficiency, which is why the market for membranes is expected to quintuple from 2000 to 2020.[23]

While separation membrane is able to permeate gases selectively, barrier films are designed to block a specific penetrant. Packaging materials made with various barriers play a significant role in modern society. Food, beverages, cosmetics, pharmaceuticals and electronics all require good gas and moisture protection.[16, 24] According to the World Packaging Organization (WPO), global packaging sales increased from 372.4 to 563.9 billion dollars from 1999 to 2009.[25] Plastic packaging materials such as polyethylene (PE), polypropylene (PP), polyvinylchloride (PVC) and polyethylene terephthalate (PET) are extensively used for making containers, lids, pouches, and films due to their barrier properties, mechanical flexibility and price.[26, 27]

Of all the membrane materials (polymer, inorganic and mixed matrix), mixed matrix composite membranes combine material types to fine-tune the properties, along with controlling the morphology of the membrane.[22, 28, 29] Despite the commonly used thin film preparation techniques such as plasma enhanced chemical vapor deposition (PECVD)[30, 31] or solvent casting,[32, 33] layer-by-layer assembly (LbL) continues to grow in popularity (since the 1990s)[34] due to its simplicity and versatility. By alternately exposing a substrate to oppositely-charged polyelectrolyte solutions, electrostatic attractions between the charged ingredients result in the buildup of anion/cation bilayers (BL), as shown in Figure 1.1. Film thickness and other properties can be easily controlled by increasing the number of deposition cycles, and although rinsing and drying steps are often used between deposition steps, they are optional. To produce functional polymeric thin films with unique structures and properties, one can achieve these goals through adjusting concentration,[35, 36] pH/ionic strength,[37-39] temperature,[38, 40] molecular weight[41, 42] and deposition time[35, 43, 44] of the aqueous deposition mixtures. In addition to electrostatic attraction,[45] hydrogen bonding[46] and covalent bonding[47] can also be used in a layer-by-layer fashion. The LbL technique has also been demonstrated for integrating multiple polymers,[44, 48] incorporating nanoparticles,[49, 50] inorganic clays,[51, 52] and biological molecules.[45, 53] All the advantages mentioned make

LbL assembly a promising candidate for drug delivery,[54-56] antireflection,[57-59] flame retardant,[60-62] and gas barrier/separation [63-65] layers.

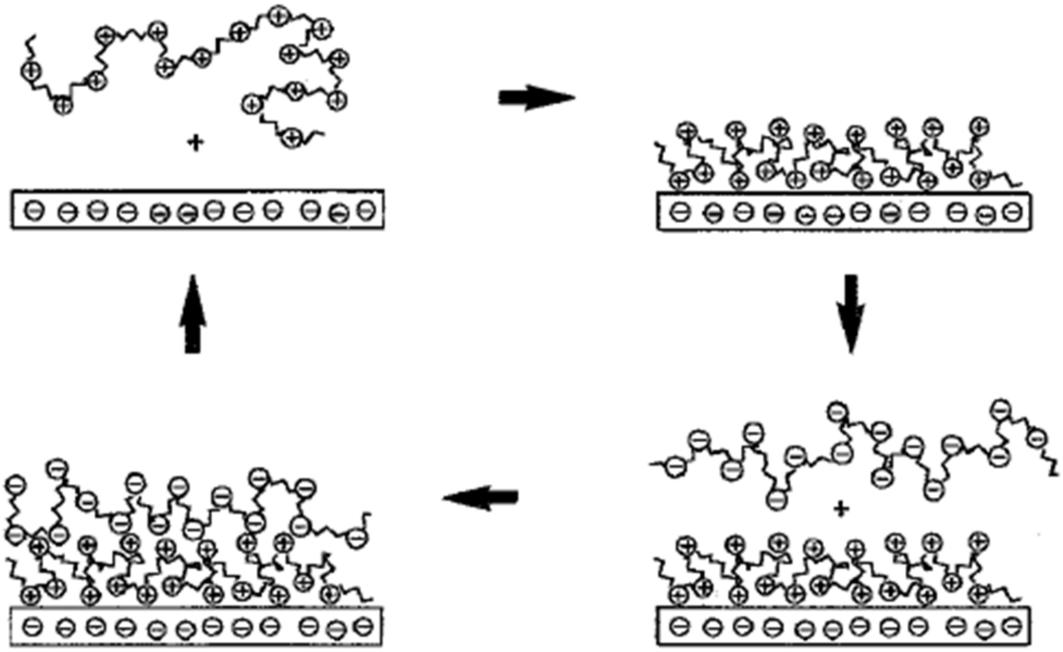

Figure 1.1. Schematic of the layer-by-layer deposition process.[44]

1.2 Objectives and Dissertation Outline

The objective of this dissertation is to understand how layer-by-layer systems (all-polymer and polymer-nanoplatelet) perform as either gas barrier or gas separation films. By creating more interactions in the thin film and increasing the distance of the molecular diffusion path, diffusivity of gas through the multilayer assemblies is effectively suppressed (while solubility remains unchanged), which reduces gas permeability. Thin film structure can also be fine-tuned to allow smaller gases to permeate through, creating a gas separation film. In this dissertation, the capability of improving gas barrier and separation properties via LbL coatings, with varying recipes and processing parameters, is demonstrated. These all-polymer and polymer-nanoplatelet assemblies create a highly impermeable/selective nanocoating that can be used for packaging (e.g., food and electronics) and gas purification.

Chapter II is a concise review of gas transport mechanisms, barrier/separation technologies and layer-by-layer assembly. The first part elaborates gas transport in polymer and nanocomposites, followed by the theoretical models used to describe these transport phenomena. The second part of the chapter covers gas barrier and separation films that have been studied, including polymer, inorganic and mixed matrix membranes. The last part illustrates the basics of LbL assembly, with special emphasis on gas barrier and separation behavior.

Chapter III describes the ability of LbL processing to tailor gas barrier of polymer-clay thin films. A three component recipe, consisting of polyvinylamine (PVAm), poly(acrylic acid) (PAA) and montmorillonite (MMT) clay was deposited as repeating PVAm/PAA/PVAm/MMT quadlayers (QL). This QL assembly demonstrates the influence of polymer interdiffusion and clay concentration on oxygen barrier behavior. With the aid of ellipsometry and quartz crystal microbalance (QCM), it was confirmed (by varying the placement of PVAm and polyethylenimine (PEI) layers) that these QL assemblies can be switched from linear to exponential growth with greater clay deposition in each layer. Atomic force (AFM) and transmission electron microscope (TEM) images also revealed a high level of clay orientation. Oxygen transmission rate (OTR) testing was performed on coated poly(ethylene terephthalate) (PET) to analyze barrier behavior as a function of polymer interdiffusion and clay concentration.

Chapter IV is an extension of Chapter III and previous work done to investigate the light gas barrier of PEI/PAA/PEI/MMT QL thin film.[66] Cross-sectional TEM images were used to examine the nanobrick wall structure while increasing the number of QLs deposited. TEM images and QCM confirmed the decrease of clay concentration as the assembly grew thicker. Hydrogen and helium transmission rate testing was performed on coated polystyrene (PS) to evaluate the influence of the number of QL deposited on barrier properties.

Chapter V describes a chitosan (CH)/PAA/chitosan (CH)/graphene oxide (GO) QL system. The influence of CH and PAA solution pH on growth, structure, polymer interactions and barrier was investigated. Ellipsometry and QCM were used to measure the growth and mass deposition as a function of QL deposited and polyelectrolyte pH, and to calculate composition of GO in these assemblies. Scanning electron microscopy (SEM) and cross-section TEM were used to examine film structure and coverage of GO on top of polymer layer. Fourier transform infrared (FTIR) spectra confirmed the level of CH/PAA interaction for each assembly. OTR of the coated PET assemblies were measured under dry and humid condition with unmodified GO and thermally-reduced GO. Hydrogen and carbon dioxide transmission rates were also measured to quantify the separation behavior.

Chapter VI describes the exceptionally high hydrogen permselectivity and remarkable elastic modulus in an ionically crosslinked, LbL-assembled PEI/PAA membrane. These membranes perform beyond Robeson's upper-bound limit, despite being made of seemingly homogenous polymer. Nanoindentation was used to investigate mechanical behavior of these films. Cross-sectional SEM images were taken to confirm the uniformity over the substrate. Gas permeation testing allowed for comparison of PEI/PAA with other polymer and mixed matrix membranes.

Chapter VII is conclusions for this work and future research directions. This dissertation investigated the influence of polymer interdiffusion, nanoplatelet concentration and types of nanoplatelet on gas barrier and separation behavior. Tremendous properties were demonstrated, but these multilayer assemblies are currently unable to separate gas pairs with similar molecular sizes. In order to improve selectivity, materials such as polyethylene oxide (PEO) are introduced into the assembly to increase solubility of specific gas (i.e., carbon dioxide). By varying the deposition solution pH, mechanical properties and PEO composition can be controlled, which alters permeability of different gas pairs and selectivity. The second work describes the use of LbL assembly to reproduce uniform and crack-free Bragg reflecting surfaces. The refractive index (RI) of each layer was designed by combining two materials in each layer. Thickness of each layer was then controlled by altering the number of BL in each layer. The high RI layer consisted of cationic PEI and anionic vermiculate clay (VMT), forming a dense layer. The low RI layer contained cationic colloidal silica (SiO_2) and anionic cellulose nanocrystals (CNCs). Due to the entirely different shape of SiO_2 and CNCs, a porous layer with low RI is created. Cross-sectional TEM images show well-defined high and low RI layers, which were found to have iridescent properties after six deposition cycles (containing hundreds of individual layers).

CHAPTER II

LITERATURE REVIEW

2.1 Gas Diffusion Theory

In order to design a gas barrier or gas separation film, one needs to understand gas transport phenomena through a polymer membrane. The first gas permeation analysis is attributed to Mitchell.[67, 68] He observed that natural rubber balloons filled with hydrogen gas deflated over time and reasoned this was due to diffusion of gas through the balloon wall. In 1866, Graham measured the permeation rate of all known gases on every polymer membrane available.[69] His work led to Graham's law of diffusion:

$$r \, \alpha \, 1/\sqrt{M} \tag{2.1}$$

where gas permeation rate r is inversely proportional to the root of molecular weight M of penetrant.

Two types of membranes are used to describe gas permeation: porous or dense. Figure 2.1 illustrates how gases permeate through these membranes. For porous membranes, the gas diffusion mechanism varies according to pore size.[70] If the pores are relatively large (0.1 – 10 µm), gases permeate through the membrane by convective flow and no separation occurs.[70] If the pore size is smaller than the mean free path of the gas molecules (< 0.1 µm), then permeation is dominated by Knudsen diffusion.[70, 71] In this case, penetrants follow the Graham's law. When the membrane pore size is below

10 nm, gases are separated by molecular sieving.[70] Gas transportation through this type of membrane is a combination of gas phase diffusion and surface diffusion.[72] Despite the research interest in these porous membranes, high cost and complicated processing limit their use, so most commercial gas separation membranes are the dense type. Layer-by-layer assembly belongs to the dense category, and is the focus of this dissertation, so porous membranes will not be further reviewed here.

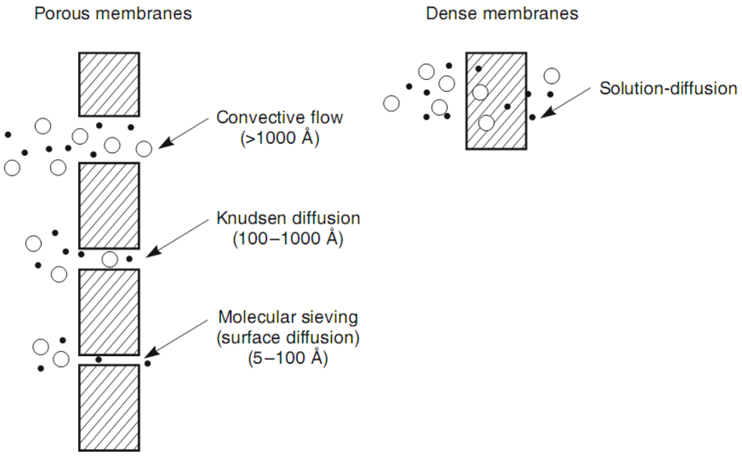

Figure 2.1. Mechanisms for permeation of gases through porous and dense separation membranes.[70]

2.1.1 Gas Transport through Polymer

Gas transport in nonporous dense polymer membranes is described by the solution-diffusion model. This model can be divided into five steps as depicted in Figure

2.2, which includes diffusion through the boundary layer at the upstream side, relative sorption of gases by the polymer membrane, diffusion of the gases inside the polymer membrane, desorption of gases at the permeate side, and diffusion out of the boundary layer of the downstream side.[73]

In 1866, Graham postulated basic expression representing the solution-diffusion mechanism through a polymer membrane:[69]

$$P = D \times S \tag{2.2}$$

where the gas permeability (P) (cm^3 cm cm^{-2} s^{-1} Pa^{-1}) is the product of diffusivity (D) (cm^2 s^{-1}) and solubility (S) (cm^3(273.15K; 1.013 × 10^5 Pa) cm^{-3} Pa^{-1}). Diffusivity is a kinetic factor that represents the ability of molecules to move through the polymer.[73] Larger penetrants generally have lower diffusivity, which is also sensitive to polymer chain flexibility and free volume in the polymer. Diffusivity can be defined by free volume theory:[74]

$$D = A\, exp(\frac{-B}{F}) \tag{2.3}$$

where A and B are constants of the specific gas-polymer system and F represents the fractional free volume:

$$F = \frac{V_{total} - V_{occupied}}{V_{total}} \tag{2.4}$$

where V_{total} is the sum of the theoretical volume of polymer ($V_{occupied}$) and the free volume in the system. Solubility, on the other hand, is a thermodynamic factor related to gas condensability (characterized by gas critical temperature, boiling point, enthalpy of vaporization, *etc.*) and gas-polymer interactions.[73] Solubility is related to local concentration (C) of the gas at a given temperature and is expressed as a function of pressure (p):

$$S = C/p \tag{2.5}$$

Larger penetrants are usually more condensable, resulting in higher local concentration and solubility. Definition of selectivity ($\alpha_{A/B}$) is the gas permeability ratio of A to B. It can be influenced by the differences in diffusivity or the differences in solubility:

$$\alpha_{A/B} = \frac{P_A}{P_B} = \left[\frac{D_A}{D_B}\right]\left[\frac{S_A}{S_B}\right] \tag{2.6}$$

The competition between diffusivity and solubility is determined by whether the polymer chains are at equilibrium, which will be explained in the next section.

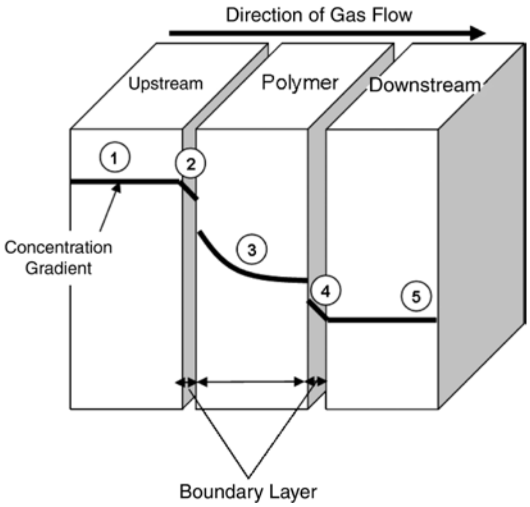

Figure 2.2. Schematic presentation of gas permeation steps across polymer membranes according to the solution-diffusion mechanism.[73]

2.1.1.1 Transport through a Rubbery Polymer

When gas molecules permeate through a polymer membrane, the interactions between the penetrant and polymer change the physical state of the polymer. Both diffusivity and solubility depend greatly on whether the polymer membrane is above or below its glass transition temperature (T_g).[75] If the polymer is at equilibrium at room temperature (RT) ($T_g < RT$), segments of polymer chains have sufficient thermal energy to allow limited rotation. This motion changes its mechanical properties, and the polymer is defined as rubber. Gas transport behavior in rubber can be sufficiently explained using the solution-diffusion model, as long as it doesn’t contain crystalline phase that acts as a barrier to the gas molecules.[26, 73] For rubbery polymers, the solubility term is usually dominant over diffusivity, so gas permeability increases with increasing penetrant size (without considering additional penetrant-polymer interactions).[76-78]

2.1.1.2 Transport through a Glassy Polymer

Gas diffusion in a glassy polymer ($T_g > RT$) is more complicated because the sorption sites are unique. For a glassy polymer, changes in gas permeability as a function of pressure is often explained by a dual-mode model, which was first proposed by Barrer[79] and later modified by Petropoulos and Koros.[80, 81] The basic assumptions of this model are: dissolution of gas in the polymer matrix by Henry’s law and adsorption of gas molecules in holes (or cavities) on the surface (or inside) the polymer matrix by Langmuir’s law. The pressure dependence of solubility can be described as:

$$S = k_D + \frac{C'_H b}{1+bp} \tag{2.7}$$

where k_D is Henry's law constant, C'_H is the Langmuir capacity constant, and b is the Langmuir affinity constant. C'_H indicates the level of unrelaxed free volume in the glassy polymer. This term is used to determine the nonequilibrium nature of glassy polymers. The affinity constant describes the specific nature of a given penetrant to sorb into the excess unrelaxed volume in the nonequilibrium glassy polymer matrix. It was found that the balance between the diffusivity term and the solubility term in Equation 2.6 is different for glassy and rubbery polymer.[78] The diffusivity term is usually dominant for a glassy polymer, so gas permeability decreases with increasing penetrant size. The nonequilibiurm state of glassy polymers can also be affected by process parameters such as temperature, pressure and penetrant-polymer interactions.[73]

2.1.2 Transport in Nanocomposites

Nanocomposites are two phase systems that consist of a polymer matrix and dispersed particles of nanometer scale. Adding inorganic nanoparticles into a polymer matrix has been shown to successfully increase elastic modulus. The coupling between large surface area nanoparticles and a polymer matrix facilitates stress transfer to the reinforcing phase, so tensile strength and toughness are also increased.[82-85] These impermeable nanoparticles can also increase flame retardancy of the polymer matrix,[86-88] while also forming a tortuous pathway to reduce gas permeability.[89-91] The most common nanoparticles belong to the family of 2:1 phyllosilicates (i.e., clays). Their crystal structure, shown in Figure 2.3, consists of an aluminum or magnesium hydroxide octahedral sheet sandwiched between two silicon oxide tetrahedral sheets.[83, 92] The layer thickness of each clay platelet is 1 nm and their lateral dimensions vary from 30 nm to several microns, making the aspect ratio (α) range from 30 to several thousands.[85,93]

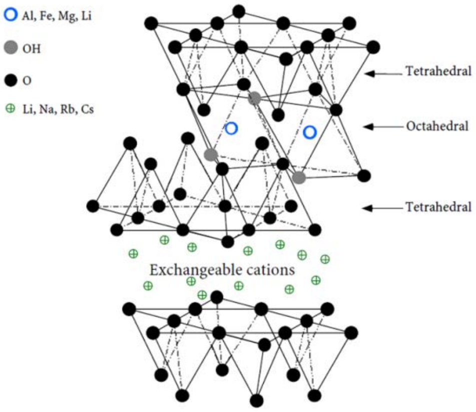

Figure 2.3. Montmorillonite clay chemistry and structure.[92]

Simple mixing of polymer and nanoplatelets does not always result in the generation of a nanocomposite, but rather the dispersion of larger stacked aggregates. This aggregation is due to the weak interactions between polymer and inorganic component, which results in poor properties relative to a fully exfoliated nanocomposite.[94] Depending on the strength of the interfacial interactions, three types of morphology are possible in polymer-clay nanocomposites:[95] (1) phase separated composite - clay platelets have the same basal plane spacing d_{001} as the theoretical value, suggesting the polymer chains did not enter the gallery of the platelets (Fig. 2.4a), (2) intercalated composite - d_{001} is increased by the entering polymer, but the clay platelets remain stacked in parallel with each other (Fig. 2.4b), and (3) exfoliated composite - d_{001} is greater than 10 nm, clay sheets are pushed apart irregularly by polymer or organic species (Fig. 2.4c). There are different factors controlling the extent of clay exfoliation, including concentration,[94] interfacial interactions[96] and temperature.[97]

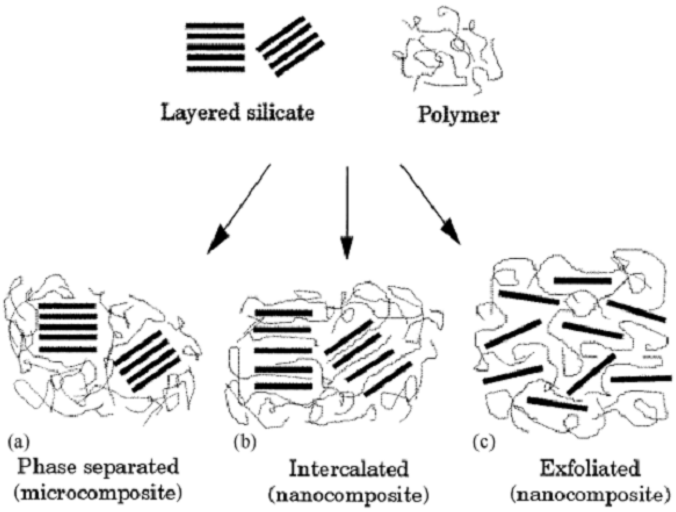

Figure 2.4. Schematics of the three different clay-filled composite morphologies.[95]

Gas diffusion through nanocomposites can be viewed as a solution-diffusion process. In the absence of adsorption by the filler, or effects of the filler on the surrounding polymer,[98] solubility of the composite can be described as:

$$S = S_0(1 - \phi) \tag{2.8}$$

where S_0 is the solubility of the pure polymer matrix and ϕ is the volume fraction of filler in the matrix. In this case, solubility does not depend on morphology of the polymer and the filler.[98] Diffusion is more complicated because fillers act as impermeable barriers and force penetrant to follow an elongated (tortuous) pathway to diffuse through the composite.

$$D = D_0 f \tag{2.9}$$

f is the tortuosity factor where D_0 is the diffusivity of the neat polymer. Tortuosity factor depends on the volume fraction of the filler, aspect ratio of the filler (α), and its orientation in the polymer matrix. Combining Equation 2.8 and 2.9 gives

$$P = DS = S_0 D_0 f(1-\phi) = P_0 f(1-\phi) \tag{2.10}$$

or

$$f = \frac{P}{P_0(1-\phi)} \tag{2.11}$$

where P_0 is the gas permeability of neat polymer. A simple permeation model for a regular arrangement of platelets has been proposed by Nielsen and is presented in Figure 2.5.[99] The platelets are evenly dispersed and considered to be rectangular with finite width (L) and thickness (W). Their orientation is perpendicular to the diffusion direction. Nielson also proposed that tortuosity (τ), the reciprocal of tortuosity factor, is a function of α ($= \frac{L}{2W}$) and ϕ:

$$\tau = 1 + \alpha\phi = 1 + \frac{L}{2W}\phi = \frac{1}{f} \tag{2.12}$$

Combining Equation 2.11 and 2.12, the gas permeability of nanocomposites becomes:

$$P = \frac{P_0}{\frac{1+\alpha\phi}{1-\phi}} \approx \frac{P_0}{1+\alpha\phi} \tag{2.13}$$

Nielsen's model describes a composite with low filler volume fraction ($\phi \ll 1$) which makes the filler in the composite a "dilute suspension". The denominator of Equation 2.13 can be simplified as shown above.

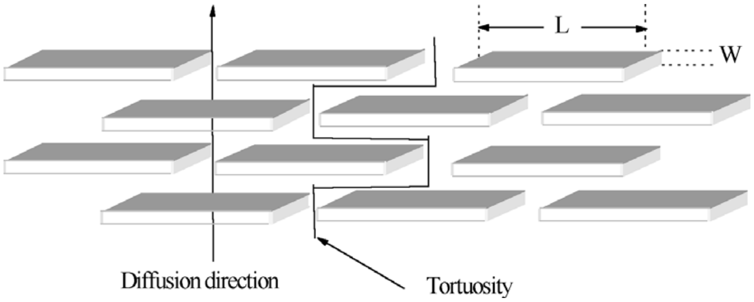

Figure 2.5. Schematic of gas transport through a polymer-platelet composite via a tortuous path.[99]

A more advanced tortuous path theory was later proposed by Cussler.[100] The difference between the Nielsen and Cussler models is the former failed to describe higher concentration regimes in the composite. Cussler's model states the relationship between the gas permeability of a filled polymer matrix and neat polymer as:

$$P = \frac{P_0}{1+\mu\alpha^2\phi^2/\left(1-\phi\right)} \tag{2.14}$$

where μ is a geometric factor representing the shape of the filler. It describes gas diffusion phenomena when the filler concentration in the composite is “semi-dilute” ($\phi \ll 1$ and $\alpha\phi < 1$).[90, 101] The distribution of platelets in a polymer composite can also affect gas permeability. When the platelets are in a regularly spaced array, μ = 1. When the platelets are in a randomly distributed array, μ = 4/9. These possible geometries of platelets in the composite are shown in Figure 2.6.

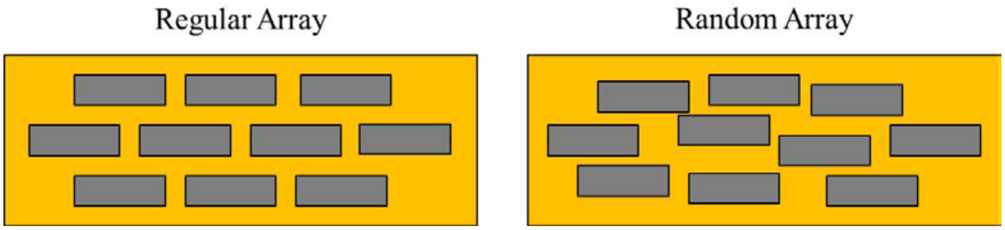

Figure 2.6. Geometries of regular and random arrays for platelet-filled polymer composites.

2.1.3 Limitations of Gas Separation Using Polymer Membranes

The best gas separation membrane should have high gas permeability and high selectivity. In reality, there are strong trade-offs between gas permeability and selectivity that are not easily broken.[102-105] It is believed that this trade-off behavior for specific gas pairs is unique and related to the nature of the gas molecules. Robeson proposed a selectivity-permeability relationship for polymer membranes and various gas pairs in

1991 and revised it in 2008.[20, 21] The transport parameters, selectivity ($\alpha_{A/B}$) and gas permeability (P_A), were plotted to generate an upper-bound line, Figure 2.7. In general, rubbery polymers have higher flux, while glassy polymers exhibit better selectivity. The following empirical equation was proposed to explain the upper-bound lines for given gas pairs:

$$log\alpha_{A/B} = log\beta_{A/B} - \lambda_{A/B} logP_A \tag{2.15}$$

where $\lambda_{A/B}$ is the slope of the upper-bound, which depends only on the size of the gas pair and $log\beta_{A/B}$ being the intercept at $logP_A$ = 0 (depends on gas condensabilities). Development of better membrane materials is an ongoing research topic, making further revision of the upper-bound necessary in the future.

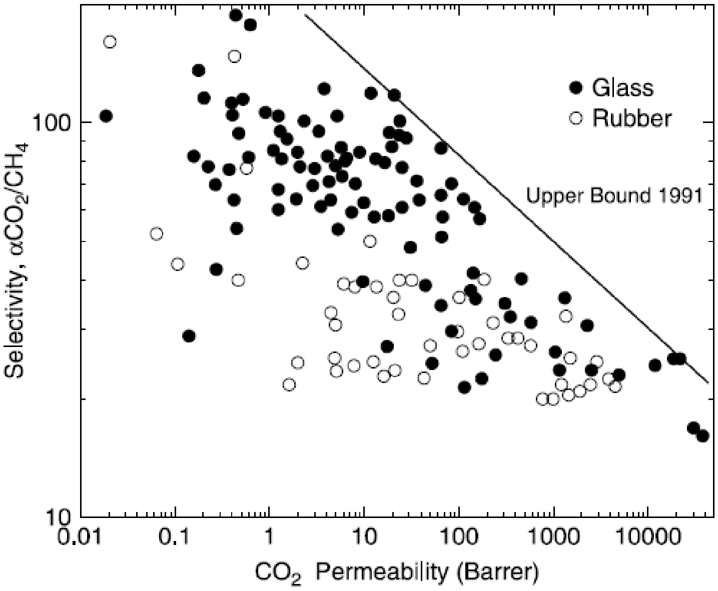

Figure 2.7. Upper-bound line of CO_2 permeability and CO_2/CH_4 permselectivity.[20]

2.2 Gas Barrier/Separation Films

Transparent and flexible thin films with high barrier properties are important for packaging. Lack of metallic components is also vital for microwavability and recyclability,[106] which explains the strong interest in using nanoplatelets as impermeable fillers.[107-110] In contrast, gas separation films require high flux and selectivity.[16, 70, 73] Flux can be increased by increasing surface area of the separation module, while selectivity is controlled by film structure and gas-polymer interactions.[23, 70, 111-113] These properties are necessary for packaging, electronic displays and gas purification/separation.[19, 22, 114-116] The gas barrier and separation technologies reviewed in this section have been developed to satisfy these applications. Polymer films, whether as a blend or bulk material, are the most studied and commonly used for barrier/separation application (see Section 2.2.1).[16, 117-119] A new approach for barrier/separation films is by depositing a thin barrier layer on top of the polymer substrate, which offers advantages such as light weight, low cost and design freedom.[116, 120] Inorganic films, which contain impermeable inorganic nanoparticles and polymer matrix have been studied for their low gas. The inorganic materials can be deposited on flexible substrate to reduce gas permeability (Section 2.2.2.1),[17, 121] used as a separation film itself (Section 2.2.2.1)[122, 123] or coated as a metal oxide layer (Section 2.2.2.2).[124-126] Finally, mixed matrix membranes combine the benefits of the previous systems (Section 2.2.3), enabling properties to be tailored by choosing the materials necessary and controlling the morphology of the membrane.[22, 28, 29, 127, 128]

2.2.1 Polymers

High barrier polymers, such as ethylene vinyl alcohol (EVOH), polyvinylidene chloride (PVDC) and polyethylene naphthenate (PEN), act as fillers when laminated with polymers like polyethylene (PE),[129] polypropylene (PP)[117, 130] and poly(ethylene terephthalate) (PET).[131] The gas barrier can be improved 2 to 10 times relative to the neat commodity polymer.[16] This improvement is not significant relative to other techniques, but inexpensive processing has made it one of the most prevalent forms of commercial packaging material.[27]

As for bulk polymer membranes, they made their debut in commercial gas separation in 1980. Starting with the hydrogen-separating Prism® (polysulfone), other membranes such as Cynara (cellulose acetate) and Separex (cellulose acetate) were introduced to remove carbon dioxide from methane in natural gas.[118, 132, 133] More recently, work by Dow, Ube and DuPont has expanded the market and made membrane separation more competitive than conventional gas separation techniques.[70] Other materials, such as silicon-based and high-temperature polymers have also been studied. Due to their chain flexibility, large free volume and low glass transition temperature (T_g of polydimethylsiloxane (PDMS) is -123°C), silicon-based polymers have high gas and vapor permeability.[134, 135] Their excellent thermal and chemical resistance is suitable for separation of high value organic vapors from industrial waste streams. For instance, a PDMS-blended membrane operating at 35 °C and 1 atm exhibited an oxygen permeability 250 times higher than polyimide membranes, while O_2/N_2 selectivity remained similar. High-temperature polymer membranes, such as polybenzimidazole

(PBI) or polyimides (PI), with T_g over 400 ^oC and decomposition temperature near 600 ^oC, have also received more attention.[136-139] High T_g polymer increase the operating temperature up to 300 ^oC, which increases flux while maintaining high selectivity (H_2/CO_2 = 20) relative to rubbery polymers, as shown in Figure 2.8.[73]

2.2.2 Inorganic Films

Two types of inorganic films will be introduced, the metalized films and metal oxide films.

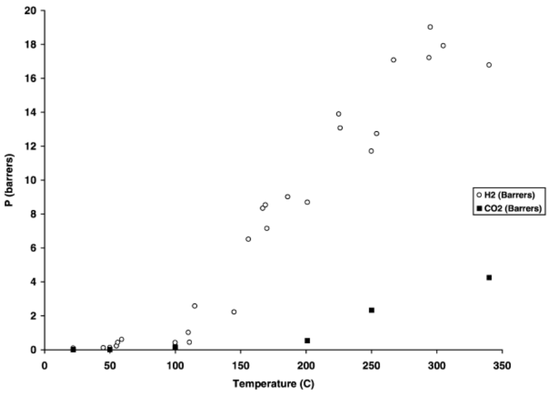

Figure 2.8. Permeance as a function of temperature for H_2 and CO_2 permeating through PBI membranes.[136]

2.2.2.1 Inorganic Films: Metalized Plastics and Metal Films

Traditional flexible barriers consist of polymer film with a thin layer of aluminum, ranging from ten nanometers to few micrometers.[17, 121, 140] Although metalized film provides barrier properties (oxygen transmission rate [OTR] = 1.4×10^{-14}

cm^3 cm^{-2} s^{-1} Pa^{-1}) unrivaled by any other flexible packaging, the smaller thickness is susceptible to the formation of pinholes and other stress induced fractures.[17] Additionally, metalized film cannot be recycled, is opaque and cannot be microwaved. It is for these reasons that eliminating the metal layer has become an important aspect of package design. Metal is also used in gas separation, mostly in high-temperature membrane reactors for the preparation of pure hydrogen.[141] For instance, hydrogen permeable palladium and its alloy membranes are extremely selective, with hydrogen permeability often 10-100 times higher than polymer membranes.[122, 123] These metal membranes must be operated at a high temperature (>300 °C) to obtain useful gas permeability and to prevent cracking by absorbed hydrogen, which limits their industrial applications.[142]

2.2.2.2 Inorganic Films: Metal Oxide Films and Ceramic/Zeolite Films

Thin glass-like metal oxide films can be produced by physical vapor deposition (PVD), or plasma-enhanced chemical vapor deposition (PECVD), to dramatically reduce gas permeability of polymer substrates, as shown in Table 2.1.[143-146] The development of these technologies started in the 1980s for PVD and 1900s for PECVD. Silicon oxide (SiO_x) and aluminum oxide (Al_yO_z) are the most commonly deposited materials, both of which are transparent, water-resistant, microwavable and exhibit barriers comparable to metalized films. Oxide layers are a foil (i.e., metal) replacement for food and pharmaceutical packaging.[124-126] Major problem with oxide layers are limited flexibility, poor crack resistance and the relatively high production costs.[147, 148] During the past few years, ceramic- and zeolite-based films have been used for commercial separations.[149, 150] These films consist of a selective ceramic or zeolite layer on a microporous support. Extraordinarily high selectivity (H_2/N_2 = 275) has been reported for these films.[150] Their ceramic nature allows operation at high temperature, which means high gas permeability during separation. Despite their promise, the cost of these films (\$3000/m^2), is currently too high to be commercialized for most applications.[23, 70]

Table 2.1 Oxygen transmission rates of bare and SiOx-coated polymer substrates.

Substrate	Coating		OTR ($cm^3\ m^{-2}\ day^{-1}\ atm^{-1}$)	Ref.
	Technique	Thickness		
Polyethylene (PE)	bare	12μm	8525	[143]
	PECVD	40nm	300	[143]
Oriented Polypropylene (OPP)	bare	25μm	2500	[143]
	PVD	70nm	218	[144]
	PECVD	90nm	9	[145]
Poly(ethylene terephthalate) (PET)	bare	12μm	120	[143]
	PVD	70nm	2.18	[146]
	PECVD	40nm	1	[143]

2.2.3 Mixed Matrix Membranes

The introduction of nanoparticles into a continuous polymer matrix has improved mechanical and thermal stability of conventional polymer membranes as well as their gas barrier/separation performance. Nanoparticles mixed within polymer matrix can be classified into two categories: porous particles, such as zeolites,[151, 152] and nonporous platelets, such as graphene-based materials and clay.[82, 128, 153, 154] The addition of nanoparticles can improve gas barrier and/or selectivity by increasing the diffusion pathway for gases, as shown in Figure 2.9.[127] Clay-filled polyurethane,[155] epoxy,[156] polyolefin,[157] polyamide[89] and biodegradable polymers[158] have all exhibited 50% to 90% improvement in barrier. As noted earlier, the simple mixing of polymer and nanoparticles does not always result in a nanocomposite. In the case of clay, this is due to the Na^+ and K^+ ions that are more compatible with hydrophilic polymers.[85] Nanoparticles also tend to aggregate when a threshold concentration is achieved (≤ 10wt %),[91] restricting the possibility for further barrier and separation improvement. Layer-by-layer assembly was proposed to solve this problem. The strong electrostatic interactions that accompany this deposition technique can efficiently decouple single clay platelets, allowing for the creation of dense composites with high concentration and exfoliation of nanoplatelets.[159]

Figure 2.9. TEM images of Polylactide/ Montmorillonite (MMT) nanocomposite film.[160]

2.3 Layer-by-Layer Assembly

In order to induce higher functionality and performance, one needs to control molecular orientation of composites on nanoscale, as their properties strongly depend on the local environment.[34, 161-164] Langmuir-Blodgett (LB) deposition accomplishes this by consecutively depositing single molecular layers.[165-167] Unfortunately, the LB technique requires expensive equipment and is limited with respect to substrate size.[34, 48] It is also difficult to obtain high quality multilayer films due to the high steric demand of covalent or coordination chemistry, making it desirable to have an alternate method for fabricating nanostructured films. The electrostatic attraction between cationic and anionic molecules is a straightforward driving force to build up multilayer thin films. Iler was the first to propose the concept in 1966,[168-170] but it was more than twenty years later that Decher and coworkers popularized layer-by-layer (LbL) assembly.[34] In this case, multilayer films are built up by alternately dipping substrates into oppositely charged polyelectrolyte solutions, as shown in Figure 2.10.[34, 171, 172] Over the past two decades, the LbL assembly technique has received significant attention due to its precise tailorability of thin film structure through adjustment of concentration,[35, 36] pH/ionic strength,[37-39] temperature,[38, 40] molecular weight[41, 42] and deposition time[35, 43, 44] of the aqueous deposition mixtures. Although electrostatic attraction is the most common bonding type for LbL, hydrogen bonding[46, 173, 174] and covalent bonding[175-177] can also be used to grow multilayer thin films. LbL films are now being used for a variety of applications, including antireflection,[57-59] regular/stretchable gas barrier,[174, 178] flame resistant[60-62] and drug delivery.[54-56] Another advantage of this multilayer assembly technique is the large nanoparticle concentration that can be achieved relative to bulk composites,[65, 66, 179] which provides high performance with a much thinner coating. The free volume of the polymer matrix or distance between each deposited nanoplatelet layer can be tailored to control the diffusivity of different permeating gases. This will be described in more detail in Sections 2.3.1 and 2.3.2.

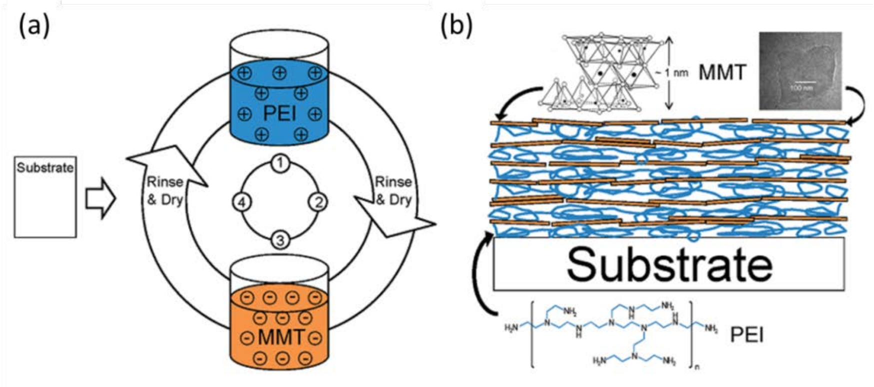

Figure 2.10. (a) Schematic of layer-by-layer assembly. (b) cross-sectional illustration of the nanobrickwall stricture.[110]

2.3.1 Gas Barrier Behavior of Multilayer Thin Films

Anionic clay, such as montmorillonite (MMT), has been paired with cationic polyelectrolytes such as polyethylenimine (PEI),[110] polyacrylamide (PAm)[159] and chitosan (CH)[180] to create bilayer assemblies. These sub-micron assemblies reduced the thick polymer substrate oxygen transmission rates (OTR) by 2 to 3 orders of magnitude.

Texas A&M's Polymer NanoComposites Lab[178] discovered that clay spacing, which is the distance between each deposited clay layers, can be controlled by varying the pH of polyelectrolyte solutions or the number of polymer layers deposited between clay layers, as shown in Figure 2.11.[110, 181] It was found that greater clay spacing improved gas barrier. Replacing MMT with vermiculite (VMT) clay or graphene oxide (GO) in these multilayers also decreased oxygen permeability (up to five times lower than MMT) due to higher platelet aspect ratio (4X larger than MMT), as predicted by Cussler's model.[65, 182] Since most LbL films are assembled from aqueous solutions, it is not surprising that exposure to moisture increases free volume of the film and increases gas permeability. Yang and Stevens suppressed moisture sensitivity by thermally reducing GO in a PEI/GO bilayer assembly,[65, 183] maintaining barrier under humid conditions. Schaaf and coworkers introduced Nafion into a clay-based assembly.[154] The addition of this hydrophobic fluorinated polymer preserved the OTR (97% reduction relative to uncoated poly(lactic acid) (PLA)) under humid condition, and reduced water vapor transmission rate (WVTR) by 78%.

Polymer-only multilayers have also been shown to exhibit high barrier (comparable to polymer-clay assemblies). Yang showed that altering the pH of PEI and PAA increased film thickness and polymer interdiffusion to create a "scramble salt" structure with higher density (1.13 g cm^{-3}) than a simple polymer mixture.[63] This increased density was due to decreased fractional free volume, which explains why 8 BL of PEI/PAA (305 nm thick) exhibits the lowest oxygen permeability (3.2×10^{-21} cm^3 cm cm^{-2} s^{-1} Pa^{-1}) ever reported for a neat polymer thin film. The present dissertation explores barrier properties of different gases, with a focus on decreasing free volume of the polymer layer and increasing the level of filler deposited (Chapter III[184] and IV). The influence of GO and polymer pH, on moisture sensitivity and barrier behavior, is also evaluated (Chapter V).

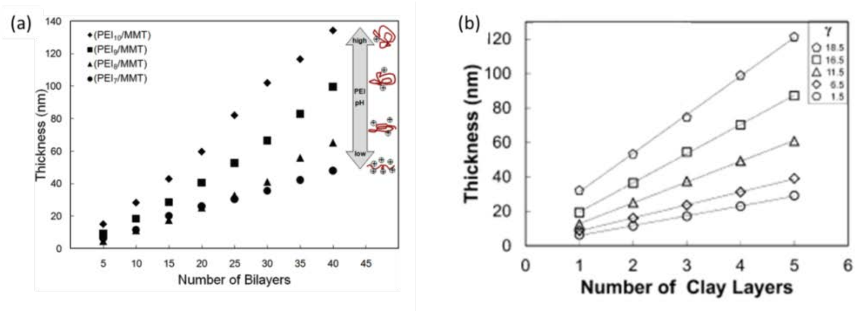

Figure 2.11. Thickness of PEI/MMT as a function of bilayers deposited while varying pH of PEI. (b) Thickness as a function of clay layers deposited with varying numbers of poly(allyl amine) (PAAm)/poly(acrylic acid) (PAA) bilayers [γ] between clay depositions.[181]

2.3.2 Gas Separation Behavior of Multilayer Thin Films

Gas separation membranes are currently used to separate hydrogen from gas mixtures (H_2/CH_4, H_2/CO, H_2/hydrocarbons),[22, 185, 186] recover CO_2 from CH_4, N_2, CO or other hydrocarbons, and remove H_2S and CO_2 from biogas.[19, 187, 188] Even more than for barrier, gas separation requires a defect-free film, because small gas molecules will permeate through the smallest defect present.[189] Layer-by-layer is already known for its ability to generate defect-free assemblies. Stroeve and coworkers discovered that 100 BL of PAAm/poly(styrene sulfonate) (PSS) exhibited high CO_2/N_2 selectivity (~24) at 50 ^{o}C,[190] although this film exhibited low flux. McCarthy and coworkers reported an increased selectivity for H_2/N_2 and H_2/O_2 when applying 20 to 200 BL of poly (allylamine hydrochloride) (PAH)/PSS, but this film also has low gas permeability due to the formation of a dense and rigid structure.[191] Another group induced imidization after depositing PAH/poly(amic acid), as shown in Figure 2.12. The newly formed polyimide membrane exhibited comparable O_2/N_2 (6.9) and CO_2/N_2 (68) selectivity as conventional PI membranes.[192] Nanoparticles have also been used in LbL assemblies for gas separation. GO platelets were assembled with polyelectrolyte or zeolitic imidazolate framework (ZIF), showing a H_2/CO_2 selectivity of 383[65] and H_2/N_2 selectivity of 90.[193] Tsapatsis and coworkers reported a zeolite/silica assembly that separated H_2 from N_2.[194] This completely inorganic assembly was under the Robeson upper-bound Figure 2.13, but its strong heat resistance allowed for a wide range of operating temperature (from room temperature to 200 ^{o}C). The present dissertation focuses on two types of gas separation membranes: CH/PAA/CH/GO mixed matrix assemblies (Chapter V) and PEI/PAA all-polymer assemblies (Chapter VI).[195]

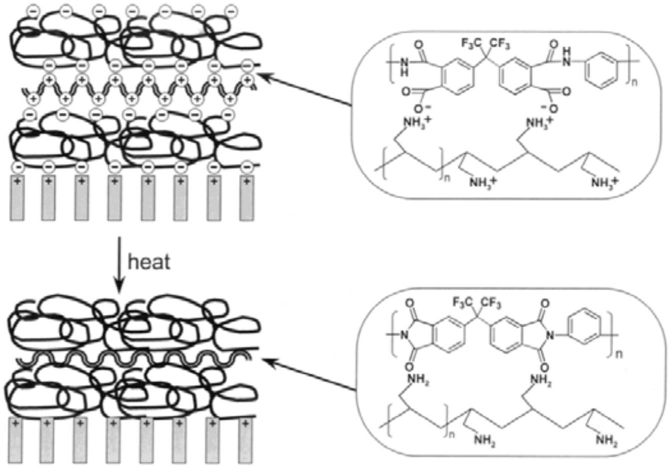

Figure 2.12. Thermal imidization of PAH/poly(amic acid) assembly on a porous alumina support.[192]

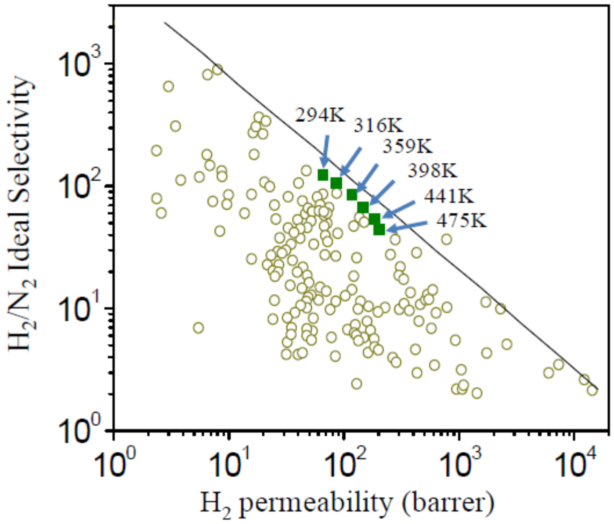

Figure 2.13. Robeson plot for a MCM-22/silica membrane (membrane A3B3), placed in context with other membranes for H_2/N_2 separation.[194]

CHAPTER III*

INFLUENCE OF POLYMER INTERDIFFUSION AND CLAY CONCENTRATION ON GAS BARRIER OF POLYELECTROLYTE/CLAY NANOBRICK WALL QUADLAYER ASSEMBLIES

3.1 Introduction

Super gas barrier exhibited by some layer-by-layer assemblies has led to significant study.[65, 180, 196-198] Two approaches have been used to produce low oxygen permeability. The first is to create an extremely tortuous path by layering nanoplatelets, such as clay and graphene oxide.[65, 197] The impermeable gas platelets create a tightly packed nanobrick wall structure that significantly extends the diffusion pathway of a gas molecule. The best system to-date is a quadlayer (QL) system prepared by repeatedly depositing polyethylenimine (PEI), poly(acrylic acid) (PAA), PEI, and montmorrilonite (MMT) clay.[197] In this case, a 4QL film, with a thickness of 50nm, achieved an oxygen transmission rate of 0.005 cm^3 m^{-2} day^{-1} atm^{-1}. A second approach exploits extensive polyelectrolyte interdiffusion to obtain an exceptionally dense film.[198] The greatest oxygen barrier has been achieved with an "exponentially growing" polyelectrolyte combination.

---

*Reprinted with permission from "Journal of Membrane Science" by Tzeng, P.; Maupin, C. R.; Grunlan, J. C., "Influence of Polymer Interaction and Clay Concentration on Gas Barrier of Polyelectrolyte/Clay Nanobrick Wall Quadlayer Assemblies" *J. Membr. Sci.* **2014**, *452*, 46-53, Copyright [2015] by Elsevier.

Further improvement in barrier performance could be achieved by combining these two concepts in a single film. For instance, weak polycations are known to have a distinct degree of ionization at a given pH and they can ionize a neighboring polyanion to a given degree, resulting a more interdiffused complex.[199, 200] In the present study, cationic polyvinylamine (PVAm) and polyethylenimine and anionic poly(acrylic acid) and sodium montmorillonite were assembled as polycation/PAA/polycation/MMT quadlayers (QL). Various combinations of polycations were investigated, resulting in differences in film thickness, clay concentration (and spacing) and oxygen transmission rate. A six PVAm/PAA/PVAm/MMT quadlayer film has a thickness (175 nm) five times that of a 2 QL film, while its OTR is two orders of magnitude lower (0.009 cm^3 m^{-2} day^{-1} atm^{-1}). Compared to bare PET with no thin film coating, the OTR is 3 orders of magnitude lower. These transparent and flexible gas barrier films are now more tailorable, allowing a film to be designed for a specific flexible electronics or food packaging application.

3.2 Experimental

3.2.1. Materials

Branched polyethylenimine (Aldrich, St. Louis, MO) (M_W ~ 25,000 g mol^{-1}) and polyvinylamine (BASF, Florham Park, NJ) (M_W ~ 340,000 g mol^{-1}, >90% hydrolyzed) are cationic polymers that were dissolved into 18.2 MΩ deionized water to create independent 0.1 wt% solutions. The pH was adjusted from its unaltered value (~10.5 for PEI and ~6.8 for PVAm) to 10 by adding 1.0 M hydrochloric acid (HCl) or 1.0 M sodium hydroxide (NaOH). Titration of PVAm revealed a pKa in the range of 7.3 - 8.5. pH measurements for titrating 0.1M PVAm solutions were performed using an IQ 240 pH meter (0.01 pH unit sensitivity). 10N NaOH and HCl were used to change PVAm from its natural pH (~7.2) into its covalent and ionic forms (see Supporting Information). Poly(acrylic acid) (Aldrich) (M_W ~ 100,000 g mol^{-1}) is an anionic polymer that was prepared as a 0.2 wt% solution with 18.2 MΩ deionized water. The pH of PAA was adjusted from its unaltered value (~3.1) by adding 1.0 M NaOH. Anionic natural sodium montmorillonite (MMT) (trade name Cloisite Na^+) (Southern Clay Products, Inc., Gonzales, TX) clay was prepared as a 1 wt% aqueous suspension. This suspension of high aspect ratio nanoplatelets (*l*/d is 80 to 300)[201] was used at its natural pH (~9.7).

3.2.2. Substrates

Single-side-polished (100) silicon wafers (University Wafer, South Boston, MA) were used as deposition substrates for ellipsometry and atomic force microscopy (AFM). Fused quartz slides (Structure Probe, Inc. West Chester, PA) were used for visible light transmission measurement via UV-vis spectroscopy. Both silicon wafers and quartz slides were piranha treated with a 3:1 ratio of 30% hydrogen peroxide to 99% sulfuric acid and stored in deionized water before use. *Caution: Piranha solution reacts violently with organic material and needs to be handled properly.* Prior to use, the silicon wafers were rinsed with acetone and deionized water. Poly(ethylene terephthalate) (PET) film, with a thickness of 179 µm (trade name ST505, Dupont–Teijin), was purchased from Tekra (New Berlin, WI). This film was rinsed with deionized water and methanol before use. Clean PET was then corona-treated with a BD-20C Corona Treater (Electro-

Technic Products Inc., Chicago, IL). Corona treatment improves adhesion of the first polyelectrolyte layer by oxidizing the film surface.[202] Polished Ti/Au crystals, with a resonance frequency of 5 MHz, were purchased from Maxtek, Inc (Cypress, CA) and used as deposition substrates for quartz crystal microbalance (QCM) characterization.

3.2.3. Layer-by-Layer Deposition

The layer-by-layer process is shown schematically in Figure 3.1. A given substrate was first dipped into the polycation solution (PEI and/or PVAm) for 5 minutes, followed by rinsing with deionized water for 30 seconds and drying with a stream of filtered air. After the first positively-charged layer was adsorbed, the substrate was dipped into PAA solution for another 5 minutes, followed by another rinsing and drying cycle. The substrate was then dipped into polycation and MMT solutions to form one "quadlayer". Starting from the second deposition cycle, the remaining numbers of layers were created using one minute dip times. This process was carried out using home-built robotic systems.[203, 204] The pH of PEI, PVAm or PAA is shown as a subscript next to their initials in the figures and text. For example, one quadlayer of PVAm(pH=10)/PAA(pH=4)/PVAm(pH=10)/MMT(unaltered pH of 9.7) is abbreviated as $(\mathrm{PVAm}_{10}/\mathrm{PAA}_{4}/\mathrm{PVAm}_{10}/\mathrm{MMT})_{1}$.

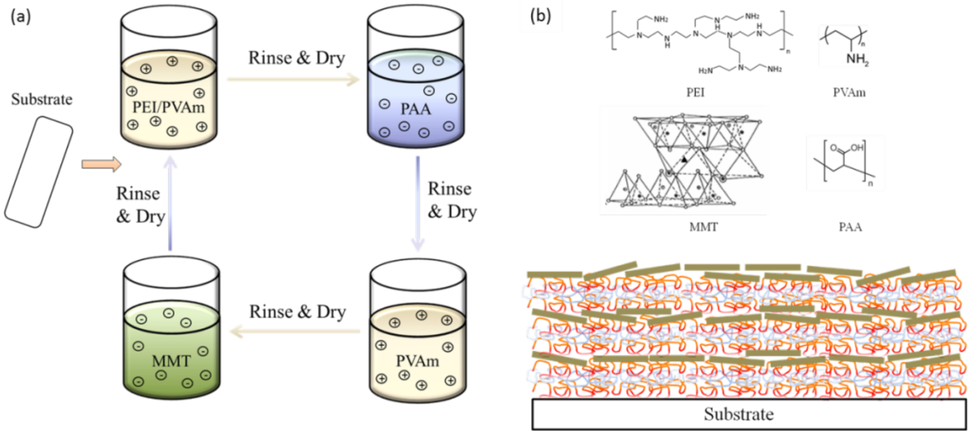

Figure 3.1. (a) Schematic of the quadlayer assembly process. (b) Polyelectrolytes and clay used in the quadlayer assemblies and a cross-sectional illustration of the resultant nanobrick wall thin film. MMT structure: [201] (▲)Al^{3+}, Mg^{2+}, Fe$^{3+/2+}$; (○) O^{2-}; (⊙) OH^{-}; (●)Si^{4+}.[184]

3.2.4.Thin Film Characterization

Assembly thickness on silicon wafers was measured every quadlayer with a PHE-101 Discrete Wavelength Ellipsometer (Microphotonics, Allentown, PA), using a 632.8 nm laser at an incidence angle of 65°. For the ($PEI_{10}/PAA_{4}/PEI_{10}$/MMT) system, 9 and 10 QL films were measured by a P-6 profilometer (KLA-Tencor, Milpitas, CA) due to their large thickness (>1000nm). Thicknesses from 2 to 8 QL were measured by both ellipsometer and profilometer, which showed similar values. Mass increments were measured each layer with a Research Quartz Crystal Microbalance (QCM) (Inficon, East Sycrase, NY) using a frequency range of 3.8 - 6 MHz. The 5 MHz quartz crystal was inserted in a holder and dipped into the solutions. After each deposition, the crystal was rinsed and dried and then left on the microbalance to stabilize for 5 minutes. Visible light transmission was obtained with a USB2000UV-vis spectrometer (Ocean Optics, Dunedin, FL). FTIR spectra of LbL films were measured with a Bruker Optics ALPHA-P 10098-4 spectrometer in ATR mode. PAA peaks in its covalent (COOH) and ionic form (COO^-) are of interest in this study to compare the ionic interaction between polycation and polyanion, or so called 'degree of ionization'. The COO^- and COOH peaks of PAA were first assumed to have similar extinction coefficients,[205] which allowed the fraction of ionized PAA carboxylic groups to be obtained by deriving $Abs_{1560}/(Abs_{1560}+Abs_{1710})$.[206] Cross-sections of the quadlayer assemblies were imaged with a JEOL 1200 EX TEM (Mitaka, Tokyo, Japan), operated at 110 kV. Samples were prepared for imaging by embedding a piece of coated PET in epoxy prior to sectioning it with a diamond knife. Surface structure of the coated silicon wafers were imaged with a Multimode Scanning Probe Microscope (SPM) (Veeco Digital Instruments, Santa Barbara, CA) in tapping mode. OTR testing was performed by MOCON (Minneapolis, MN) in accordance with ASTM D-3985,[207] using an Oxtran 2/21 ML instrument at 23°C and 0% RH.

3.3 Results and Discussion

3.3.1. Multilayer Film Growth

Film growth of three different polyamine quadlayer recipes was measured by ellipsometry and profilometry, as shown in Figure 3.2. Notice that instead of being three times as thick, $(PVAm_{10}/PAA_4/PVAm_{10}/MMT)_6$ is five times thicker than

$(PVAm_{10}/PAA_4/PVAm_{10}/MMT)_2$ due to “island growth”.[208] The growth of the first few layers is influenced by the substrate, resulting in the thickness per layer being thinner than the “bulk” film. PVAm-based quadlayers exhibit a linear growth trend, while PEI-based quadlayers exhibit exponential growth due to PEI/PAA interdiffusion.[51, 63, 197] Before deposition, both PEI_{10} and PAA_4 solutions are in a low charge form in which polymer chains are more globular. As deposition proceeded, these pH-sensitive polyelectrolytes became more highly charged due to the alternating pH (i.e., PEI encountering a lower pH when PAA was deposited and PAA encountering a higher pH environment). In order to compensate the newly formed charge inside the bulk film, more PEI and PAA were adsorbed into the growing multilayer, resulting in exponential growth.[51] The large film thickness observed here may seem counterintuitive for a highly-charged polymer backbone, but it should be noted that charge density and effective pKa can differ from their solution state values within the multilayer assembly.[209, 210] Degree of ionization is directly linked to pKa. The pKa of PVAm ranges from 7.3-8.5, PEI has pKa values of 6.5-8.5,[211-213] and PAA has pKa values of 5.5-6.5.[214, 215] Based on the fact that PEI has a slightly lower pKa than PVAm, along with results obtained from FTIR, PEI appears to be more responsive to changes in pH. This suggests that when encountering an acidic PAA environment, PEI can be easily ionized and have stronger ionic interaction with PAA than PVAm.[216] Figure 3.3 shows mass deposited for these same assemblies. All systems exhibit the same growth trends observed with ellipsometry (Figure 3.2). This data also provides the clay concentrations for each film, which are summarized in Table 1.

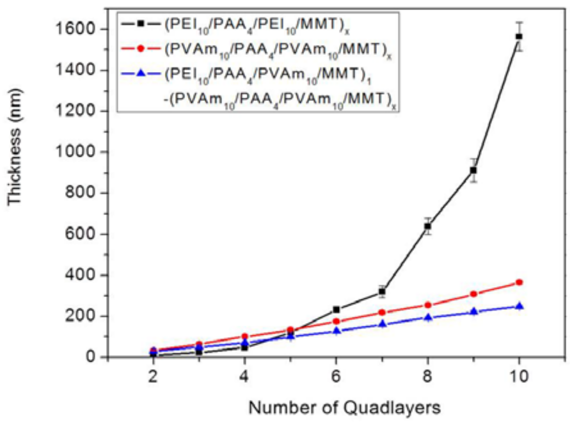

Figure 3.2. Film thickness as a function of quadlayers deposited with three recipes: ($PEI_{10}/PAA_4/$ $PEI_{10}/MMT)_x$, $(PVAm_{10}/PAA_4/PVAm_{10}/MMT)_x$ and $(PEI_{10}/PAA_4/PVAm_{10}/MMT)_1$- $(PVAm_{10}/PAA_4/PVAm_{10}/MMT)_{x-1}$.[184]

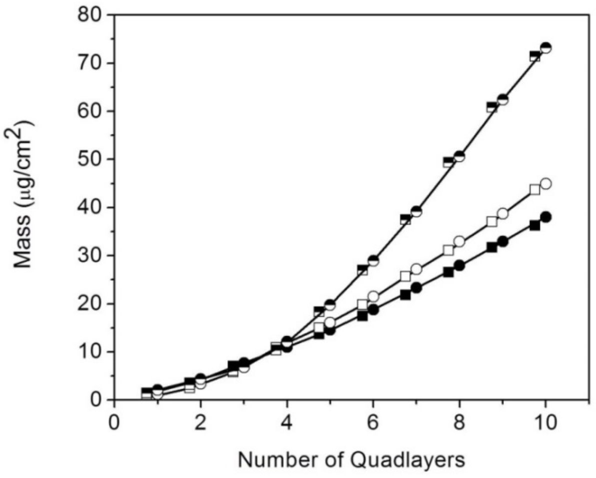

Figure 3.3. Mass as a function of quadlayers deposited with three recipes: $(PEI_{10}/PAA_4/PEI_{10}/MMT)_x$ (half-filled dots), $(PVAm_{10}/PAA_4/PVAm_{10}/MMT)_x$ (filled dots) and $(PEI_{10}/PAA_4/PVAm_{10}/MMT)_1$- $(PVAm_{10}/PAA_4/PVAm_{10}/MMT)_{x-1}$ (hollowed dots). Rectangular and circular dots indicate the accumulated mass measured from the beginning to the specific polymer or clay layer, respectively. [184]

Unlike PEI-based assemblies, $PVAm_x$ grows linearly. There are a few reasons why PEI displays greater interdiffusion than PVAm in these assemblies. PVAm has a higher T_g than PEI and therefore greater chain stiffness at room temperature, which inhibits diffusion in the polymer assembly.[217, 218] It has been shown that chain size (molar mass) or structure (branched polymer) can directly influence chain diffusion.[219] Others have shown that by increasing film surface roughness, more surface area is available to adsorb additional material that produces exponential growth.[219, 220] Even though the thickness of a PEI quadlayer is smaller than PVAm for the first few cycles, it surpasses PVAm after 5 QL. With this better understanding of the assembly mechanism, a relation between the number of PEI layers and thickness was observed. $(PEI_{10}/PAA_4/PVAm_{10}/MMT)_1$-$(PVAm_{10}/PAA_4/PVAm_{10}/MMT)_x$, though containing PEI in the assembly, grew linearly and was thinner than PVAm-based quadlayer, as shown in Figure 3.2. Two reasons might explain this phenomenon: (1) PEI/PAA actually grows thinner than PVAm/PAA at early stages and (2) clay layers are preventing interdiffusion.

FTIR analysis helps to explain why PEI and PVAm assemblies have such different properties. Infrared spectroscopy was used to compare the electrostatic interaction between polycations and polyanions. Figure 3.4 shows the FTIR spectra of $(PVAm_{10}/PAA_4/PVAm_{10}/MMT)_5$ and $(PEI_{10}/PAA_4/PEI_{10}/MMT)_5$ assemblies. For both systems, two peaks (1715 and 1560 cm^{-1} for PEI and 1671 and 1560 cm^{-1} for PVAm) and one shoulder (1630 cm^{-1} for PEI and 1715 cm^{-1} for PVAm) can be observed. It should be noted that the characteristic band of MMT occurs at 995 cm^{-1}, so all peaks between 1400 cm^{-1} and 1800 cm^{-1} can be attributed to the polyelectrolytes. Two different peaks represent the neutral (1715 cm^{-1}) and ionic (1560 cm^{-1}) form of PAA, respectively.[221, 222] The peak at 1630 cm^{-1} corresponds to $–NH_3^+$ bending. For $(PVAm_{10}/PAA_4/PVAm_{10}/MMT)_5$ film, the peak at 1671 cm^{-1} represents carbonyl groups, originating from the unhydrolyzed amide groups in PVAm.[223, 224] For the $(PEI_{10}/PAA_4/PEI_{10}/MMT)_5$ film, the neutral PAA peak (1715 cm^{-1}) decreases as the pH of PEI increases, which means the portion of ionized PAA (i.e., degree of ionization) increases.[223] The $PVAm_{10}/PAA_4/PVAm_{10}/MMT$ QL shows a similar trend, with the basic PVAm ionizing PAA. Figure 3.4(c) shows the FTIR spectra of both PEI and PVAm-based 5 QL film with the polycation at pH 10. It is observed that PAA in PEI-based quadlayers is almost fully ionized, because no peak or shoulder appears at 1715 cm^{-1}. PVAm-based quadlayers, on the other hand, have a neutral PAA shoulder, which suggests a lower degree of ionization. The difference in degree of ionization of PEI and PVAm-based assemblies demonstrates a weaker PVAm/PAA interaction than PEI/PAA. The lower degree of ionization in the PVAm-based QL suggests that there is less ionic crosslinking inside the assembly, resulting in a lower density film, which explains the larger thickness of PVAm-based assemblies at a low number of quadlayers.

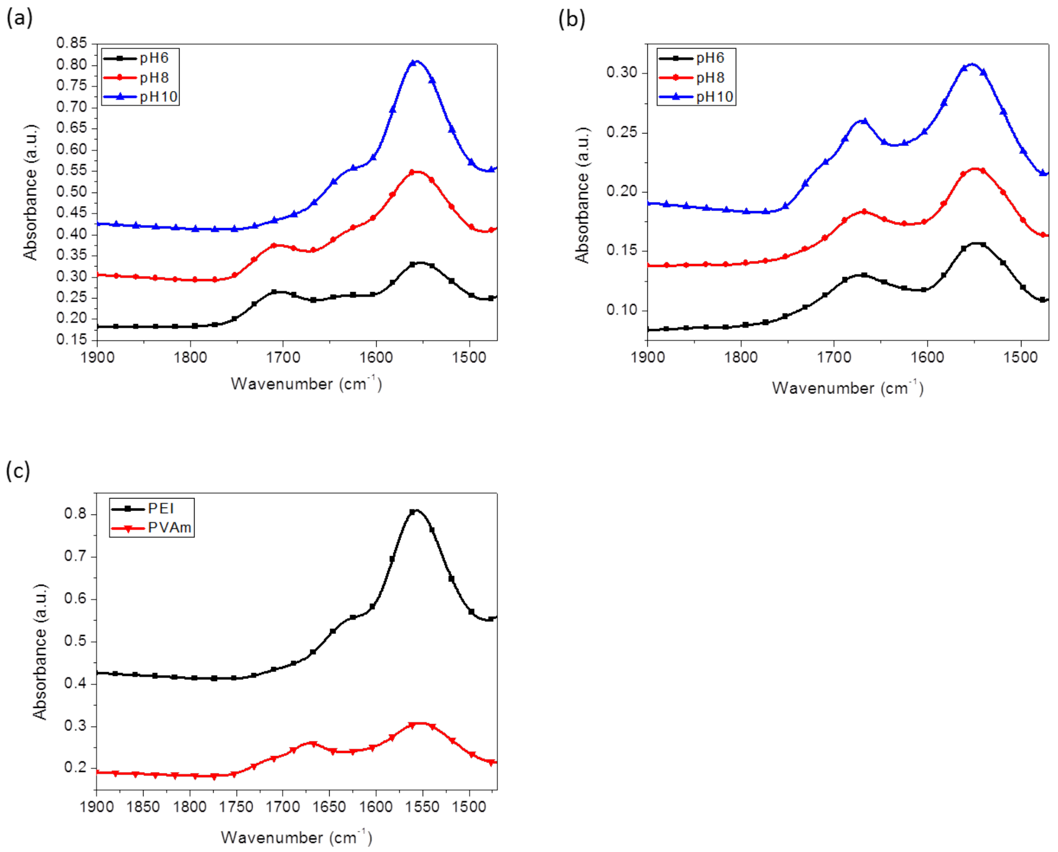

Figure 3.4. FTIR spectra of 5QL (a) $PEI_{10}/PAA_4/PEI_{10}/MMT$ and (b) $PVAm_{10}/PAA_4/PVAm_{10}/MMT$ at different polycation pH, and a combination of (c) both assemblies at polycation pH 10.[184]

3.3.2. Nanobrick Wall Thin Film Structure

TEM cross-sectional images of $(PVAm_{10}/PAA_4/PVAm_{10}/MMT)_5$ and $(PEI_{10}/PAA_4/PEI_{10}/MMT)_5$ are shown in Figure 3.5(a) and (b). The thickness observed in these images verifies the result obtained from ellipsometry (Figure 3.2) and looks strikingly similar to the schematic nanobrick wall structure (Figure 3.1) and a TEM cross section from an earlier study.[197] The film in Figure 3.5(a) is a little thicker and has some waviness due to stress relief during sectioning and the section being cut at a slight angle. In this PVAm-based quadlayer, five clay layers can be clearly observed as dark lines, which match the number deposited. For the PEI-based quadlayer (Figure 3.5(b)), an ordered nanobrick wall structure is still observed, although it is difficult to identify each clay layer. This TEM micrograph demonstrates that clay platelets deposit in a highly oriented fashion, resulting in the excellent oxygen barrier behavior described in the next section. AFM height images of $(PVAm_{10}/PAA_4/PVAm_{10}/MMT)_5$ and $(PEI_{10}/PAA_4/PEI_{10}/MMT)_5$ are shown in Figure 3.5(c) and (d). The cobblestone-like structure in both assemblies reveals that the platelets are tightly packed, which agrees with previous studies of polymer-clay assemblies.[36, 110, 159, 197] It is this combination of tight packing and near perfect orientation of clay platelets that produces low gas permeability when these films are deposited onto thick plastic films (e.g., PET) commonly used for packaging.

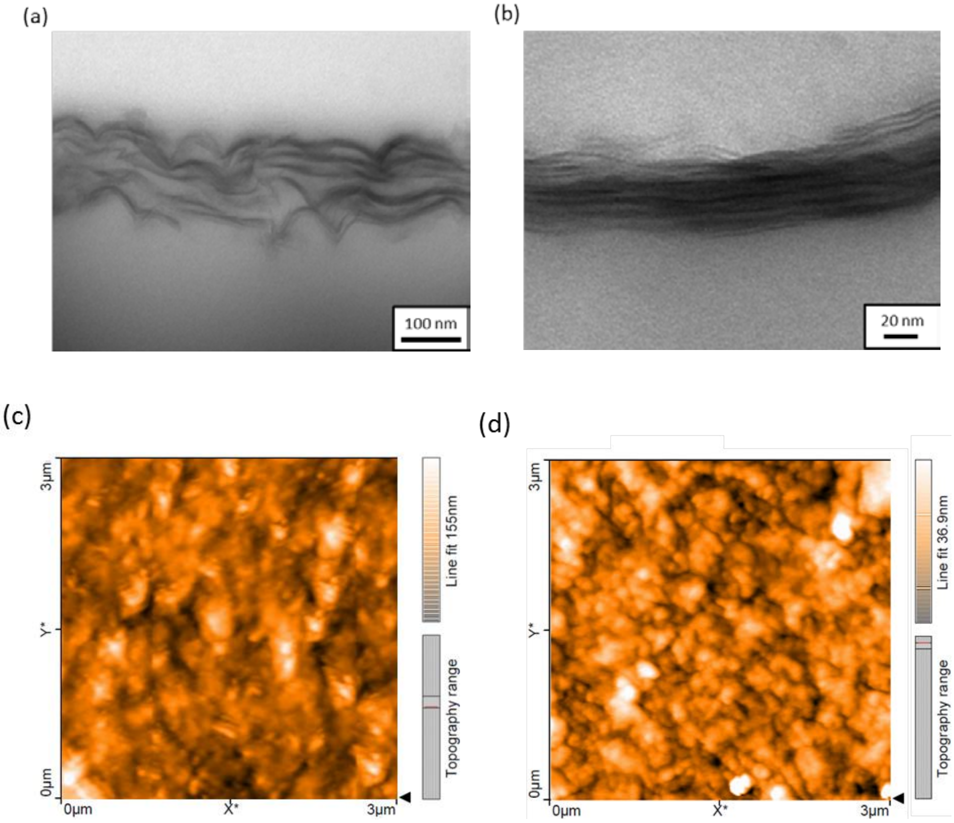

Figure 3.5. TEM cross sectional images of (a) $(PVAm_{10}/PAA_4/PVAm_{10}/MMT)_5$ and (b) $(PEI_{10}/PAA_4/PEI_{10}/MMT)_5$, deposited on PET substrate. AFM height images of (c) $(PVAm_{10}/PAA_4/PVAm_{10}/MMT)_5$ and (d) $(PEI_{10}/PAA_4/PEI_{10}/MMT)_5$ films.[184]

In many applications, optical transparency is as important as gas transmission rate for barrier films. Visible light transmission (390-750nm) of PVAm-based quadlayers is shown in Figure 3.6(a). As the number of quadlayers increase from 2 to 6, light transmission decreases only slightly, from 98.3% to 96.8%. Compared to the change in film thickness, light transmission was expected to decrease more rapidly. This same phenomenon has been observed in previously studied polymer/clay thin films.[36, 110, 159] Such high transparency after 6 QL is likely due to the fact that clay platelets are near perfectly aligned and well separated from each other through the film thickness, as shown in Figure 3.5. Images of PVAm-based quadlayers on PET film, shown in Figure 3.6(b), reveal how transparent and defect free these nanobrick walls are over a significant area (100 cm^2). The LbL technique allows for high clay loading (>24wt %) without the same clay aggregation issues associated with conventional polymer/clay composite films.[225, 226]

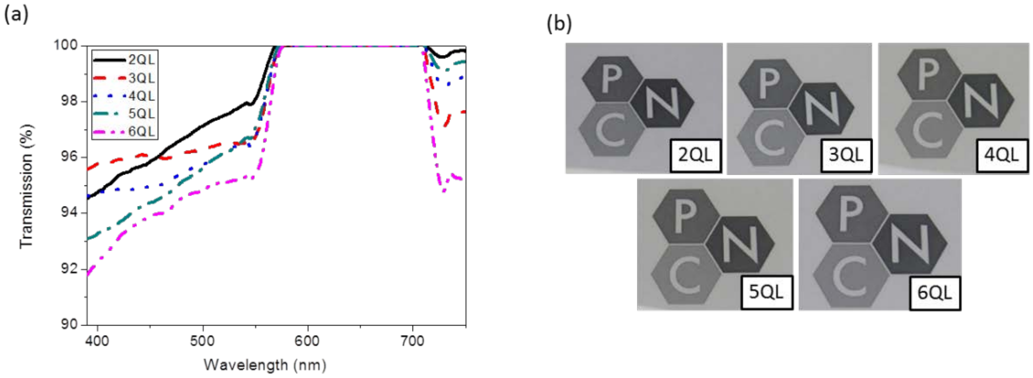

Figure 3.6. (a) Visible light transmission as a function of wavelength for PVAm-based QL on fused quartz slides. (b) Image of $(PVAm_{10}/PAA_4/PVAm_{10}/MMT)_x$ thin films deposited on 179µm PET.[184]

3.3.3. Oxygen Barrier of Quadlayer Assemblies

The nanobrick wall structure of these quadlayer assemblies creates an extremely tortuous pathway that significantly extends a permeating molecule's diffusion time.[159, 225, 226] Because the clay platelets are densely packed, they reroute the diffusion length perpendicular to the thickness direction of the film, which lowers the gas transmission rate.[227] Figure 3.7(a) shows the oxygen transmission rate (OTR) of PVAm-based quadlayers coated on 179μm PET film. Though the OTR of a $(PVAm_{10}/PAA_4/PVAm_{10}/MMT)_2$ coated PET film is similar to bare PET film (~8.6 cm^3 m^{-2} day^{-1} atm^{-1}), 3QL of this recipe is able to lower the OTR by two orders of magnitude, while only increasing PET thickness ~0.04%. As the number of QL increases to six, OTR decreases to 0.009 cm^3 m^{-2} day^{-1} atm^{-1}). Compared to other thin, clay-based barrier films, this 6QL nanocoating is two orders of magnitude lower in both OTR and thickness.[196, 228, 229] Additionally, this $(PVAm_{10}/PAA_4/PVAm_{10}/MMT)_6$ assembly has a comparable thickness to SiO_x nanocoatings, but one order of magnitude lower OTR.[230-232] It is three orders of magnitude below the OTR of 25 μm thick EVOH film.[233] When compared on the basis of permeability, which normalizes thickness, these quadlayers have even better barrier. Figure 3.7(a) shows that permeability decreases as a function of QL deposited on PET. Each new polymer and clay layer not only increases film thickness, but also the residence time of permeating molecules due to a more tortuous pathway. With an oxygen permeability of 3.7×10^{-21} (cm^3(STP) cm cm^{-2} Pa^{-1} s^{-1})) for $(PVAm_{10}/PAA_4/PVAm_{10}/MMT)_6$, this transparent, 175 nm thick coating has a permeability comparable to metalized plastic film.[234, 235]

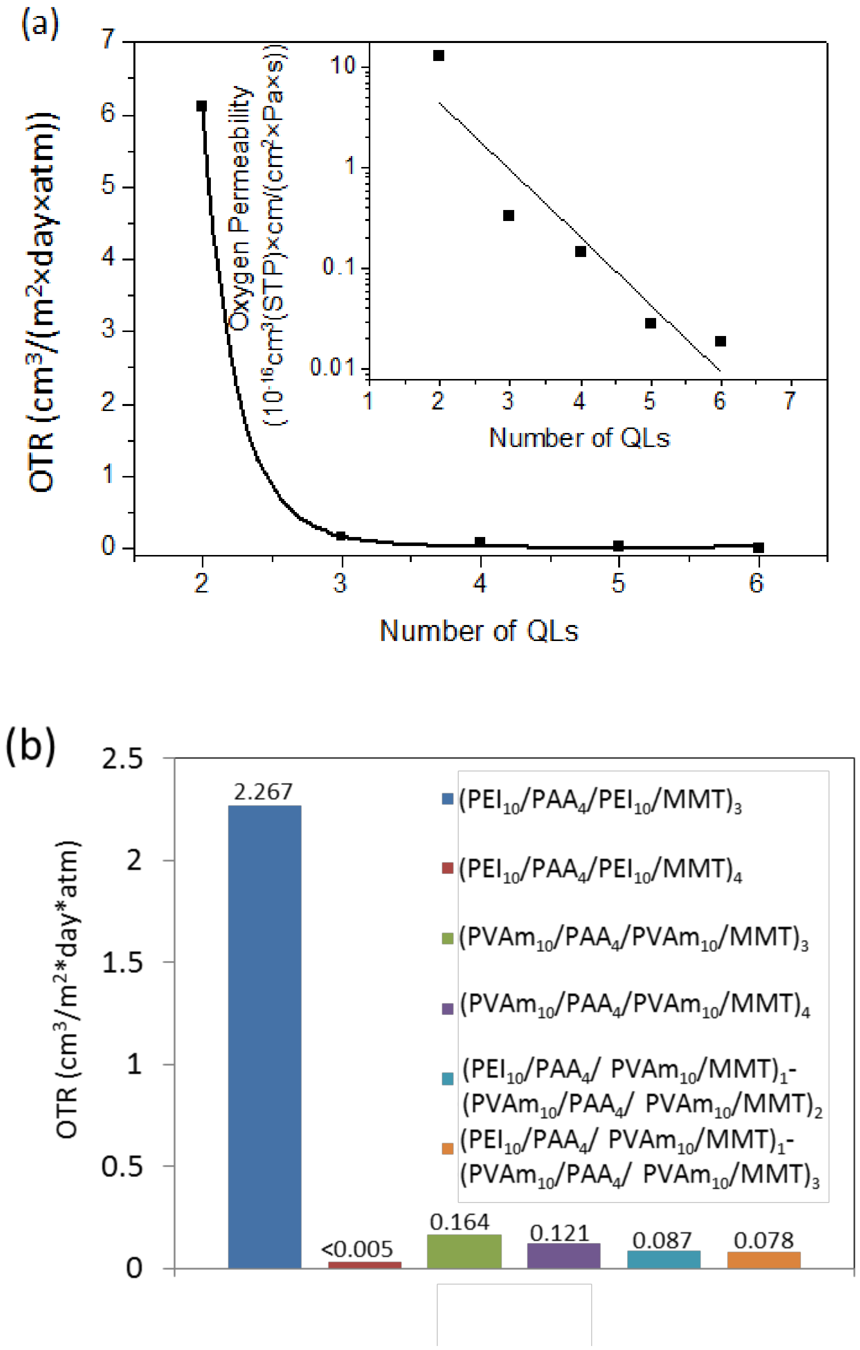

Figure 3.7. (a) Oxygen transmission rate and oxygen permeability as a function of PVAm-based quadlayers deposited on 179µm PET. (b) Oxygen transmission rate as a function of quadlayer recipe and number deposited on 179µm PET.[184]

Table 3.1. Oxygen transmission rate, film thickness, and clay concentration of quadlayer thin films deposited on 179 μm PET.[184]

	OTR ($cm^3\ m^{-2}\ day^{-1}\ atm^{-1}$)	Film thickness (nm)	Clay (wt%)	Oxygen Permeability ($10^{-16} cm^3(STP)\ cm\ cm^{-2}\ Pa^{-1}\ s^{-1}$)	
				Coating[a]	Total
179 μm PET					17.50
$(PVAm_{10}/PAA_4/PVAm_{10}/MMT)_2$	6.122	33.7	35.0	0.0169	12.52
$(PVAm_{10}/PAA_4/PVAm_{10}/MMT)_3$	0.164	64.4	27.5	0.00025	0.34
$(PVAm_{10}/PAA_4/PVAm_{10}/MMT)_4$	0.071	101.2	25.6	0.00017	0.15
$(PVAm_{10}/PAA_4/PVAm_{10}/MMT)_5$	0.014	145.4	24.6	0.000046	0.03
$(PVAm_{10}/PAA_4/PVAm_{10}/MMT)_6$	0.009	175.2	24.1	0.000037	0.02
$(PEI_{10}/PAA_4/PVAm_{10}/MMT)_1$-$(PVAm_{10}/PAA_4/PVAm_{10}/MMT)_2$	0.037	51.3	40.4	0.000044	0.08
$(PEI_{10}/PAA_4/PVAm_{10}/MMT)_1$-$(PVAm_{10}/PAA_4/PVAm_{10}/MMT)_3$	0.026	72.6	34.0	0.000043	0.06
$(PEI_{10}/PAA_4/PEI_{10}/MMT)_3$	2.267	28.3	48.6	0.002	4.64
$(PEI_{10}/PAA_4/ PEI_{10}/MMT)_4$	<0.005[b]	50.9	36.7	≤0.000005[b]	≤0.001[b]

[a] The quadlayer thin film permeability was decoupled from the total permeability using a previously described method.[229] [b] The low-end OTR detection limit for an Oxtran 2/21L module is 0.005 $cm^3\ m^{-2}\ day^{-1}\ atm^{-1}$.

The OTR values of $(PEI_{10}/PAA_4/PEI_{10}/MMT)_x$, $(PVAm_{10}/PAA_4/PVAm_{10}/MMT)_x$ and $(PEI_{10}/PAA_4/PVAm_{10}/MMT)_1$-$(PVAm_{10}/PAA_4/PVAm_{10}/MMT)_{x-1}$ at 3 and 4 QL are compared in Figure 3.7(b) and Table 3.1. $(PEI_{10}/PAA_4/PEI_{10}/MMT)_x$ is undetectable at 4QL while $(PVAm_{10}/PAA_4/PVAm_{10}/MMT)_x$ exhibits barrier performance that may be good enough for food packaging, LEDs and photovoltaic encapsulation at just 3QL.[236] As for $(PEI_{10}/PAA_4/PVAm_{10}/MMT)_1$-$(PVAm_{10}/PAA_4/PVAm_{10}/MMT)_{x-1}$ at 3 and 4 QL, OTR is reduced by a factor of 4 (3QL) and 2 (4QL) compared to the PVAm-only assembly. There are two contributing factors to the OTR difference in these systems. First, for a constant number of QL, replacing PVAm with PEI causes more interdiffusion to occur at the interface with PAA, which creates a denser film. This assertion is supported by the FTIR results described earlier (Figure 3.4). Another factor is greater clay concentration in the $(PEI_{10}/PAA_4/PVAm_{10}/MMT)_1$-$(PVAm_{10}/PAA_4/PVAm_{10}/MMT)_{x-1}$ assemblies, as shown in Table 3.1. Assuming similar clay oreintation in all quadlayer systems, evidenced by AFM and TEM images in Figure 3.5, it is reasonable to correlate lower OTR with greater clay concentration.[36, 197] Cussler's model[227] is used to qualitatively explain the mechanism of our aligned, flake-filled membrane:

$$\frac{P_0}{P} = 1 + \mu\alpha^2\left(\frac{\varphi^2}{1-\varphi}\right) \tag{3.1}$$

where P_0, the polymer permeability, over P, the composite permeability, is a function of the filler aspect ratio (α), geometric factor (μ) and volume fraction in the composite (φ). Additionally, the model is most consistent with the assumption that the filler loading is 'semidilute':[101]

$$\varphi \ll 1 \tag{3.2}$$

$$\alpha\varphi > 1 \tag{3.3}$$

The predicted filler aspect ratios of $(PVAm_{10}/PAA_4/PVAm_{10}/MMT)_4$, $(PEI_{10}/PAA_4/PVAm_{10}/MMT)_1$-$(PVAm_{10}/PAA_4/PVAm_{10}/MMT)_3$ and $(PEI_{10}/PAA_4/PVAm_{10}/MMT)_4$ are 398, 542 and 752 (Table 3.2), respectively, which are much larger than the experimentally measured aspect ratio (~ 166).[93] The primary issue is that our films likely do not adequately meet the "semi-dilute" assumption of Cussler's model. Our filler volume fraction is only one order of magnitude smaller than 1, and $\alpha\varphi$ is almost two orders of magnitude larger than 1, suggesting we are more filler-saturated than the model assumes. It is also possible that overlap between adjacent clay platelets creates a much larger effective aspect ratio. Nevertheless, the model does a good job of qualitatively describing the behavior we observe.

Table 3.2. Oxygen permeability data of PVAm quadlayers and aspect ratio prediction.

	Film thickness (nm)	Volume Fraction of filler	Oxygen Permeability (10^{-16}cm^3(STP) cm cm^{-2} Pa^{-1} s^{-1})	Cussler's aspect ratio prediction[a]
$(\mathrm{PVAm_{10}/PAA_4})_6$	96.2		0.17	
$(\mathrm{PEI_{10}/PAA_4})_6$	369[c]		0.057[c]	
$(\mathrm{PVAm_{10}/PAA_4/PVAm_{10}/MMT})_4$	101.2	0.12	0.00017	398
$(\mathrm{PEI_{10}/PAA_4/PVAm_{10}/MMT})_1$-$(\mathrm{PVAm_{10}/PAA_4/PVAm_{10}/MMT})_3$	72.6	0.16	0.000043	542
$(\mathrm{PEI_{10}/PAA_4/PVAm_{10}/MMT})_4$	50.9	0.18	≤0.000005[b]	752

[a] Clay aspect ratio predicted from Cussler's model. [b] The low-end OTR detection limit for an Oxtran 2/21L module is 0.005 cm^3 m^{-2} day^{-1}atm^{-1}. [c] $(\mathrm{PEI_{10}/PAA_4})_6$ results obtained from our previous work.[184]

In the 4QL assemblies, barrier improves as more PVAm layers are replaced with PEI, which results in a higher clay concentration. For the 3QL systems, the same trend is observed in $(\mathrm{PVAm_{10}/PAA_4/PVAm_{10}/MMT})_3$ and $(\mathrm{PEI_{10}/PAA_4/PVAm_{10}/MMT})_1$-$(\mathrm{PVAm_{10}/PAA_4/PVAm_{10}/MMT})_2$, however $(\mathrm{PEI_{10}/PAA_4/PEI_{10}/MMT})_3$ has the highest OTR despite having the highest clay concentration. This exception is likely related to clay spacing.[110] The PEI-based 3QL film is almost 50% thinner than other two systems, resulting in a much smaller clay spacing of 4.6 nm. $(\mathrm{PVAm_{10}/PAA_4/PVAm_{10}/MMT})_3$ and $(\mathrm{PEI_{10}/PAA_4/PVAm_{10}/MMT})_1$ - $(\mathrm{PVAm_{10}/PAA_4/PVAm_{10}/MMT})_2$ have clay spacing of 23.5 nm and 14.4 nm, respectively. Low OTR in LbL films seems to require a critical combination of minimum clay concentration, spacing and layers.[159, 181, 197]

3.4 Conclusions

Quadlayer assemblies, deposited using the layer-by-layer technique, were used to study how polyelectrolyte interdiffusion and clay concentration influence the gas barrier behavior of these thin films. Positively-charged PEI and PVAm were combined with negatively-charged PAA and MMT to generate ‘nanobrick walls’. Highly oriented clay platelets, revealed with TEM and AFM, are the reason for the exceptional oxygen barrier exhibited by these films. As the number of polymer-clay quadlayers increase, the OTR of PVAm-based QL deposited on PET decreases. Rigid PVAm molecules cause quadlayer growth to be linear rather than exponential, which occurs with more flexible PEI. This results in thinner layers for PVAm and weaker interaction with PAA relative to PEI. This weak interaction also seems to carry over to MMT, which results in lower clay concentration for PVAm-based assemblies. This study confirms the importance of polymer interdiffusion and clay concentration in reducing oxygen permeability in these nanobrick wall structures. PVAm and PEI were combined to tailor OTR by controlling these factors. It was found that simply switching the first PVAm layer to PEI simultaneously lowers the OTR and film thickness. It is now possible to simultaneously control OTR and thickness of a multilayer thin film barrier coating. This water-based nanocoating technology offers tremendous opportunity in food packaging, gas separation and protection of electronic devices.

CHAPTER IV*

SUPER HYDROGEN AND HELIUM BARRIER WITH POLYELECTROLYTE NANOBRICK WALL THIN FILM

4.1 Introduction

Gas barrier layers have found broad application for a variety of packaging applications for the food/pharmaceutical,[237] flexible electronics[238] and fuel cell[239] industries. These films often require a combination of low permeability, optical transparency, mechanical strength and flexibility.[240] Current barriers include metallized films,[241] SiO_x coatings[242] and polymer composites.[243] While these materials offer excellent barrier properties, they often suffer from poor substrate adhesion, undesirable optical quality and limited flexibility.[244] In contrast, LbL assemblies prepared with clay nanoplatelets have proven capable of overcoming all of these limitations.[180, 245-247] These nanobrick wall thin films have demonstrated undetectable oxygen transmission rate (OTR<0.005 cm^3 m^{-2} day^{-1} atm^{-1}) that rivals metallized films.[110] Additionally, this technology can be applied by spraying[248] or using a continuous immersion process.[249]

Hydrogen (H_2) is a key feedstock for the manufacture of petrochemicals, ammonia and methanol,[250] with H_2 corrosion and/or embrittlement of process equipment remaining a significant safety concern.[251] Conformal H_2 barrier coatings

---

*Reprinted with permission from "Macromolecular Rapid Communication" by Tzeng, P.; Lugo, E. L.; Mai, G. D.; Wilhite, B. A.; Grunlan, J. C. "Super Hydrogen and Helium Barrier with Polyelectrolyte Nanobrick Wall Thin Film" *Macromol. Rapid Comm.* **2015**, 3*6*, 96-101, Copyright [2015] by John Wiley and Sons.

would allow an extension of process equipment lifetime while reducing the risk of equipment failure owing to prolonged H_2 exposure. The wide flammability window and low ignition temperature for H_2 combine with an extremely high solid-state mobility, in both metallic and polymeric materials, to necessitate the use of thick-walled metallic containers for safe transport and storage of industrial scale H_2.[247] Recent growth in H_2-driven fuel cell technologies, offering high efficiencies and zero point-of-use emissions for portable, household and vehicular power generation necessitates breakthroughs in size and weight reduction for H_2 storage and transmission equipment,[252-254] which may be achieved through development of polymer nanocomposite barrier coatings.

Helium (He) is widely used in the manufacturing sector for leak detection[255, 256] and as an inert gas blanket for high-temperature welding[257] and reactive chemical storage.[258] It is also used in the medical sector as a cryogenic for magnetic resonance imaging (MRI) tools.[259, 260] Additionally, He and H_2 provide an excellent source of lift for lighter-than-air vehicles (for meteorological and aviation use).[261] Despite being the second-most abundant element in the universe, terrestrial supplies of helium continue to dwindle as released gas is sufficiently buoyant to escape the atmosphere.[262] This non-renewable nature of terrestrial He requires further advances in He-barrier film technologies to ensure the continued sustainability of manufacturing and medical industries. A high barrier thin film could allow He and H_2 to be stored, at least temporarily, in relatively lightweight polymeric containers.

Commercial He gas barriers currently employ aluminized polyurethane or polyolefin/polyester that are capable of providing low He permeability (10-300 cm^3 mm

m^{-2} day^{-1} atm^{-1}),[263, 264] but are produced using complex process conditions, have poor optical properties and potential health hazards. Metallization of polymeric films requires ultra-high vacuum and high temperature conditions, resulting in a complex and energy-intensive process. Aluminum nanocoatings are typically opaque and often have adhesion problems, which further limits their applicability.[116] These films also pose environmental and health concerns, as aluminum can contaminate the environment through both water or airborne transmission.[116] Current materials employed to fabricate H_2 gas barriers include ethylene vinyl-alcohol (EVOH) copolymer and polyester/nanoflake composites, with reported permeabilities of 0.1-3.1 cm^3 mm m^{-2} day^{-1} atm^{-1}.[247, 265, 266] Unfortunately, EVOH copolymers are plasticized in the presence of moisture, irreversibly altering morphology and creating increased free volume and permeability.[267] Polymer/nanoflake film properties remain difficult to control owing to both nanoflake dispersion and exfoliation during processing.

In the present work, a polymer/clay composite thin film, fabricated via layer-by-layer assembly, is investigated as a H_2 and He gas barrier. The simplicity of the LbL assembly technique, as compared to current films employed for He and H_2 barrier, make it an attractive alternative. The present quadlayer (QL) system was prepared by repeatedly depositing polyethylenimine (PEI), poly(acrylic acid) (PAA), PEI, and montmorillonite (MMT) clay (Figure 4.1a and 1b). This system was previously investigated for its super oxygen barrier,[66] but barrier to light gases (i.e., hydrogen and helium) was very unexpected. Highly aligned and impermeable clay platelets create an extremely tortuous pathway, consisting primarily of diffusion perpendicular to the film surface, extending permeate retention times and reducing even light gas transmission rate.[227, 268]

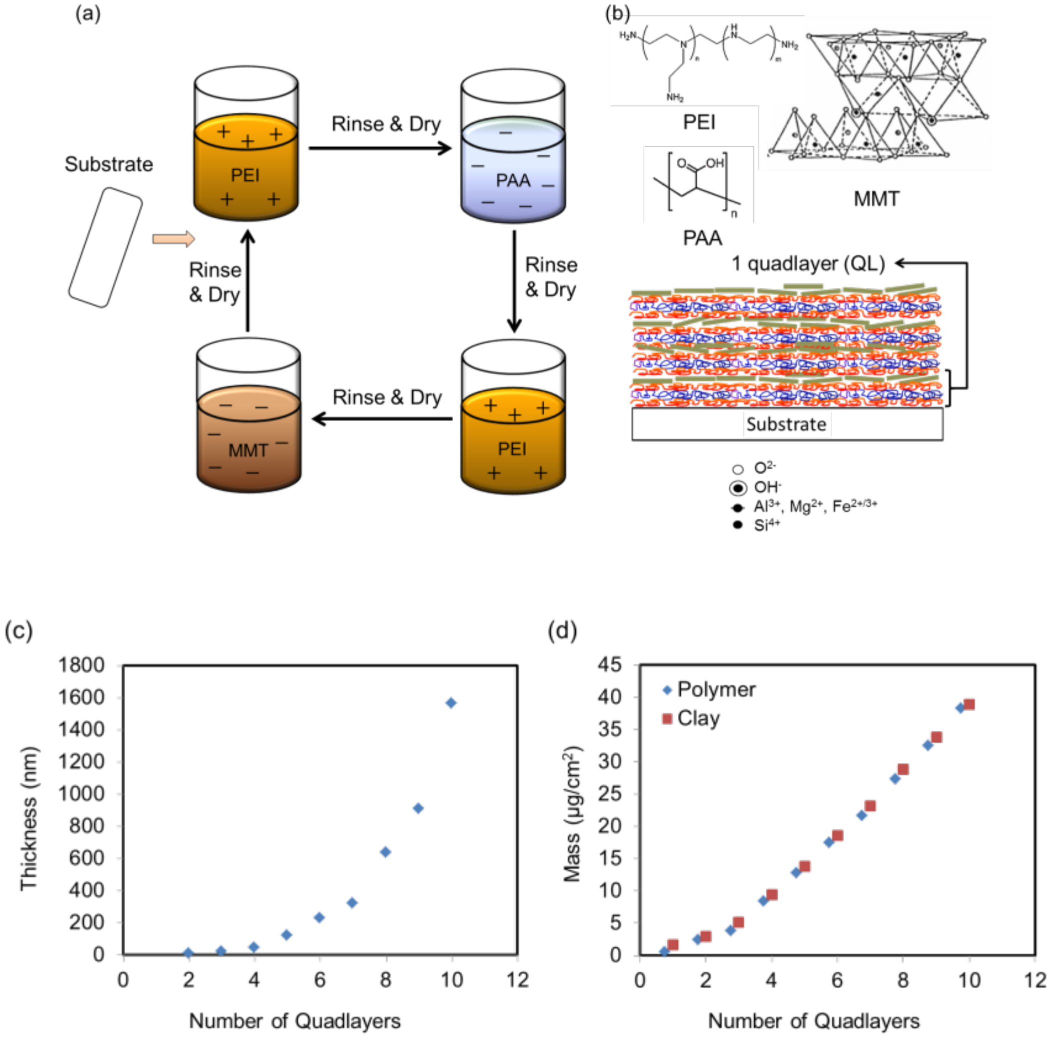

Figure 4.1. (a) Schematic of the quadlayer assembly process. (b) Materials used and cross-sectional illustration of the thin film structure. (c) Film growth as a function of quadlayers deposited. (d) Mass as a function of quadlayers deposited.[269]

4.2 Experimental

4.2.1. Materials

Branched polyethylenimine (Aldrich, St. Louis, MO) (MW ~ 25,000 g mol^{-1}) is a cationic polymer that was dissolved into 18.2 MΩ deionized water to create 0.1 wt% solutions. The pH was adjusted from its unaltered value (~10.5) to 10 by adding 1.0 M hydrochloric acid (HCl). Poly(acrylic acid) (Aldrich) (MW ~ 100,000 g mol^{-1}) is an anionic polymer that was prepared as a 0.2 wt% solution with deionized water. The pH of PAA was adjusted from its unaltered value (~3.1) to 4 by adding 1.0 M sodium hydroxide (NaOH). Anionic natural sodium montmorillonite (MMT) (trade name Cloisite Na+) (Southern Clay Products, Inc., Gonzales, TX) clay was prepared as a 1 wt% aqueous suspension. This suspension of high aspect ratio nanoplatelets ($l\ d^{-1}$ is 80 to 300)[201] was used at its natural pH (~9.7). The aqueous solutions were used to grow barrier film on a 51 µm (trade name Trycite 8001) polystyrene substrate (Dow, Midland, MI).

4.2.2. Layer-by-Layer Deposition

The PS substrate was rinsed with deionized water and methanol before use, then plasma-treated with a ATT0 Plasma Cleaner (Thierry Corp., Royal Oak, MI). Plasma treatment improves adhesion of the first polyelectrolyte layer by oxidizing the film surface.[202] The substrate was first dipped into the PEI solution for 5 minutes, followed by rinsing with deionized water for 30 seconds and drying with a stream of filtered air. After the first positively-charged layer was adsorbed, the substrate was dipped into PAA solution for another 5 minutes, followed by another rinsing and drying cycle. The substrate was then dipped into PEI and MMT solutions to form one “quadlayer”. Starting from the second deposition cycle, the remaining layers were deposited using one minute dip times. This process was carried out using home-built robotic systems.[203, 204] The pH of PEI and PAA is shown as a subscript next to the initials in the figures and text. For example, one quadlayer of PEI(pH=10)/PAA(pH=4)/PEI(pH=10)/MMT(unaltered pH of 9.7) is abbreviated as $(PEI_{10}/PAA_4/PEI_{10}/MMT)_1$.

4.2.3. Thin Film Characterization

Assembly thickness on silicon wafers was measured every quadlayer with a PHE-101 Discrete Wavelength Ellipsometer (Microphotonics, Allentown, PA) in absorbance mode, using a 632.8 nm laser at an incidence angle of 65°. Mass increments were measured each layer with a Research Quartz Crystal Microbalance (QCM) (Inficon, East Sycrase, NY) using a frequency range of 3.8 - 6 MHz. The 5 MHz quartz crystal was inserted in a holder and dipped into the solutions. After each deposition, the crystal was rinsed and dried and then left on the microbalance to stabilize for 5 minutes. Cross-sections of the quadlayer assemblies were imaged with a Tecnai F20 TEM (FEI, Hillsboro, OR), operated at 200 kV. Samples were prepared for imaging by embedding a piece of coated PET in epoxy prior to sectioning it with a diamond knife.

4.2.4. Gas Permeation System

Gas permeability coefficients of H_2 and He were measured using a constant-volume, variable-pressure method. Permeate flux was measured through a membrane by monitoring the pressure increase, in a closed vessel, using a pressure transducer. The film was mounted in a permeation cell and the upstream and downstream volumes were evacuated to de-gas the film. The valve connecting the permeation cell to the vacuum pump was then closed and a measurement of the vacuum leak rate in the downstream side was taken. Once the leak rate was determined, feed gas was introduced into the upstream side of the membrane and the pressure rise as a function of time in the downstream side was recorded. Gas permeabilities P_A (cm^3 (STP) cm cm^{-2} s^{-1} cmHg^{-1}) were calculated using the steady state pressure increase in a fixed downstream volume as:[270]

$$P_A = \frac{V_d l}{p_2 A R_g T}\left[\left(\frac{dp_1}{dt}\right)_{ss} - \left(\frac{dp_1}{dt}\right)_{leak}\right] \tag{4.1}$$

where V_d is the downstream volume in cm^3, l is the film thickness in cm, p_2 is the upstream absolute pressure in cmHg, A is the film area available for gas transport in cm^2, R_g is the gas constant, T is the absolute temperature in Kelvin and $(dp_1/dt)_{ss}$ and $(dp_1/dt)_{leak}$ are the steady state rates of pressure increase in the downstream volume at a specific upstream pressure and under vacuum. The vacuum leak rate $(dp_1/dt)_{leak}$ was less than 5% of steady state pressure increase rate $(dp_1/dt)_{ss}$.

The permeation cell is a 47 mm HP Filter Holder (Millipore, Billerica, MA, USA) with an area of 9.6 cm^2. The downstream pressure was always kept below 10 Torr in order to maintain an effectively constant pressure difference across the membrane. The pressure rise in the downstream volume was monitored using a Baratron 626B 100 Torr capacitance manometer (MKS, Andover, MA, USA). The calibrated downstream volume was 306 cm^3. A relief valve was used to prevent the downstream pressure from increasing above one atmosphere. This was necessary to prevent accidental over-pressurization of the transducer in the event of membrane rupture. The upstream pressure was varied between 4 – 6 atm and was measured using a PX409-250 pressure transducer (Omega Engineering, Stamford, CT USA). Measurements were carried out at room temperature using UHP grade gases. Swagelok VCR connections and VCO needle valve were used for downstream connections to minimize leaks. In order to achieve proper measurements, the leak maximum rate was kept below 10% steady state pressure increase rate $(dp_1/dt)_{ss}$ for the gas being tested.

4.3 Results and Discussion

4.3.1. Multilayer Film Growth

Unlike most LbL systems, which grow linearly, the exponential growth shown in Figure 4.1c is attributed to interdiffusion of the weak polyelectrolytes in this quadlayer assembly.[51, 63, 66, 184] The thin growth observed in the first few QL is strongly affected by the substrate, suggesting the deposited materials may not have full coverage during this ‘island growth’ period.[184, 271] After the initial growth, interdiffusion of PEI and PAA takes over because both are in their low charge state at pH 10 and pH 4, respectively. Clay concentration decreases as the number of QL increases, as shown in Table 4.1 and Figure 4.1d, attributed to the additional PEI and PAA deposited through interdiffusion.

4.3.2. Nanobrick Wall Thin Film Structure

Figure 4.2 shows TEM cross-sectional images of PEI/PAA/PEI/MMT assemblies, showing how clay concentration decreases at higher numbers of quadlayers. The dark lines in Figure 4.2a represent individual platelets, revealing that they are oriented parallel to the substrate and well exfoliated. Although clay is deposited five times in this 5 QL film, more than five clay layers are observed. Both exfoliated platelets and intercalated stacks can been seen, similar to the results found in other studies.[51, 66] The 10 QL film shows similar structure to the 5 QL film in the initial quadlayers (Figure 4.2b), but later exhibits increasing clay spacing (Figure 4.2c). The spacing reaches ~150 nm in the final quadlayers, suggesting a decreased clay concentration. Based on these images, it appears that the interdiffusion of PEI and PAA is able to expand the clay stacks and diffuse through the layers of platelets. These TEM images confirm that a nanobrick wall structure is generated by this LbL deposition (Fig. 4.2).

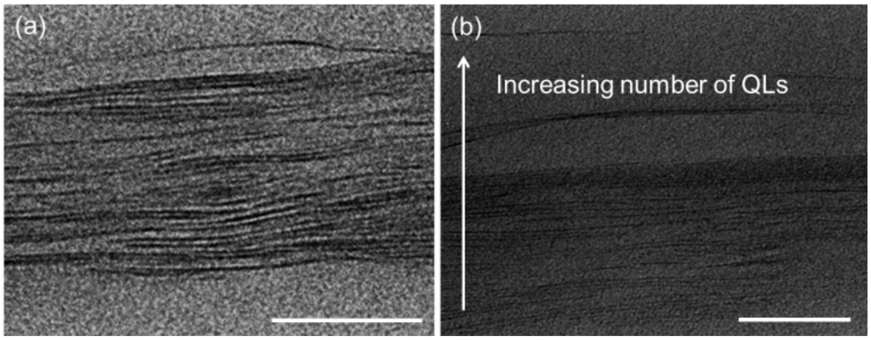

Figure 4.2. TEM cross-sectional images of (a) 5 and (b) (c) 10 PEI/PAA/PEI/MMT QL. (b) is the portion of the film closest to the PS substrate, while (c) is furthest away. The white scale bar in each figure represents 50 nm.[269]

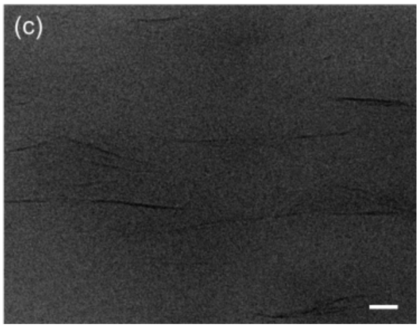

Figure 4.2. Continued.

4.3.3. Gas Barrier of Quadlayer Assemblies

Figure 4.3 shows H_2 and He permeability of quadlayer assemblies on a 51 μm polystyrene film. The overall He and H_2 permeability is observed to decrease by three orders of magnitude relative to the bare substrate, while the overall film thickness increases by only 0.2% (Table 4.1). Increasing the number of QL from 5 to 10 does not improve the barrier properties. This lack of improvement may be attributed to the dramatically expanded clay spacing and associated concentration reduction (as confirmed by analysis of growth profiles and film morphology in Figures 4.1c and 4.2, respectively), which diminishes the tortuous path afforded by the nanobrick wall structure. The 5 QL nanocomposite, with a thickness of 122 nm, exhibits a H_2 permeability one order of magnitude lower than laminated EVOH film,[265] and a He permeability three orders of magnitude lower than metallized polyolefin/polyester.[263]

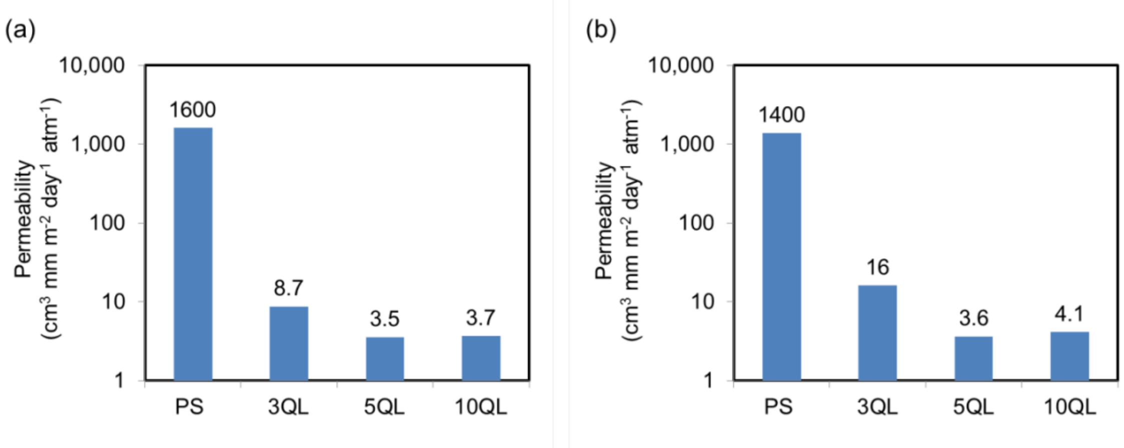

Figure 4.3. Permeability of (a) hydrogen and (b) helium as a function of quadlayers deposited on a 51 μm polystyrene substrate.[269]

Table 4.1. Permeability, film thickness, and clay concentration of quadlayer assemblies deposited on 51 μm polystyrene.

	Film Thickness (nm)	Clay loading (wt%)	Transmission Rate ($cm^3\ m^{-2}\ day^{-1}\ atm^{-1}$)		Permeability ($cm^3\ mm\ m^{-2}\ day^{-1}\ atm^{-1}$)	
			H_2	He	H_2	He
PS			31000	27000	1600	1400
3QL	48.6	54.9	170	320	8.7	16
5QL	122	34.7	69	71	3.5	3.6
10QL	1564.8	26.8	71	78	3.7	4.1

4.4 Conclusions

In summary, the present study represents the first demonstration of a layer-by-layer deposited film with low hydrogen and helium permeability. The impermeable clay platelets, together with highly interdiffused PEI and PAA mortar, formed a nanobrick wall structure that imparts significant light gas barrier.

Permeability of both hydrogen and helium decreased as the number of quadlayers increased, showing one to three orders of magnitude improvement compared to commercial barriers. The uniqueness of this polymer/clay barrier thin film is due to the high clay loading and strong ionic interactions between polyelectrolytes. The excellent performance of this thin film, combined the simplicity of layer-by-layer deposition, makes this light gas barrier coating an exciting opportunity for several packaging and protective applications.

CHAPTER V

IMPROVED GAS BARRIER/SEPARATION OF GRAPHENE OXIDE-BASED MULTILAYER THIN FILMS

5.1 Introduction

Improving gas barrier in packaging films is an ongoing endeavor. For the past two decades, technologies such as SiO_x, composite films and metallized plastic films have been successfully used to protect various items (food, electronics, etc.) from oxygen and moisture.[16, 95, 127, 230, 243, 272-276] In many cases, these barrier solutions require complex processing conditions,[277, 278] exhibit poor optical and/or mechanical behavior,[279, 280] and/or suffer from pinholes.[232, 277, 280] Additionally, metal applied by vapor deposition can also pollute the environment and negatively impact human health.[279] More recently, super gas barrier thin films have been deposited from water using layer-by-layer (LbL) assembly.[64, 180, 197] These environmentally-friendly nanocoatings overcome many of the limitations described for more traditional gas barriers.

High gas barrier is most often realized by using clay as one of the ingredients. [89-91] The electrostatic interaction between polyelectrolyte and clay forces the platelets to deposit in a highly oriented fashion, creating a long tortuous pathway that reduces gas permeability,[159] but the presence of hydrophilic polymers causes plasticization in the presence of moisture, resulting in an increase in gas permeability.[281] More hydrophobic platelets, such as graphene, have been examined to reduce this moisture sensitivity.[282, 283] Two dimensional graphene (sp^2 carbon atom) possesses excellent electrical,[284, 285] mechanical[286, 287] and thermal properties,[288] making it an interesting platelet for LbL assembly. Considering the difficulty to exfoliate graphene, due to its strong van der Waals interactions, graphene oxide (GO) is a more appealing starting material.[289, 290] The hydroxyl and carboxyl groups on the GO surface enable aqueous deposition through electrostatic or hydrogen bonding (see structure in Figure 5.1 (b)).[291] In most cases, GO is paired with a cationic material to create a "bilayer" (BL) assembly.[183, 247] These multilayer assemblies exhibit low gas permeability, but contain a high GO concentration (~90 wt%),[65] which is costly and produces strongly colored films.

In the present study, chitosan (CH) and poly(acrylic acid) (PAA) were used to fabricate a "quadlayer" (QL) assembly with graphene oxide. Discrete, equally spaced layers of polymer and GO were observed in a TEM cross-section of the film, indicating linear growth. The single polymer layer between GO is now replaced by an interdiffused polymer matrix. The pH deviation between CH and PAA not only influences degree of ionization of PAA, but creates a denser polymer layer. A 5 CH/PAA/CH/GO QL film (< 50 nm) exhibits an oxygen permeability of 3.9×10^{-20} cm^3 cm cm^{-2} Pa^{-1} s^{-1} under dry conditions. This barrier can be maintained in a high humidity environment after thermally reducing graphene oxide. It was discovered that this reduced GO assembly could also separate gas molecules with different sizes. With a H_2/CO_2 selectivity of 215, this thin film membrane outperforms most known separation membranes. The advantages of this quadlayer assembly, including its low GO concentration (< 50 wt%)

and excellent barrier/separation behavior, make it a promising system for packaging (food, pharmaceuticals and electronics) and gas separation.

5.2 Experimental

5.2.1. Materials

Cationic chitosan (Mw 60,000 g mol^{-1}, degree of deacetylation 95%) (G.T.C. Bio Corp., Qingdao, China) was dissolved into 18.2 MΩ deionized water to create a 0.1 wt% solution. pH was adjusted to 3.5, 4.5 and 5.5 using a previously described method.[292] Anionic poly(acrylic acid) (Mw 100,000 g mol^{-1}) (Sigma-Aldrich, Milwaukee, WI) was used to make a 0.2 wt% solution that pH was adjusted to 3, 4 and 5. All pH values were adjusted by adding 1.0 M hydrochloric acid (HCl) or 1.0 M sodium hydroxide (NaOH). Graphene oxide (aspect ratio 300-800) (CheapTubes, Brattleboro, VT) was exfoliated in deionized water via sonication (10W) for 10 minutes with a MISONIX XL-2000 tip sonicator (Qsonica, Melville, NY). A 0.1 wt% graphene oxide suspension was used as an anionic component at its natural pH (~3.2).

5.2.2. Substrates

Single-side-polished (100) silicon wafers (University Wafer, South Boston, MA) were used as substrates for ellipsometry and scanning electron microscopy (SEM). Ti/Au quartz crystals, with a resonance frequency of 5 MHz, were purchased from Maxtek Inc. (Cypress, CA) and used as deposition substrates for quartz crystal microbalance (QCM) characterization. Silicon wafers were cleaned with a 3:1 ratio of 30% hydrogen peroxide to 99% sulfuric acid and stored in deionized water. These substrates were then rinsed with acetone and deionized water before use. *Caution: Piranha solution reacts violently with organic material therefore needs to be handled properly*. 179 µm thick poly(ethylene terephthalate) (PET) film (trade name ST505, Dupont–Teijin) was purchased from Tekra (New Berlin, WI). PET was rinsed with deionized water and methanol, then corona-treated with a BD-20C Corona Treater (Electro-Technic Products Inc., Chicago, IL) to impart a strong negative surface charge.

5.2.3. Layer-by-Layer Deposition

Figure 5.1 illustrates the layer-by-layer assembly procedure. A layer of CH was first deposited by dipping the substrate into the solution for 5 minutes, followed by rinsing with deionized water for 30 seconds and drying with a stream of filtered air. The substrate was then dipped into PAA solution for another 5 minutes, followed by another rinsing and drying cycle. The quadlayer was completed with one more layer of CH and GO. Starting from the second deposition cycle, the remaining layers were deposited using one minute exposures to each solution. This process was carried out with home-built robotic systems.[204, 293] pH of CH and PAA are shown as a subscript next to their initials in the figures and text. For example, one quadlayer of CH(pH=5.5)/PAA(pH=3)/CH(pH=5.5)/GO (unaltered pH of 3.2) is abbreviated as $(CH_{5.5}/PAA_3/CH_{5.5}/GO)_1$. Quadlayer assemblies were heated at 175 ºC for 90 minutes to convert GO into reduced-GO (rGO).

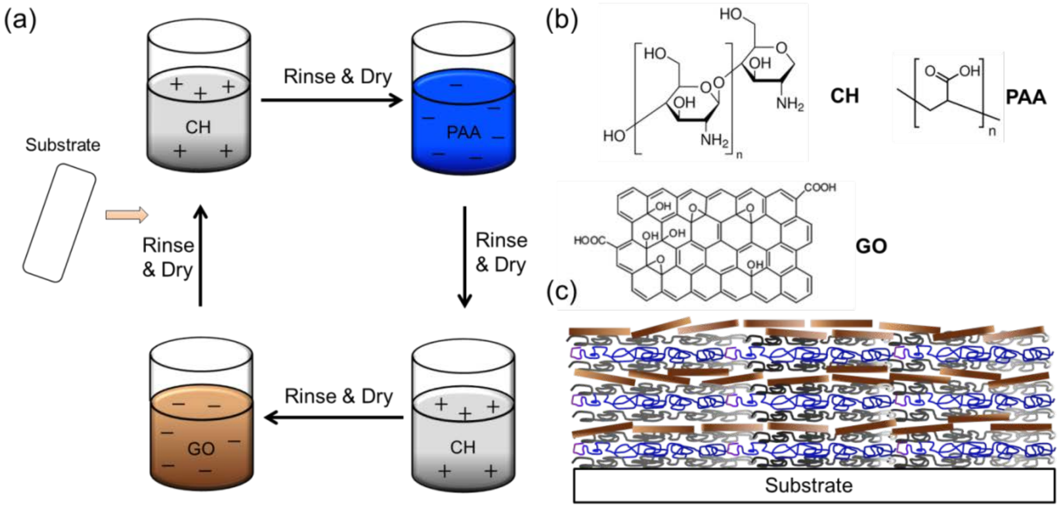

Figure 5.1. Illustration of (a) LbL process (b) materials used and (c) nanobrick wall structure built from chitosan/poly(acrylic acid)/chitosan/graphene oxide quadlayers.

5.2.4. Thin Film Characterization

Film thickness was measured every quadlayer with a PHE-101 Discrete Wavelength Ellipsometer (Microphotonics, Allentown, PA), using a 632.8 nm laser at an incidence angle of 65º. FTIR spectra of LbL films were measured with a Bruker Optics ALPHA-P 10098-4 spectrometer in ATR mode. Origin software was used to deconvolute PAA peaks in its protonated (COOH) and ionic (COO^-) forms to derive degree of ionization (DOI), as described in our previous study.[294] To avoid the absorbance peaks of the silicon oxide substrate and carboxylic acid of GO, 100 bilayers (BL) of CH/PAA (~1.5 μm) were used for FTIR analysis. Cross-sections of the quadlayer assemblies were prepared by embedding the film in Epofix resin (EMS, Hatfield, PA) overnight, followed by cutting with an Ultra 45º diamond knife (Diatome, Hatfield, PA). Sections were imaged with a Tecnai G2 F20 TEM (FEI, Hillsboro, OR), operated at 200 kV. Surface structure of the coated silicon wafers were imaged with a JSM-7500F JEOL field-emission scanning electron microscope (FESEM, Tokyo, Japan). OTR testing was performed by MOCON (Minneapolis, MN) in accordance with ASTM D-3985,[207] using an Mocon Oxtran 2/21 ML instrument at 23 ºC and 0% (or 100%) RH. Permeation of H_2 and CO_2 were tested via Mocon Multi-Tran 400 and Permatran C4/41 instruments at 23 ºC and 0% RH (according to ISO 15105 and ASTM F2476-05).[295, 296] Carbon bonding was characterized with a PHI Quantera XPS (ULVAC-PHI, Chanhassen, MN).

5.3 Results and Discussion

5.3.1. Film Growth

Figure 5.2 shows the thickness of chitosan/poly(acrylic acid)/chitosan/graphene oxide quadlayers under varying pH combinations. The linear growth observed in these assemblies is verified by the cross-sectional TEM image (Figure 5.2(c)). The contrast between polymer and GO is low due to the low electron density in both, so resolution is sacrificed in order to distinguish the two. The five dark lines in this TEM image represent GO layers deposited, clearly showing this film to have a highly oriented structure. Not only does the thickness of the $(CH_{5.5}/PAA_3/CH_{5.5}/GO)_5$ film measured by TEM (~44 nm) agree with ellipsometry, GO spacing derived from the electron signal profile (GO located at 6, 13, 21, 27 and 33 nm in Figure 5.2(d)) also confirms linear growth. Figure 5.3 showed mass deposited for these quadlayer recipes, with a linear trend similar to the ellipsometry results. Concentration of GO in these 5QL films were listed as well, all of them showing a GO concentration ~48% except for $CH_{5.5}/PAA_5/CH_{5.5}/GO$. The low GO concentration of $CH_{5.5}/PAA_5/CH_{5.5}/GO$ was seen in the SEM images and will be presented in the following section.

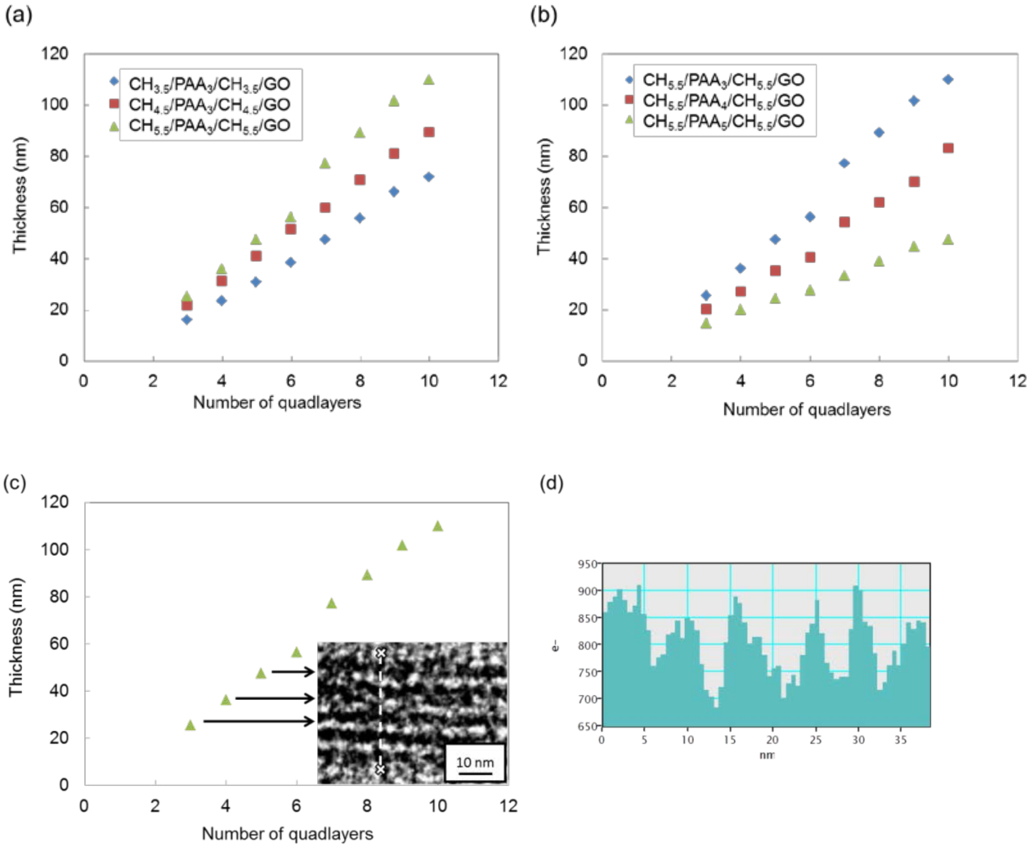

Figure 5.2. Thickness of CH/PAA/CH/GO as a function of quadlayers deposited with varying (a) pH of CH and (b) pH of PAA. (c) Film growth of $CH_{5.5}/PAA_3/CH_{5.5}/GO$ compared with TEM cross-section of 5QL film. (d) Electron signal profile scanned through the white dotted section in (c). Valley points indicate position of GO layers.

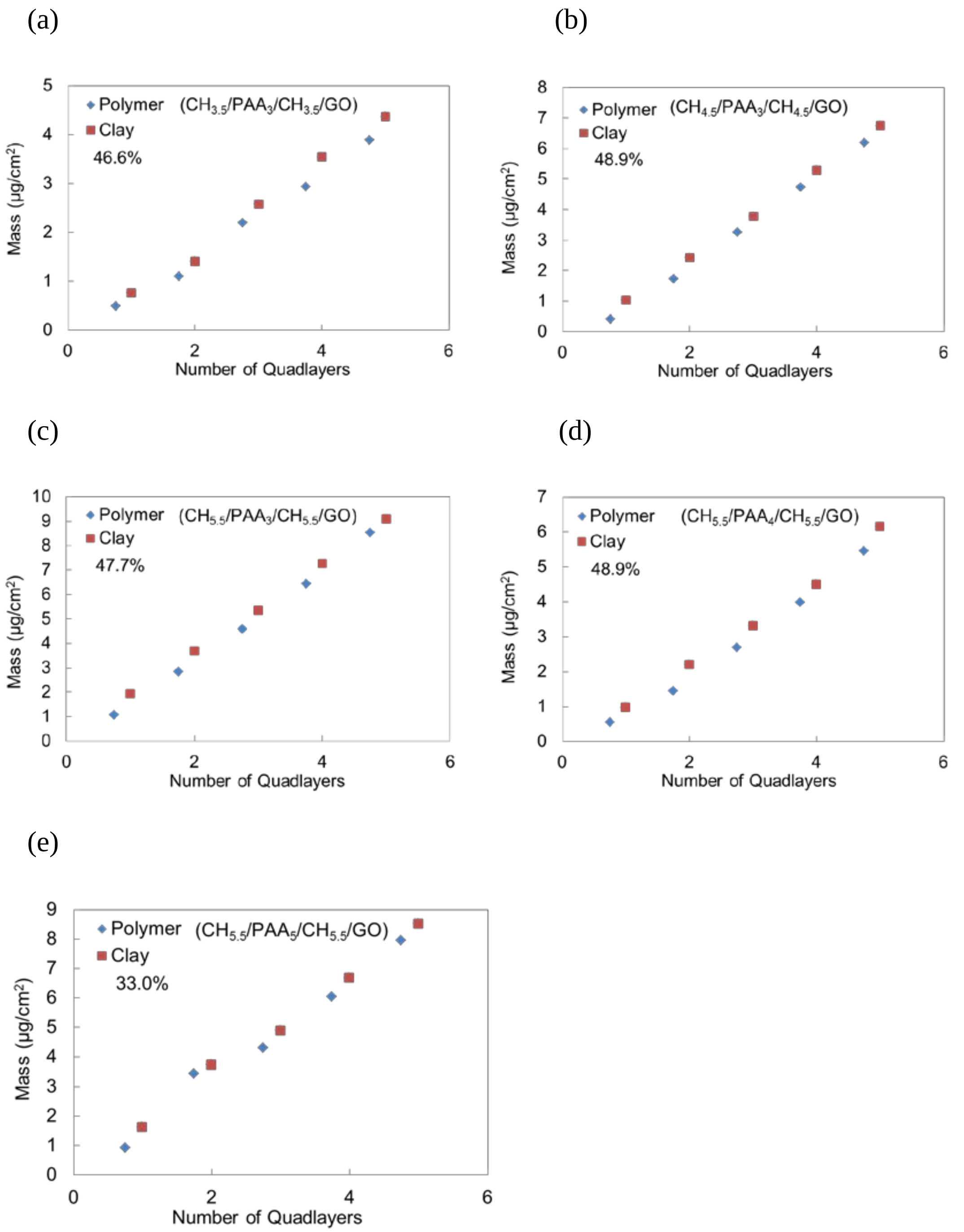

Figure 5.3. Mass as a function of quadlayers deposited: (a) $CH_{3.5}/PAA_3/CH_{3.5}/GO$ (b) $CH_{4.5}/PAA_3/CH_{4.5}/GO$ (c) $CH_{5.5}/PAA_3/CH_{5.5}/GO$ (d) $CH_{5.5}/PAA_4/CH_{5.5}/GO$ and (e) $CH_{5.5}/PAA_5/CH_{5.5}/GO$. Concentration of GO (5 QL) is listed as well.

The variation of thickness per QL increment with pH, from 4.8 to 11.0 nm per QL, is caused by changes in conformation of the polyelectrolytes. For the $CH_{5.5}/PAA_5/CH_{5.5}/GO$ and $CH_{3.5}/PAA_3/CH_{3.5}/GO$ assemblies, CH and PAA have similar pH, suggesting that one of the polyelectrolyte is in a lower charged state (CH at pH 5.5 or PAA at pH3) with a globular conformation to achieve thicker growth in the former. The counter polyelectrolyte (PAA at pH 5 or CH at pH 3.5), being highly ionized, has a linear chain conformation due to the electrostatic self-repulsion.[198] With only a small change in environmental pH, the counter polyelectrolyte remains highly ionized, so the deposited polymer layer is thin. On the other hand, $CH_{5.5}/PAA_3/CH_{5.5}/GO$ starts the deposition in a pH 5.5 solution. This partially charged chitosan is deposited onto the substrate with a globular conformation.[198] During PAA deposition, amine groups of CH not involved in bonding to the substrate (or preceding layer) are likely to be ionized because of the acidic environment, creating additional positive charges. In this case, poly(acrylic acid) with only a few ionized carboxylic acid groups is also adsorbed in a globular chain conformation. This same process occurred again for the second CH deposition. Deposition of globular, lowly charged chains is the reason for the thickness increment to increase 100% relative to assemblies prepared with similar CH and PAA pH. The transition of polyelectrolytes from solution to multilayer film not only changes pKa (pKa of CH increased and pKa of PAA decreased), but the degree of ionization increases as well,[206] which will be discussed later. The additional charges generated during each deposition step also serves to attract more polyelectrolytes into the assembly, forming an interpenetrating network known as a “scramble salt” structure.[297] Formation of scramble salt will influence barrier properties as well and will be elaborated in the following paragraphs.

5.3.2. Film Morphology

SEM images of 1 QL assembly surfaces are shown in Figure 5.4. The wrinkles confirm the presence of GO and these images suggest GO deposition is uniform over the surface. By fixing the pH of CH at 5.5, the level of wrinkling diminishes as the pH of PAA increases. In $CH_{5.5}/PAA_5/CH_{5.5}/GO$, there are few observable wrinkles, suggesting less GO coverage. When the pH of PAA is held constant at 3, increasing CH pH from 3.5 to 5.5 does not change the coverage of GO very much. The same trends are also found in the gas barrier of these films (i.e., greater GO coverage correlates to reduced oxygen permeability).

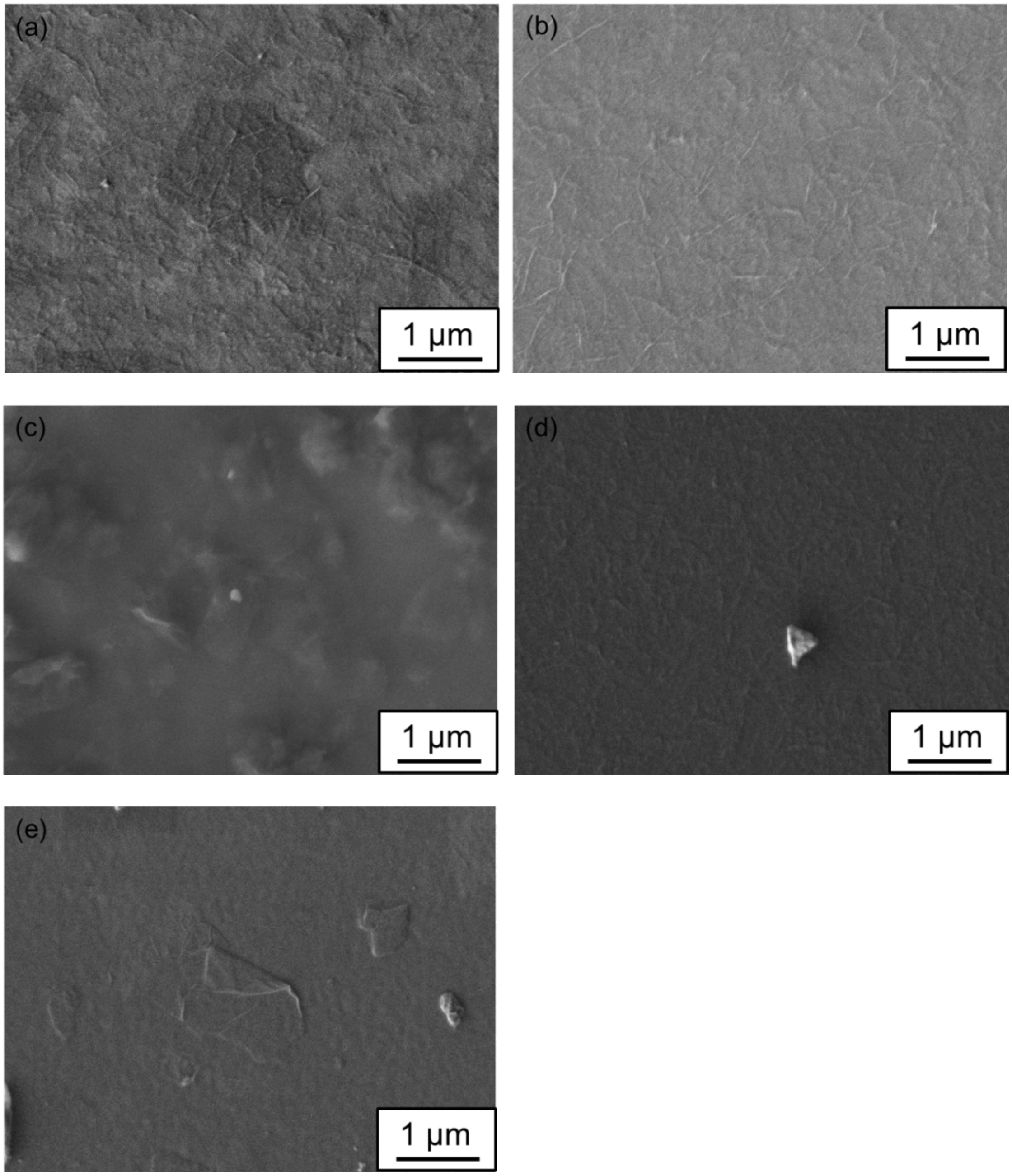

Figure 5.4. SEM surface images of one quadlayer of (a) $CH_{3.5}/PAA_3/CH_{3.5}/GO$ (b) $CH_{4.5}/PAA_3/CH_{4.5}/GO$ (c) $CH_{5.5}/PAA_3/CH_{5.5}/GO$ (d) $CH_{5.5}/PAA_4/CH_{5.5}/GO$ and (e) $CH_{5.5}/PAA_5/CH_{5.5}/GO$.

As mentioned earlier, the interaction between chitosan and poly(acrylic acid) generates a scramble salt structure through interdiffusion and ionization.[199, 200] FTIR spectra of CH/PAA assemblies, shown in Figure 5.5, were used to compare the degree of interdiffusion. Degree of ionization of PAA was derived by dividing peak area of its ionic form (COO^-) by the total area of ionic and protonated form (COOH), which are 1550 and 1715 cm^{-1}, respectively. The peak at 1650 cm^{-1} in these spectra represents primary amine (NH_2) bending of chitosan.[298, 299] For $CH_{3.5}/PAA_3$ and $CH_{5.5}/PAA_5$, DOI is less than 40% because CH and PAA are at similar pH. In this case, the highly charged polyelectrolyte (CH at 3.5 or PAA at pH 5) is unable to ionize the counter ion. As the difference in pH increases to 1.5, as it does for $CH_{4.5}/PAA_3$ and $CH_{5.5}/PAA_4$, there is greater ability for the two polymers to interdiffuse and lock in the structure by inducing an increased ionization. When the pH difference is 2.5, as it is for $CH_{5.5}/PAA_3$, the initially low-charged polyelectrolytes highly interdiffuse and then highly ionize one another. This creates a dense polymer layer and also facilitates deposition of GO, both of which impart gas barrier.

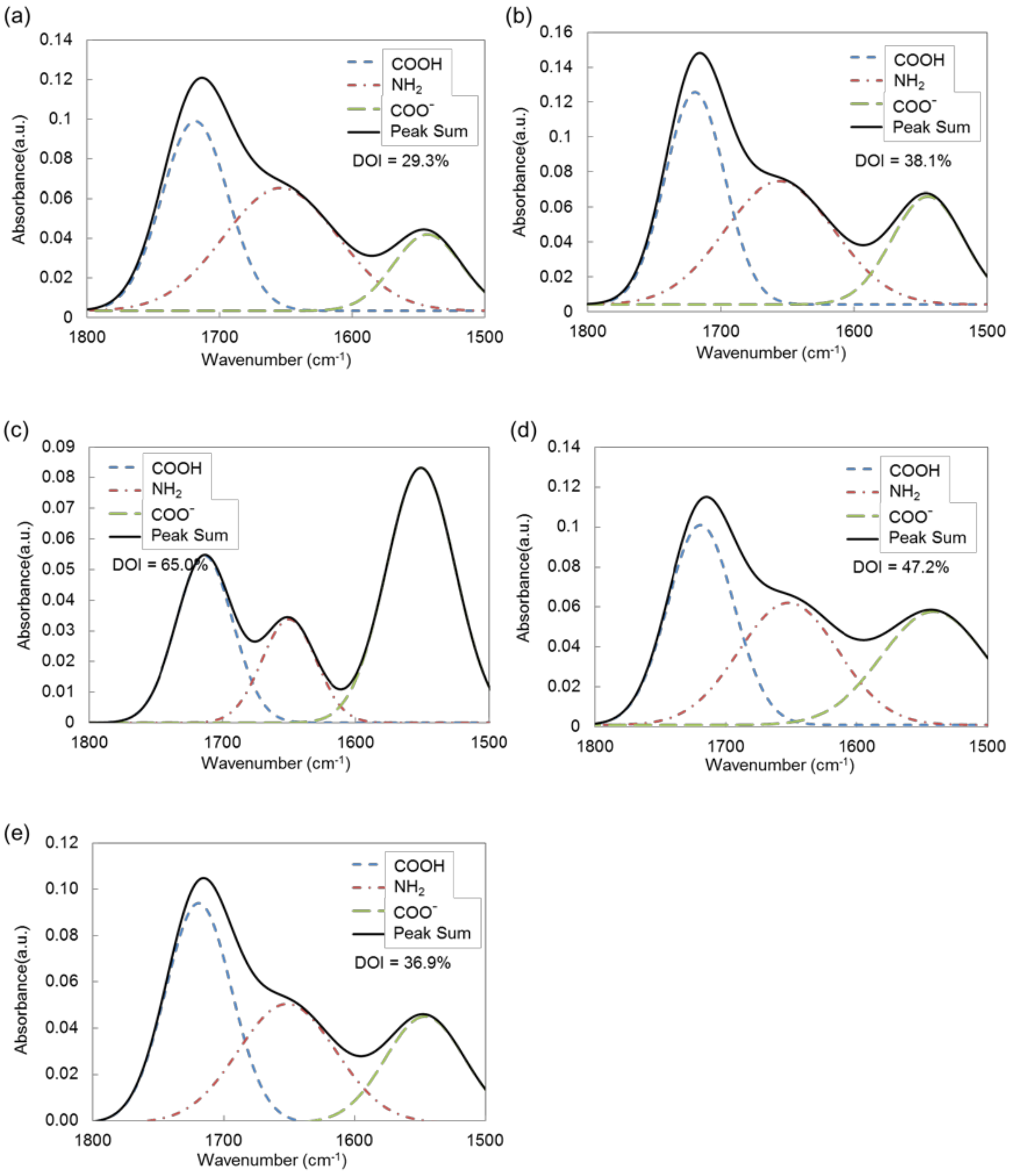

Figure 5.5. FTIR spectra of (a) $(CH_{3.5}/PAA_3)_{100}$ (b) $(CH_{4.5}/PAA_3)_{100}$ (c) $(CH_{5.5}/PAA_3)_{100}$ (d) $(CH_{5.5}/PAA_4)_{100}$ and (e) $(CH_{5.5}/PAA_5)_{100}$.

5.3.3. Gas Barrier and Separation

Oxygen transmission rates (OTR) for quadlayer films assembled with varying pH are summarized in Table 5.1. All of the 5QL nanocoatings improved the oxygen barrier of the PET substrate (OTR = 8.4 $cm^3\ m^{-2}\ day^{-1}atm^{-1}$). Oxygen transmission rate decreases as the pH difference between CH and PAA increases in these assemblies, with $(CH_{5.5}/PAA_3/CH_{5.5}/GO)_5$ exhibiting the lowest OTR (~0.34 $cm^3\ m^{-2}\ day^{-1}atm^{-1}$). This 48 nm coating reduced OTR by a factor of more than 20 because both low-charged polyelectrolytes ionized one another during extensive interdiffusion, forming a highly dense layer with uniform coverage by GO platelets. By tailoring assembly structure with deposition pH, oxygen permeability as low as 3.9×10^{-20} $cm^3\ cm\ cm^{-2}\ Pa^{-1}\ s^{-1}$ is achieved. This value matches SiO_x and is two orders of magnitude lower than 25μm ethylene-vinyl alcohol film, another commonly used oxygen barrier.[230, 231, 233]

Table 5.1. Oxygen transmission rate and permeability of five quadlayer assemblies on 179 μm PET film.

Assembly	OTR (Total) ($cm^3\ m^{-2}\ day^{-1}\ atm^{-1}$)	P (Film) ($10^{-19}\ cm^3\ cm^{-1}\ cm^{-2}\ Pa^{-1}\ s^{-1}$)	Film thickness (nm)
$(CH_{3.5}/PAA_3/CH_{3.5}/GO)_5$	1.23	1.0	30.9
$(CH_{4.5}/PAA_3/CH_{4.5}/GO)_5$	1.18	1.3	41.2
$(CH_{5.5}/PAA_3/CH_{5.5}/GO)_5$	0.34	0.39	47.5
$(CH_{5.5}/PAA_4/CH_{5.5}/GO)_5$	1.33	1.3	35.2
$(CH_{5.5}/PAA_5/CH_{5.5}/GO)_5$	4.03	4.3	24.5

This exceptional gas barrier is further improved with thermal reduction of graphene oxide. The GO used here contains 36.2% sp^2 carbon bonding (Fig. 5.6). After thermal reduction at 175 ºC for 90 minutes, a portion of C-O (C-OH and C-O-C) and carbonyl (C=O and COOH) bonding was converted to sp^2 (36.2% to 49.8%), resulting in more hydrophobic, conjugated, two-dimensional platelets. The $(CH_{5.5}/PAA_3/CH_{5.5}/rGO)_5$ assembly OTR remained the same as $(CH_{5.5}/PAA_3/CH_{5.5}/GO)_5$ at 0% RH, but it maintained its higher barrier at 100% RH, while the unreduced $(CH_{5.5}/PAA_3/CH_{5.5}/GO)_5$ was degraded by one order of magnitude, as shown in Figure 5.7 (a). It is believed that rGO makes the assembly less sensitive to moisture, which reduces thin film swelling under high humidity. This ability to maintain barrier under humid conditions surpasses that observed for polymer/clay assemblies.[159, 226] When compared to polyethyleneimine (PEI)/GO bilayer (BL) assemblies,[65] the quadlayer films in this study exhibit similar OTR at 0% RH with much lower GO concentration (90 wt% relative to less than 50 wt%). This is believed to be due to the greater GO platelet layer spacing created by the additional polymer layer, which causes gas molecules to spend more time wiggling between them.[110, 181, 197] The ionized CH and PAA create a denser layer that also contributes to improved barrier.

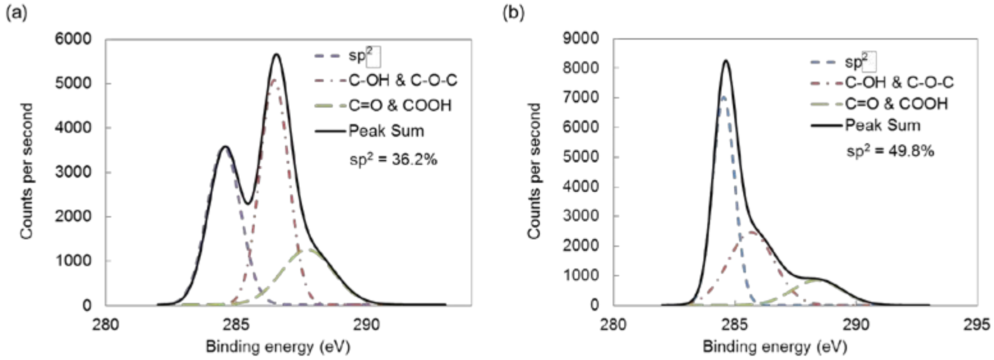

Figure 5.6. C1s XPS spectra of (a) graphene oxide and (b) thermally reduced graphene oxide.

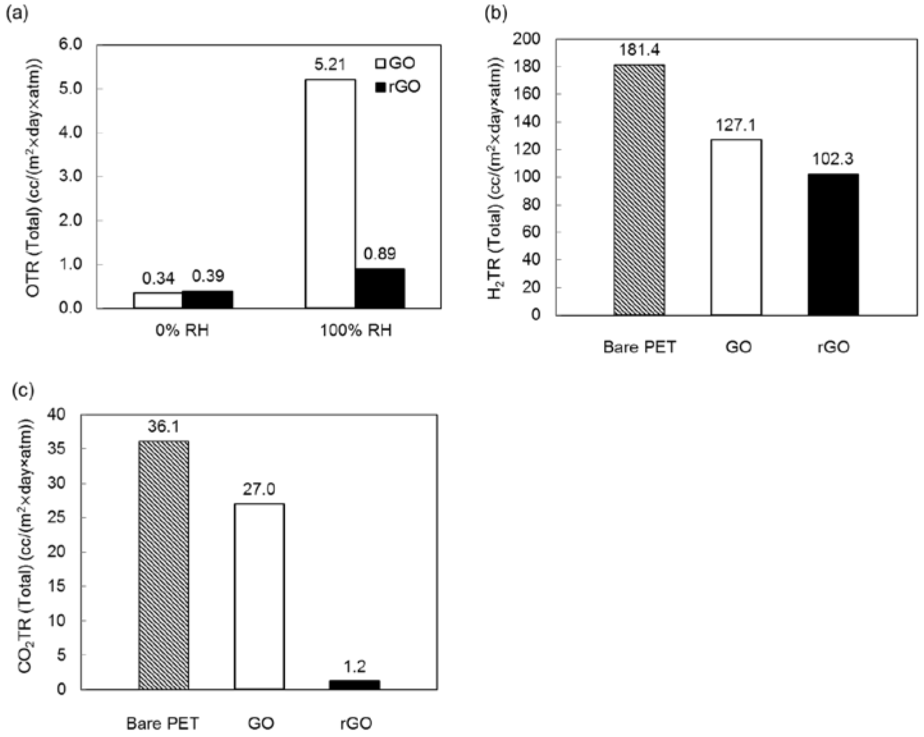

Figure 5.7. (a) Oxygen transmission rate of $(CH_{5.5}/PAA_3/CH_{5.5}/GO)_5$ on PET, under 0% and 100% RH. (b) Hydrogen and (c) carbon dioxide transmission rate of $(CH_{5.5}/PAA_3/CH_{5.5}/GO)_5$ on PET under 0% RH.

These same quadlayer assemblies can separate gases based on molecular size. Figure 5.7 shows hydrogen (H_2TR) and carbon dioxide (CO_2TR) transmission rates measured at 23 ºC and 0% RH. While H_2TR was reduced ~40% for GO and rGO films, CO_2TR was reduced from 25% to 97%, compared to the bare PET substrate, after thermal reduction. The more two-dimensional nature of rGO decreased the gaps between adjacent platelets and was enough to slow CO_2 transport. Figure 5.8 shows the separation of 5QL $CH_{5.5}/PAA_3/CH_{5.5}$/GO assemblies before and after thermal reduction. Quadlayer separation performance is placed in context with the Robeson's upper-bound limit[20, 21] and many of the best mixed matrix membranes (MMM), zeolitic imidazolate frameworks (ZIFs) and metal organic frameworks (MOFs).[195] The quadlayer H_2/CO_2 selectivity (α) increases from 5 to 215 after reducing GO, which outperforms the new Robeson's upper-bound limit (trade-off between gas permeability and selectivity, which is determined by sizes and condensabilities of gas pair).[21] This high H_2/CO_2 selectivity suggests that the pore structure in this assembly (a combination of CH/PAA matrix free volume and voids between GO platelets) creates a size-selective film that is able to separate gas molecules smaller than H_2 (2.89 Å) and larger than CO_2 (3.30 Å).[300] Excellent separation and low energy consumption should make these quadlayer films useful for applications requiring hydrogen recovery,[301] ammonia purge gas recovery[302] and carbon dioxide removal.[303]

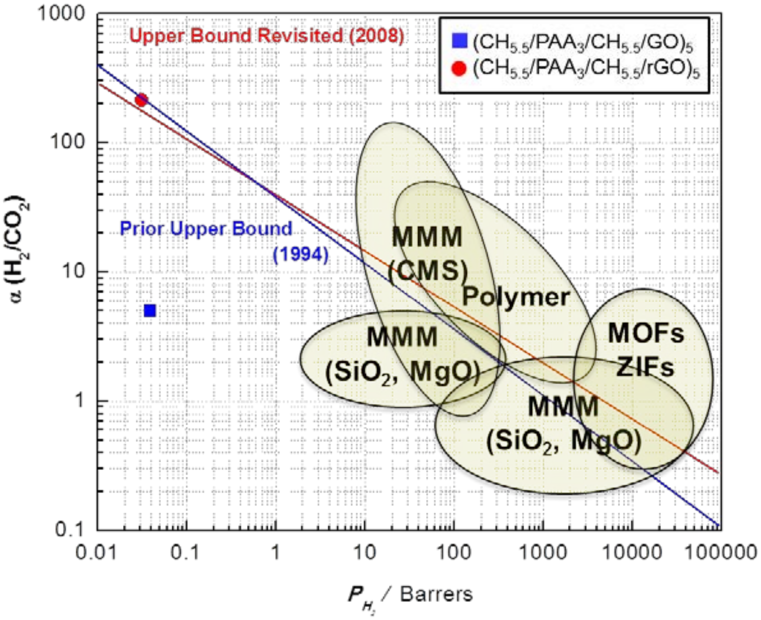

Figure 5.8. H_2/CO_2 selectivity of 5QL $CH_{5.5}/PAA_3/CH_{5.5}/GO$ in relation to the best polymer and mixed matrix membranes (MMM), including carbon molecular sieves (CMS). Robeson's upper bound for H_2/CO_2 separation is included to compare performance of membranes.

5.4 Conclusions

A graphene oxide-based quadlayer gas barrier/separation film was assembled using layer-by-layer technique. The ellipsometry and cross-sectional TEM images results revealed a linear growth with discrete GO layers, forming a "nanobrick wall" structure. pH of polyelectrolyte solutions were adjusted, eventually changing chain conformation and film thickness. Oxygen transmission rates were found to decrease as pH deviation between CH and PAA increase, which is verified by the better GO coverage shown in SEM images. $CH_{5.5}/PAA_3/CH_{5.5}/GO$ exhibited the best barrier performance because CH was highly ionized by the counter ion, therefore was able to attract more GO into the bulk film. By thermally reducing GO, OTR of the assemblies became less sensitive to moisture. Reduction of GO also increased H_2/CO_2 selectivity, the transformation of GO to a more two-dimensional structure is likely to fill up gaps between adjacent platelets, resulting CO_2 less permeable through the film. We believe this state-of-the-art composite film, based on its simplicity to fabricate and excellent barrier/separation properties bring out applications in packaging and gas separation.

CHAPTER VI*

HIGHLY SIZE-SELECTIVE IONICALLY CROSSLINKED MULTILAYER POLYMER FILMS FOR LIGHT GAS SEPARATION

6.1 Introduction

The production of inexpensive, high purity hydrogen remains a critical challenge for improving the sustainability of fossil fuels and for realizing renewable and clean energy sources capable of displacing fossil fuels. Dramatic increases in the demand for purified hydrogen for sulfur- and nitrogen-removal from “sour” crude oils is predicted in the coming decades,[304] as traditional sources of “sweet” or low-sulfur crude oils dwindle. Bio-refineries for producing “green” fuels from renewable sources are expected to further increase global demand for purified hydrogen.[305] Hydrogen itself promises a universal fuel derivable from any hydrocarbon resource, which may be converted to electrical energy using fuel cells at energy efficiencies surpassing those of combustion-based power systems with zero greenhouse gas emissions.[306] Industrial pressure-swing adsorption and cryogenic distillation processes for hydrogen purification are complex, energy-intensive and costly, and are incapable of satisfying purity requirements of many fuel cells.[307] In contrast, gas purification membranes offer a low-maintenance, energy-

---

*Reprinted with permission from “Advanced Materials” by Kim, D.; Tzeng, P.; Barnett, K. J.; Yang, Y. H.; Wilhite, B. A.; Grunlan, J. C. “Highly Size-Selective Ionically Crosslinked Multilayer Polymer Films for Light Gas Separation” *Adv. Mater.* **2013**, *26*, 746-751, Copyright [2015] by John Wiley and Sons.

efficient alternative to these processes and these membranes are capable of achieving hydrogen purities necessary for emerging energy technologies.[22]

Polymeric gas separation membranes combining low production costs with robust mechanical properties have found broad industrial application for O_2 and N_2 enrichment of air, upgrading of natural gas and hydrogen recovery from ammonia.[22] Dense polymeric membranes separate gas mixtures based upon disparities in individual species permeabilities, dictated by species solubility and mobility within the polymer material.[20, 21, 308] Size-selective polymer membranes rely upon differences in species mobility, which is directly related to molecular size.[308] In the absence of structure (i.e. in amorphous glassy or rubbery films), increasing the free volume of the polymer improves the permeability at the cost of reducing the permselectivity.[21, 308] In contrast, structured thin films assembled from molecular sieves,[309] zeolites,[310] metal-organic-frameworks (MOFs),[311] covalent-organic frameworks[312] and carbon nanotubes[313] combine nano-scale pores with high free volume in a uniform, nominally defect-free structure to avoid the trade-off between permeability and permselectivity.

Several strategies have been reported for incorporating structural aspects in polymeric systems in order to overcome the “upper bound” in separation performance, while retaining the traditional advantages of polymeric membranes. Mixed matrix membranes (MMMs) combine structural aspects of molecular sieves, zeolites or MOFs with homogeneous polymers.[151, 152] Polymers of intrinsic microporosity exploit structure and rigidity of individual macromolecules to inhibit chain packing during film synthesis, in turn realizing amorphous films with uniform pore structures.[314, 315]

Thermal re-arrangement of polymer segments in cast films allows introduction of tunable pore structures, combining high free volume with a "bottleneck" pore structure for maintaining high permselectivity.[316] Conversely, block copolymers formed from two or more incompatible polymers provide templates for producing highly ordered nanopore structures via etching of a sacrificial constituent from the as-cast film.[317]

In the present study, a branched polyethylenimine (PEI) / poly (acrylic acid) (PAA) system is assembled via LbL deposition and used for investigating light gas (H_2, CO, CO_2, O_2, N_2) separations using a flow-through membrane apparatus. Unlike other LbL systems that display linear growth due to a "ladderlike" deposition structure, PEI/PAA assembly appears to have a "scrambled salt" structure,[297] displaying exponential growth. The highly ionized PEI and PAA result in a highly interpenetrating network in both directions (from bulk film to solution, and vice versa). High modulus obtained by nanoindentation suggests high density as another evidence of the interpenetrated structure. This highly "ionically crosslinked" film is believed to be denser than traditional polymer films, making it an excellent candidate for gas barrier applications.

6.2 Experimental

6.2.1. Materials

Branched polyethylenimine (Aldrich, St. Louis, MO) (MW ~ 25,000 g mol^{-1}) was dissolved into deionized water (18.2 MΩ) for making 0.1 wt% solution. The pH was adjusted from its unaltered value (~10.5) to 10 by adding hydrochloric acid (HCl) (1.0

M). Poly(acrylic acid) (Aldrich) (MW ~ 100,000 g mol^{-1}) solution (0.2 wt%) was prepared with deionized water (18.2 MΩ). The pH of PAA was adjusted from its unaltered value (~3.1) to 4 by adding NaOH (1.0 M).

6.2.2. Substrates

Single-side-polished (100) silicon wafers (University Wafer, South Boston, MA) were used as substrates for thickness measurement. Silicon wafers were cleaned with a 3:1 ratio of 30% hydrogen peroxide to 99% sulfuric acid and stored in deionized water. These substrates were then rinsed with acetone and deionized water before use. *Caution: Piranha solution reacts violently with organic material therefore needs to be handled properly*. 179 µm thick poly(ethylene terephthalate) (PET) film (trade name ST505, Dupont–Teijin) was purchased from Tekra (New Berlin, WI). PET was rinsed with deionized water and methanol, then corona-treated with a BD-20C Corona Treater (Electro-Technic Products Inc., Chicago, IL) to impart a strong negative surface charge. Porous stainless steel (PSS) tubes (0.5 µm grade, OD: 0.5”, porous length: 2”, Mott Corporation) were used as supports for a PEI/PAA assembly. PSS supports were pretreated by immersion in an alkaline solution (sodium hydroxide, organic detergent, DI water) at 60 °C for 1 hour, followed by rinsing thoroughly with DI water and then drying at 120 °C for 2 hours. The pretreated PSS tubes were coated with nanopowder alumina (Sigma-Aldrich) by a vacuum pump which was connected to one end of the tube immersed in a nanopowder alumina solution (nanopowder alumina: alumina sol (~ 20%, Alfa-Aser), DI water (wt.% ratio: 1:7:0.1)), and the other end of the tube was plugged with a rubber stopper. After being annealed at 450 °C for 4 hours with a heating and cooling rate of 3 ^{o}C/min, the PSS tubes were airbrushed with alumina gel (dissolved alumina in nitric acid (Mallinckrodt Baker), followed by pH titration to near-neutral using ammonium hydroxide (Mallinckrodt Baker)) and annealed at the same condition described above.

6.2.3. Layer-by-Layer Deposition

The alumina-coated PSS tube was first dipped into the polycation solution (PEI) for 5 minutes, followed by rinsing with deionized water for 30 seconds and drying with a stream of filtered air, as shown in Figure 6.1. After the first positively-charged layer was adsorbed, the substrate was dipped into PAA solution for another 5 minutes, followed by another rinsing and drying cycle. One deposition cycle was defined as one 'bilayer'. Starting from the second deposition cycle, the remaining numbers of layers were created using one minute dip times. This process was carried out using home-built robotic systems.[203, 204]

6.2.4. Thin Film Characterization

Thickness of the films was measured by a P-6 profilometer (KLA-Tencor, Milpitas, CA). Gas permeation testing were carried out in two different ways. PEI/PAA multilayer films were first deposited on alumina-coated PSS tube and placed in a tube-and-shell assembly (Figure 6.2) in which the bore of the PSS tube (sweep) was supplied with helium and the annulus (feed) of the system with feed gases (H_2, CO, CO_2, O_2, N_2). Both sweep and feed gases were humidified with DI water to 3% RH prior to entering the membrane system. Permeate gas composition was continuously monitored via mass spectrometry (RGA 100, Stanford Research Systems). All gas permeation measurements were performed at room temperature (~20 ^{o}C) with permeate and retentate volumes maintained at atmospheric pressure. The permeance (P_i/t) of gas species (i) is calculated from Equation (1),

$$F_i = \frac{P_i}{t}(p_{i,f} - p_{i,s}) \tag{6.1}$$

where F_i is gas (i) permeation rate (mol m^{-2} sec^{-1}), t is membrane thickness (m), P_i is permeability (mol m^{-1} sec^{-1} Pa^{-1}), and $p_{i,f}$, $p_{i,s}$ are partial pressure (Pa) of gas i in the feed and sweep sides, respectively. Gas selectivity ($\alpha_{i/j}$) is given by the ratio of permeability (P_i/P_j) of two gas species (i,j). PEI/PAA assemblies were deposited on PET and tested by MOCON (Minneapolis, MN) as well. Gas permeation tests were performed in accordance with ASTM D-3985,[207] using Oxtran 2/21 ML for oxygen, Permatran-C 4/41 ML for carbon dioxide and Multi-Tran 400 ML for hydrogen, helium and methane at 23°C and 0% RH. A Hysitron TI 950 TriboIndenter^{TM} was used to measure mechanical properties of 10 bilayer PEI/PAA film by a method explained previously.[110] The modulus and the hardness of the sample were measured in two different environments; 38 ^{o}C with 50% relative humidity (RH) and 25 ^{o}C with 22% RH. FTIR spectra of LbL films were measured with a Bruker Optics ALPHA-P 10098-4 spectrometer in ATR mode. PAA peaks in its covalent (COOH) and ionic form (COO^{-}) are of interest in our study to compare the ionic interaction between polycation and polyanion, or so called ‘degree of ionization’.

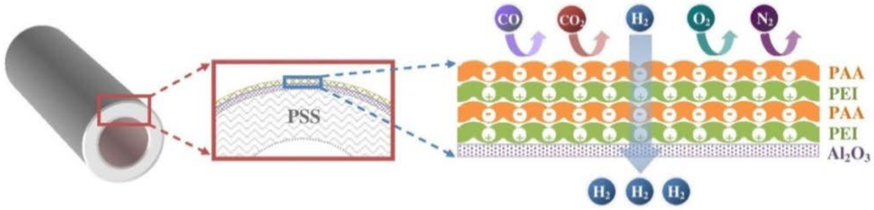

Figure 6.1. Schematic of PEI/PAA layer-by-layer gas separation membrane supported on an alumina-coated porous stainless steel tube.[195]

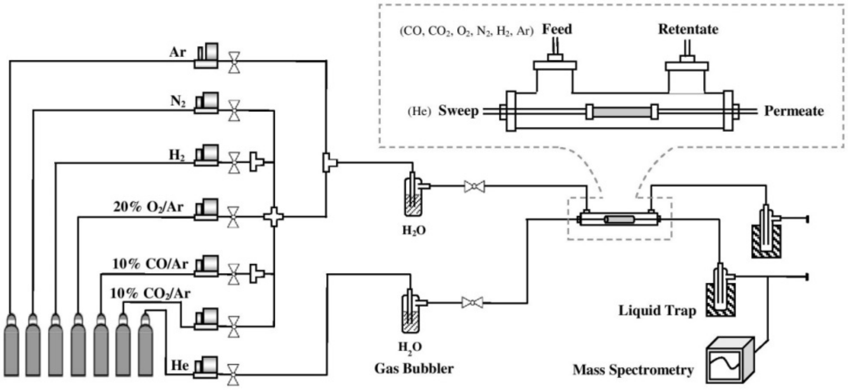

Figure 6.2. Schematic of the tube-and-shell assembly set-up for gas permeation.[195]

6.3 Results and Discussion

6.3.1. Multilayer Film Growth and Structure

Figure 6.3 presents the growth of the film thickness as the number of bilayers of PEI/PAA increases. The film thickness grows exponentially, indicating the ‘scrambled salt’ structure of the film by a highly interpenetrating network.

[redacted]

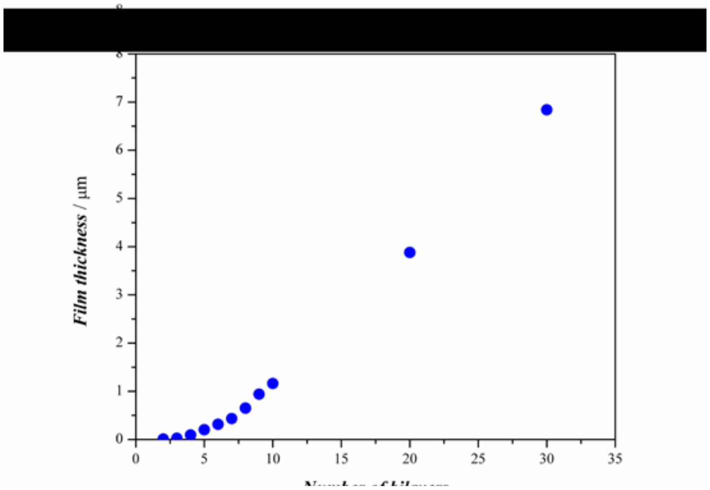

Figure 6.3. The film growth curve of the PEI/PAA films.[195]

Figure 6.4a shows a picture of a complete membrane assembly comprising a 30 bilayer PEI/PAA supported on an alumina coated-PSS substrate. Figure 6.4b presents an optical microscopic image (x50) of the porous surface of the untreated PSS substrate. The optical microscope images of the alumina coated-PSS tube and the PEI/PAA film coated over the alumina-PSS tube are shown in Figure 6.4c and d, respectively. As can be seen in Figure 6.4c, the bright white alumina layer formed by a vacuum assisted-coating technique fills the large cavities and voids present on the surface of the untreated PSS substrate. Comparing optical microscope images of the PEI/PAA film surface (Figure 6.4d) with that of the alumina-coated PSS tube (Figure 6.4c), it indicates that the conformal PEI/PAA coating is free of macroscopic defects. Figure 6.4e shows a cross-sectional SEM image of a 30 bilayer PEI/PAA film deposited over the alumina coated-

PSS tube, confirming the deposition of a ~7 µm polymer membrane over the alumina-coated PSS substrate.

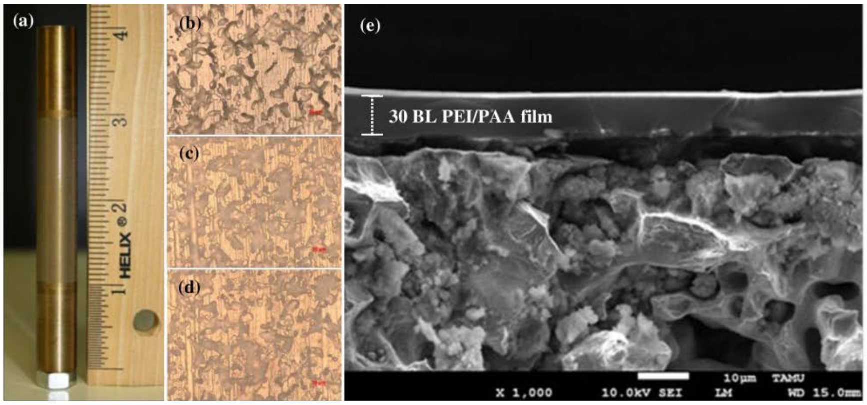

Figure 6.4. Picture of (a) a PEI/PAA-alumina-PSS tube, optical microscopic surface images (x50) of (b) a untreated PSS tube, (c) an alumina layer, (d) a PEI/PAA film, and (e) a SEM cross-section image (x1,000) of a PEI/PAA-alumina-PSS tube.[195]

6.3.2. Gas Separation Behavior

Figure 6.5a shows gas flux of H_2, N_2, O_2, CO, and CO_2 through the alumina-coated PSS tube as a function of partial pressure difference between the feed and sweep sides. Here, H_2 permeance (a slope of the hydrogen flux) is 2.1 x 10^{-7} (mol m^{-2} sec^{-1} Pa^{-1}) and permeance of the other gases (N_2, O_2, CO, CO_2) is about 1.1 x 10^{-7} (mol m^{-2} sec^{-1} Pa^{-1}). After depositing PEI/PAA films over the alumina-coated PSS tube, H_2 permeance through the PEI/PAA films decreased by about two or three order of magnitude compared to that of the alumina coated-PSS tube (Figure 6.5b), with a tendency of reduction in H_2 flux as the number of bilayers increase. In contrast, permeate partial pressures of all other gases studied remained below the lower detection limit of the mass spectrometer [corresponding to a minimum detectable permeability of CO_2 of 8.5×10^{-18} (mol m^{-1} sec^{-1} Pa^{-1})], indicating high H_2 permselectivity of the supported polymer membrane. The same permeation behavior of the PEI/PAA films was observed using a coulometric detector system (Multi-Tran 400, Permatran C4/41, Oxtran 2/21 ML). Again, the obtained permeation rates of O_2, CH_4 and CO_2 through the 10 bilayer PEI/PAA film were below the detection limit, while He and H_2 gases exhibited appreciable permeability. Given the kinetic diameters of the gases studied [He(2.6) < H_2(2.89) < CO_2(3.3) < O_2(3.46) < N_2(3.46) < CO(3.76) < CH_4(3.8)],[300] data confirms that the PEI/PAA LbL films have size-selective pore structure with a limiting diameter between 2.89 Å and 3.3 Å. The lower detection limits for CO_2 and N_2 were employed to estimate minimum detectable H_2-CO_2 and H_2-N_2 permselectivities of 190:1 and 2350:1, respectively. While the extremely low CO_2 and N_2 permeabilities prevented a precise measurement of the intrinsic H_2-N_2 and H_2-CO_2 permselectivities, this minimum detectable permselectivity provides the most conservative basis for comparing the presently reported LbL film against the state-of-the-art in light gas separation polymeric materials.

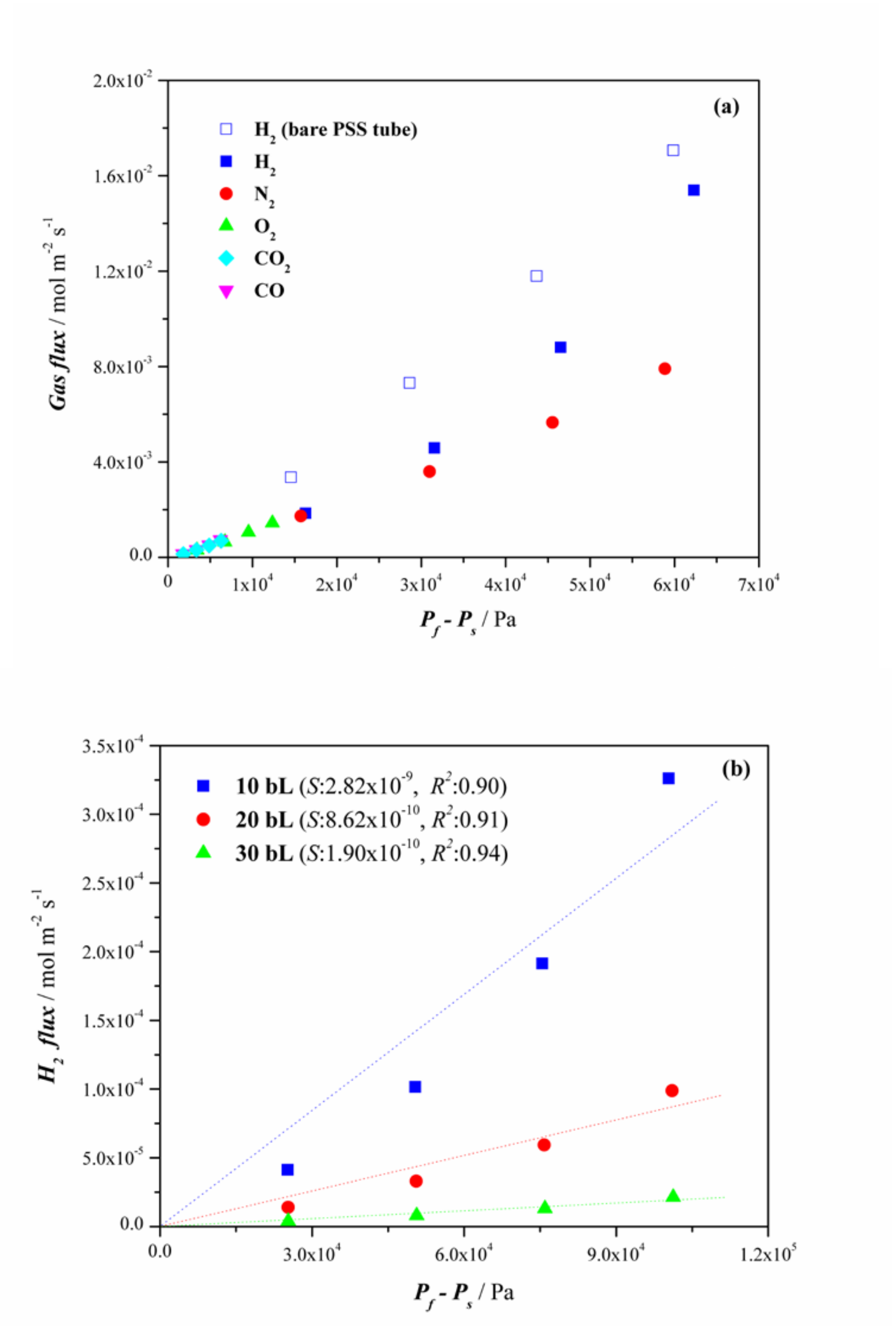

Figure 6.5. (a) Gas permeation through the alumina-coated PSS tube (blank square: bare PSS tube without alumina coating) and (b) H2 flux through PEI/PAA membranes of 10, 20, and 30 bilayers.[195]

Figure 6.6a and b present two lines representing the upper bound limits reported in 1991and 2008 by Robeson[20, 21] for (a) H_2/N_2 and (b) H_2/CO_2. Robeson's upper bound plots were established based on data obtained from various homogeneous polymer films, excluding surface modified, mixed matrix, and carbon molecular sieving membranes. Data points in Figure 6.6 summarize the performance of a broad range of structured membrane materials reported in the literature. It can be seen that several heterogeneous MMMs exceed the upper bound proposed by Robeson, while previously reported LbL films do not. In contrast, the LbL-assembled PEI/PAA films studied in this work exceed the upper boundary by a margin equal to or greater than any existing polymeric gas separation membrane, given the minimum possible H_2:N_2 and H_2:CO_2 permselectivities obtained from the lower detection limit analysis. When compared on the basis of selectivity (α) alone, not even structured porous inorganics can match these relatively simple, polymer-only membranes. Moreover, while existing polymeric membranes have overcome this "upper bound" by introducing heterogeneity and significant structural modification, our previous analysis of the LbL-assembled PEI/PAA film[198] indicates a compact, homogeneous polymer structure. Thus, this report represents the first successful use of a layer-by-layer polymer system to overcome Robeson's "upper bound."

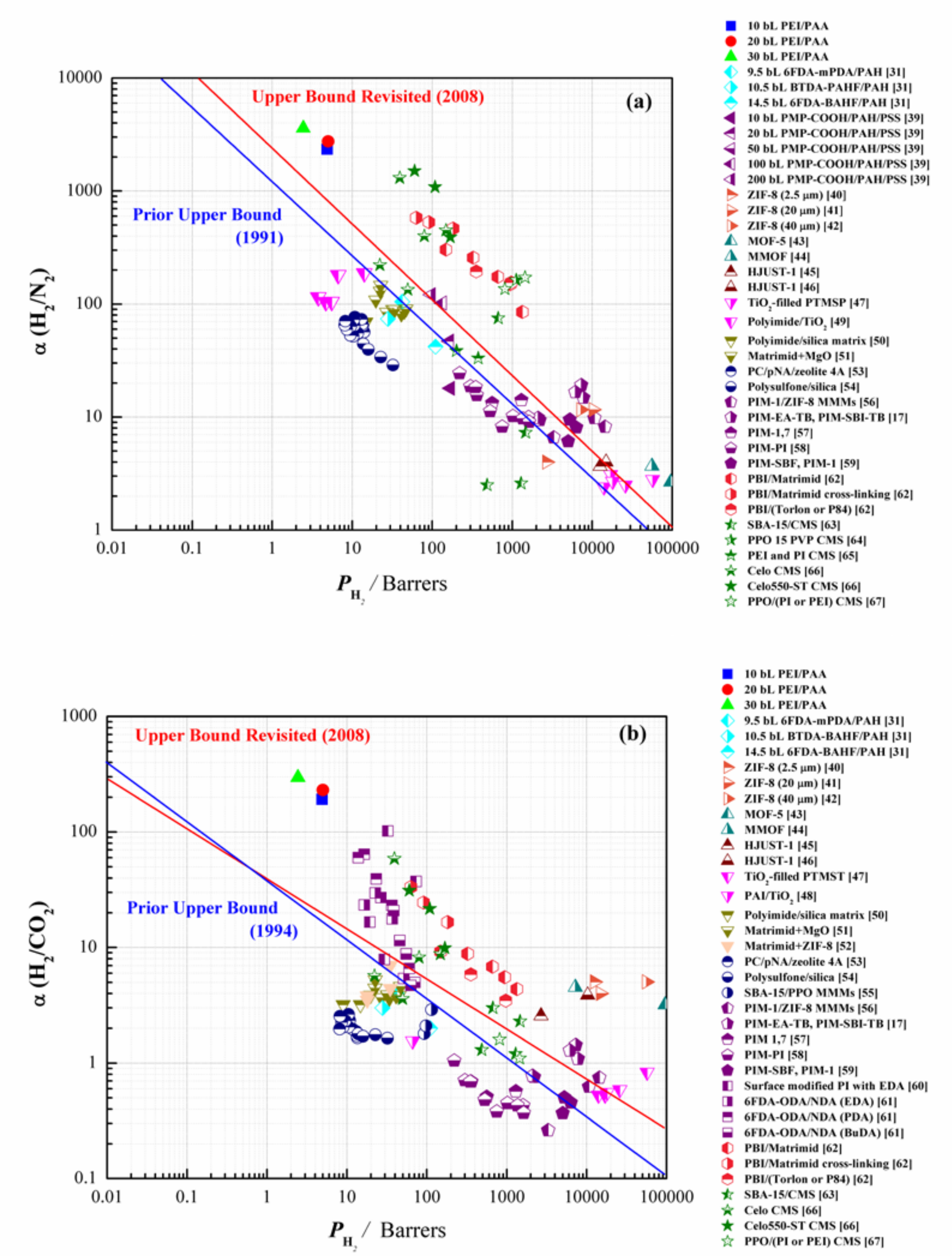

Figure 6.6. Robeson's upper bound plots ((a) H_2/N_2, (b) H_2/CO_2) of 10, 20, and 30 bilayer PEI/PAA polymer films and various other polymer and inorganic (or mixed matrix) membranes (the full term for each abbreviation listed here is presented in the Nomenclature).[195]

6.3.3. Mechanical Strength of Multilayer Film

The compactness of this polymer film can be inferred from its mechanical behavior. Figure 6.7 shows the average elastic modulus and hardness of 10 bilayer PEI/PAA films. This 1µm film has an elastic modulus of 23.4 ± 5.7 GPa and hardness of 0.7 ± 0.3 GPa at 22 %RH, higher than most known all-polymer[318, 319] and even ultrastrong and stiff uncrosslinked polymer/clay LbL assemblies.[52] One reason for this relatively high result can be explained by FTIR (Figure 6.7c). PAA has unique peaks for its neutral (-COOH at 1710 cm^{-1}) and ionized forms ($-COO^-$ at 1560 cm^{-1}) that were investigated to compare the ionic interaction between polycation and polyanion, which can be further quantified as "degree of ionization". In order to derive this value, charged carboxylate and neutral carboxylic acid peaks were first assumed to have similar extinction coefficients,[205] and then the fraction of ionized PAA carboxylic groups was calculated as $Abs_{1560}/(Abs_{1560}+Abs_{1710})$.[206] Based on the spectrum here, the portion of COO^- is much higher than COOH, indicating PAA is highly ionized by PEI. Before the film assembly, both PEI (pH10) and PAA (pH4) aqueous solutions are in neutral form in which the polymer chains are more globular. As deposition proceeds, these pH sensitive polyelectrolytes become highly charged due to the alternating pH (i.e., PEI encountering a lower pH when PAA was deposited and PAA encountering a higher pH environment), resulting in a highly ionic crosslinked and interdiffused assembly. This extensive ionically linked structure might also explain why the assembly maintains a high elastic modulus at 50% RH. Rather than plasticizing, water likely occupies free volume that further densifies the film.[320]

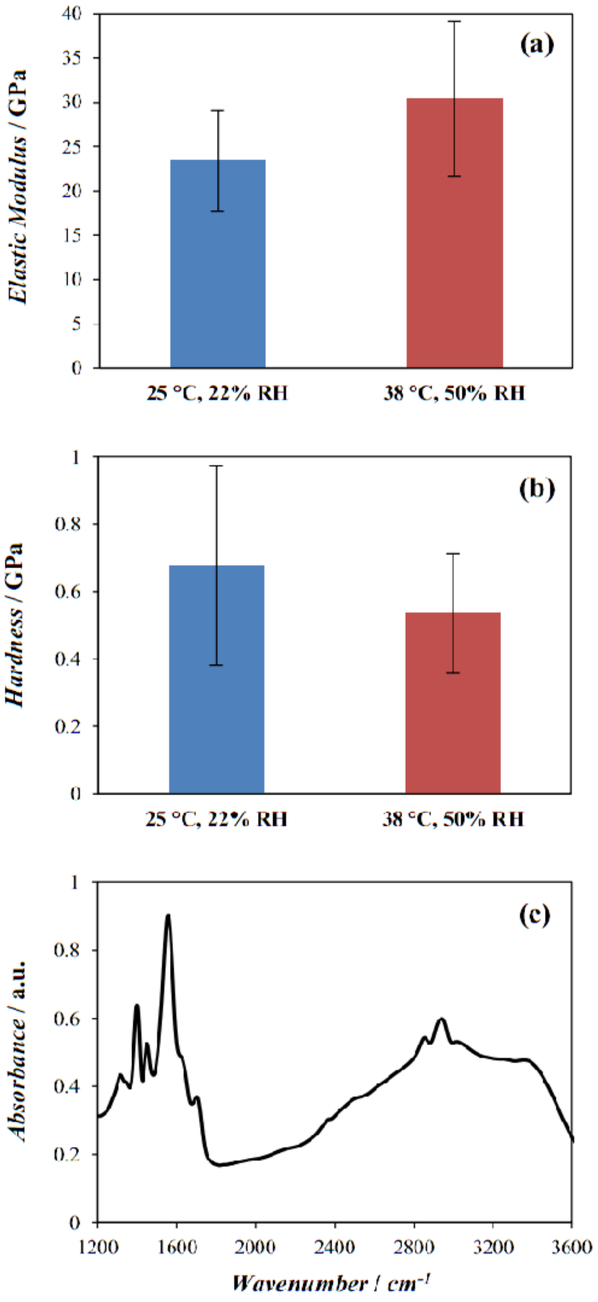

Figure 6.7. (a) Average elastic modulus and (b) hardness of 10 bilayer PEI/PAA films under different environmental conditions (error bars represent standard deviation), and (c) FTIR spectra of 10 bilayer PEI/PAA film.[195]

6.4 Conclusions

This study demonstrates exceptionally high hydrogen permselectivity and remarkable elastic modulus in an ionically crosslinked, layer-by-layer assembled PEI/PAA membrane, which performs beyond Robeson’s upper-bound limit, despite being made of only homogenous polymer. This unique thin film overcomes the drawbacks of common polymeric membranes (i.e., low selectivity and poor mechanical properties), making it a significant advance in polymeric membranes for gas separation.

CHAPTER VII

CONCLUSIONS AND FUTURE WORK

7.1 Multilayer Gas Barrier/Separation Assemblies

The goal of this dissertation work was to improve barrier and separation behavior of permeable polymeric substrates by depositing a thin film assembly. Polymer-polymer and polymer-nanoplatelet layer-by-layer assemblies either reduced gas transmission rate by three orders of magnitude (relative to an uncoated polymer substrate) or exhibited separation performance above the Robeson's upper-bound, with coating thickness ranging from 50 ~ 1500 nm. Furthermore, post-thermal treatment can enhance hydrophobicity of graphene oxide assemblies, thereby improving oxygen barrier at high humidity. This work lays the foundation for the use of LbL assembly as an effective technology for making flexible, transparent gas barrier/separation layers that are important for a variety of packaging and purification applications.

7.1.1 Influence of Polymer Interdiffusion and Clay Concentration on Gas Barrier

Quadlayer assemblies, deposited using the layer-by-layer technique, were used to study how polymer interdiffusion and clay concentration influence the gas barrier behavior. PEI and PVAm were combined with PAA and MMT to generate 'nanobrick walls'. Highly oriented clay platelets, revealed by TEM and AFM, is the reason for the exceptional oxygen barrier exhibited by these films. A 6 QL PVAm-based assembly exhibited an OTR at the detection limit of commercial instrumentation. Rigid PVAm molecules cause quadlayer growth to be linear rather than exponential. This results in thinner layers for PVAm and weaker interaction with PAA relative to PEI. The weak interaction also seems to carry over to MMT, which results in lower clay concentration for PVAm-based assemblies. This study confirms the importance of polymer interdiffusion and clay concentration in reducing oxygen permeability in these nanobrick wall structures. PVAm and PEI were combined to tailor OTR by controlling these factors. It is now possible to simultaneously control OTR and thickness of a multilayer thin film barrier.

7.1.2 Super Hydrogen and Helium Barrier with Polyelectrolyte Nanobrick Wall Thin Film

Quadlayers of PEI/PAA/PEI/MMT were deposited on polystyrene to produce transparent gas barrier assemblies. The impermeable clay platelets, together with highly interdiffused PEI and PAA mortar, formed a nanobrick wall structure that imparts tremendous light gas barrier. Permeability of both hydrogen and helium decreased as the number of quadlayers increased, showing one to three orders of magnitude improvement compared to EVOH and metallized plastics. Increasing the number of QL from 5 to 10 does not improve the barrier properties. This lack of improvement may be due to the dramatically expanded clay spacing and associated concentration reduction. The excellent performance of this assembly, combined with the simplicity of LbL deposition, makes this light gas barrier coating an exciting opportunity for several packaging and storage applications.

7.1.3 Improved Gas Barrier/Separation of Graphene Oxide Based Multilayer Thin Films

Graphene oxide sheets, along with chitosan (CH) and PAA were used in a CH/PAA/CH/GO QL assembly. Charge density (pH) of polyelectrolytes was varied, resulting in different chain conformation and film thickness. Oxygen transmission rate was found to decrease as pH difference between CH and PAA increase, which is connected to the increasing GO deposition (confirmed by SEM). $CH_{5.5}/PAA_3/CH_{5.5}/GO$ exhibited the best barrier performance because CH has been highly ionized by the counter ion, so it was able to attract more GO into the bulk film. Additionally, GO was thermally reduced, which increased hydrophobicity of the film, making OTR less sensitive to moisture. H_2/CO_2 selectivity also increased from 5 to 215 after reduction of GO, showing a performance above the Robeson's upper-bound limit. We believe this composite film, based on its ease of fabrication and excellent barrier/separation behavior, provides plenty of opportunity in packaging and gas separation.

7.1.4 Highly Size-Selective Multilayer Polymer Films for Light Gas Separation

Layer-by-layer multilayer films fabricated with two weak polyelectrolytes, PEI and PAA, exhibited high elastic modulus and hydrogen selectivity. Titrated by the oppositely charged polyelectrolyte (PEI at pH 10 and PAA at pH 4), PEI and PAA become more ionized and require charge overcompensation, resulting in a highly interdiffused network in both directions (from bulk film to solution, and vice versa). High modulus obtained by nanoindentation suggests high density as another evidence of the interdiffused structure. This highly ionically crosslinked film is believed to be denser than traditional polymer films, exhibiting H_2/N_2 and H_2/CO_2 selectivities more than 2350 and 190, respectively (above Robeson's upper-bound limit). This unique thin film overcomes the low selectivity of common polymeric membranes and performs even better than inorganic or mixed-matrix membranes, making it a significant advance in polymeric membranes for gas separation.

7.2 Future Research Plans

Chapters V and VI demonstrate these LbL assemblies exhibit size-selective behavior. Despite their high permeation selectivity, these films are diffusivity dominant, which means they are unable to separate gas molecules with similar sizes (e.g., CO_2 and N_2). New approaches for making solution-selective films are needed for commercial applications. Additionally, the ability of LbL to precisely control assembly conditions (e.g., film thickness and refractive index [RI]) is suitable to create films with enhanced optical effects (e.g., reflecting light of specific wavelengths). Two areas of future research are described here as ways to accomplish these challenges.

7.2.1 Solution-Selective Multilayer Polymer Films for CO_2/N_2 Separation

Poly(ethylene oxide) (PEO) is of considerable interest for separating gases with similar molecular sizes. creating solution-selective membranes. The ether oxygen in PEO has a strong affinity toward CO_2 (quadrupolar interactions), resulting in relatively high solubility and permeability.[321-323] In addition, the process conditions and thermal history play significant roles in the PEO crystallization.[324] Generally, high molecular weight PEO, with high crystallinity, has lower gas permeability and better mechanical properties, whereas low molecular weight PEO, with low crystallinity, has better gas transport properties.[325] Low molecular weight PEO exists in the liquid form and cannot be directly used in gas separation membranes, making the design of PEO-containing membranes with low crystallinity a challenge. Three approaches have been developed to overcome these issues:

1. design of phase-separated block copolymers with short ethylene oxide segments,
2. use of low molecular weight PEO or polyethyleneglycol (PEG) as an additive, and
3. synthesis of highly branched PEO that can be crosslinked. While most approaches require

complex synthesis, LbL provides another route to create a film where both crystallinity and mechanical properties can tailored. In one example, PEO acts as a hydrogen acceptor while poly(methacrylic acid) (PMAA) is used as hydrogen donor to create hydrogen-bonded films. Film thickness varies as pH of PEO and PMAA changes, which is due to the change of chain conformation (Figure 7.1a). A 51 µm PS film coated with 10 BL of $PEO_2/PMAA_2$ showed high CO_2/N_2 selectivity (120) and performed close to Robeson’s upper-bound (Figure 7.1b). Further study on the relation between elastic modulus and permeability is needed.

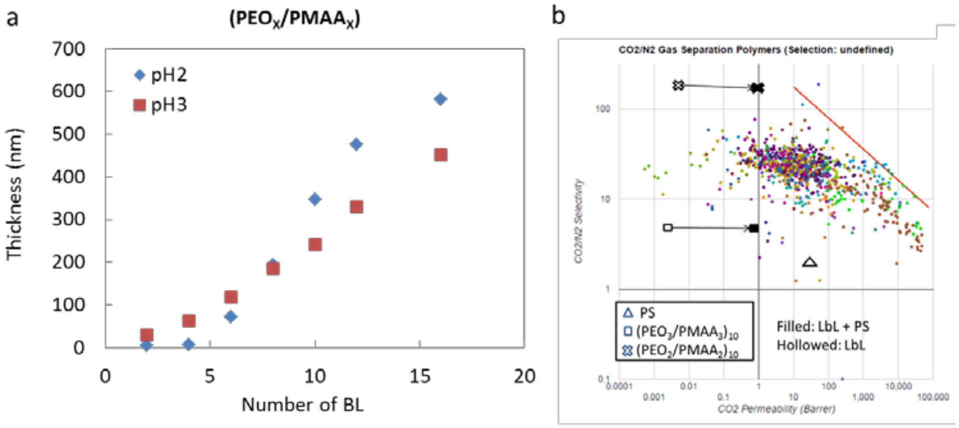

Figure 7.1. (a) PEO$_2$/PMAA$_2$ and PEO$_3$/PMAA$_3$ thickness as a function of number of BL deposited. (b) CO$_2$/N$_2$ separation performance of LbL (hollowed) and LbL-coated PS (filled) on Robeson plot.

7.2.2 Multilayer Structural Color Films

Structurally colored beetles (e.g., *Crysochroa rajah*) possess a periodicity in the upper layer of their cuticles that gives rise to a photonic band gap producing brilliant iridescence.[326] Iridescent color is derived from multilayer photonic structures and in their simplest form consists of layers with alternating high and low refractive indices. Constructive interference of reflected light, or Bragg reflection,[327] is achieved by this system when the thickness of each periodic layer is on the order of λ/4 and the viewing angle is close to 90°. Layer-by-layer deposition is suitable to reproduce this periodicity and create iridescent thin films because film structure is tailorable by adjusting solution concentration, charge density (pH), and deposition time, which produces uniform films with precise thickness. The refractive index (RI) of each layer was designed by combining two materials in each layer, as shown in Figure 7.2a. Thickness of each layer was then controlled by altering the number of BL in each layer (Figure 7.2b and c). The high RI layer (layer A) consisted 13 bilayers of PEI/VMT. The low RI layer (layer B) contained 40 bilayers of cationic colloidal silica (SiO_2) and anionic cellulose nanocrystals (CNCs). Due to the entirely different shape of SiO_2 and CNCs, a porous layer is created. Cross-sectional film structure of the stacks was characterized using SEM and TEM and compared to *C. rajah* beetle. Figure 7.3a is a TEM image showing the periodicity in the cross-section of *C. rajah* beetle elytra. The periodicity is derived from the alternating light and dark layers aligned parallel to the elytra surface. Likewise, cross-sectional TEM images of the assembled films presented alternating light and dark layers as seen in Figure 7.3c and d indicating that RI mismatched had been achieved in layer thicknesses on the order of visible light. Upon closer inspection (Figure 7.3d) a laminar arrangement of VMT (the darker lines) and PEI was seen. Figure 7.3b is a cross-sectional SEM image of $(AB)_{24}A$ which provides information about the B layer structure that the TEM images could not and confirms the dense laminar structure of the A layers. The colloidal silica and the CNCs have formed an isotropic porous structure. Preliminary results, measured by angle resolved spectrophotometry (ARS), are shown in Figure 7.4. This multilayer assembly exhibited iridescent behavior, which means the peak reflection blue shifts as incident angle increases (Figure 7.4a). Similar results were discovered in the cuticles of beetles (Figure 7.4b), suggesting the color in the LbL assembly is the result of periodic high/low RI layers. Further study will focus on varying reflecting wavelength by adjusting layer thickness and RI for applications in sensing, optical filters and replacement of pigment based coatings.

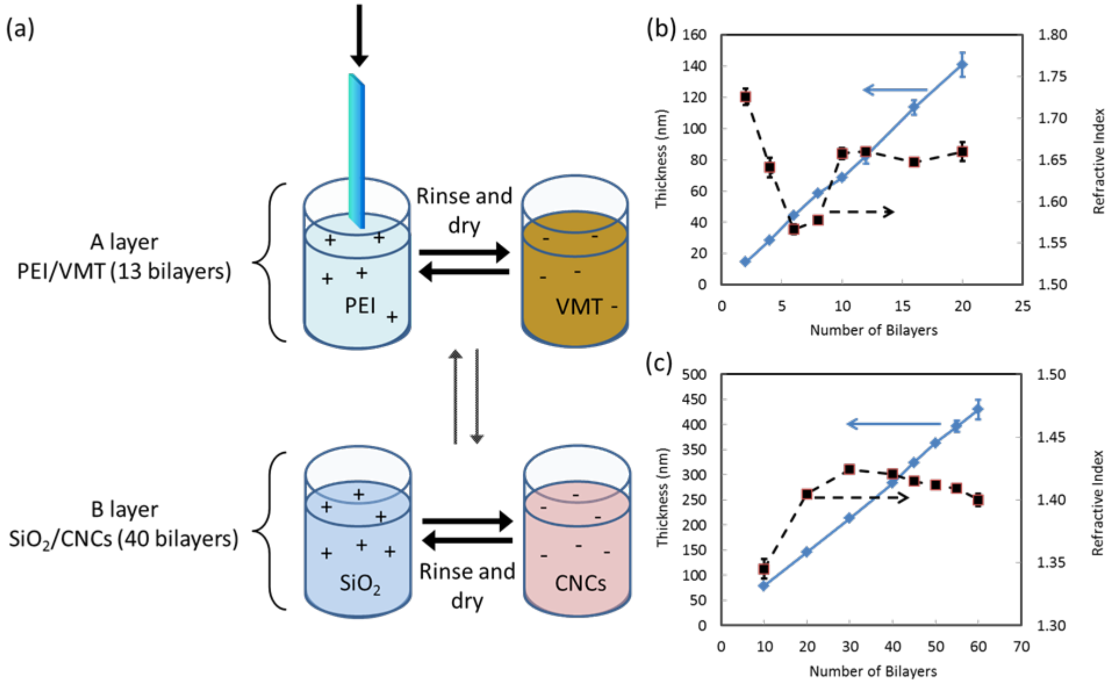

Figure 7.2. (a) Schematic of Bragg stack LbL assembly process. Thickness and refractive index of (b) PEI/VMT and (c) SiO_2/CNCs as a function of bilayers deposited. Error bars are standard deviations from the mean.

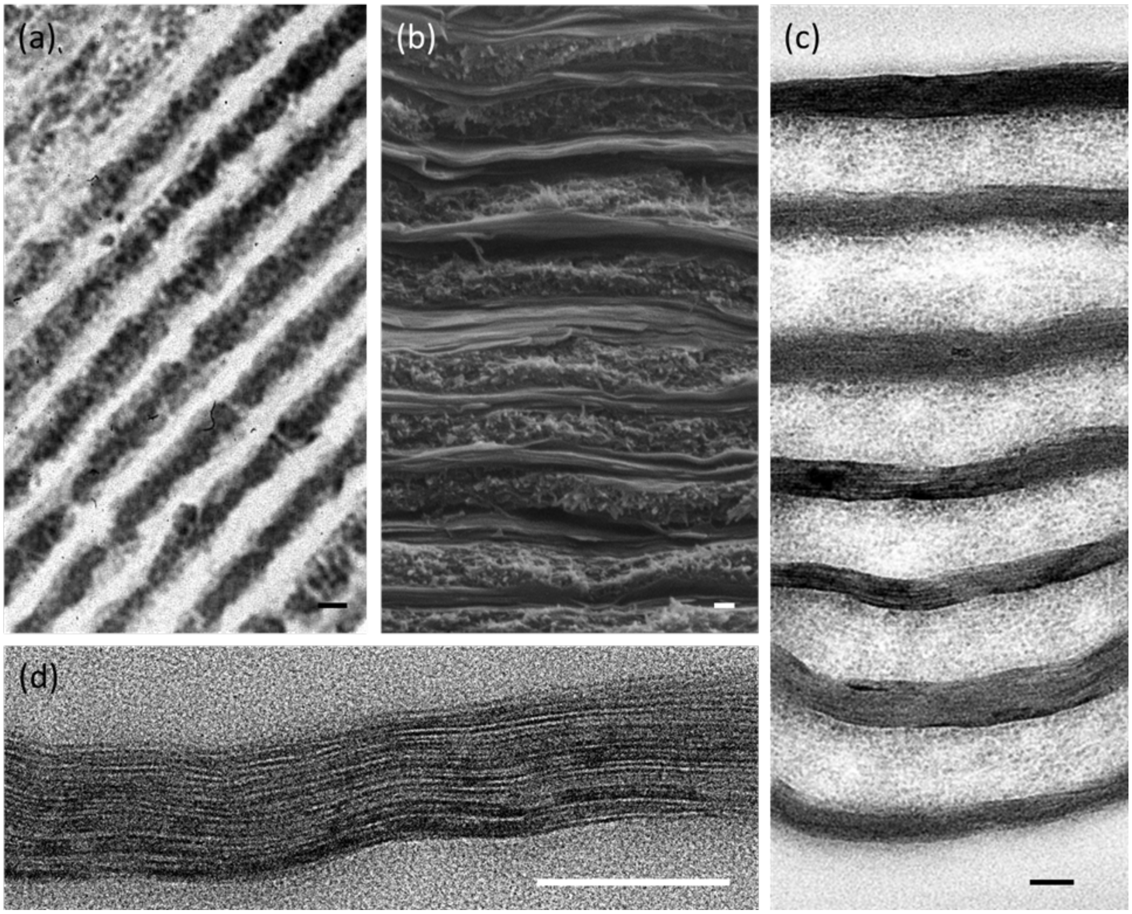

Figure 7.3. (a) TEM cross-section image of the elytra of a *Chrysochroa rajah* beetle. (b) SEM cross-section image of the $(AB)_{24}A$ film. TEM cross-section images of the (c) entire $(AB)_6A$ film and (d) a single A layer. Scale bars in all images represent 100 nm.

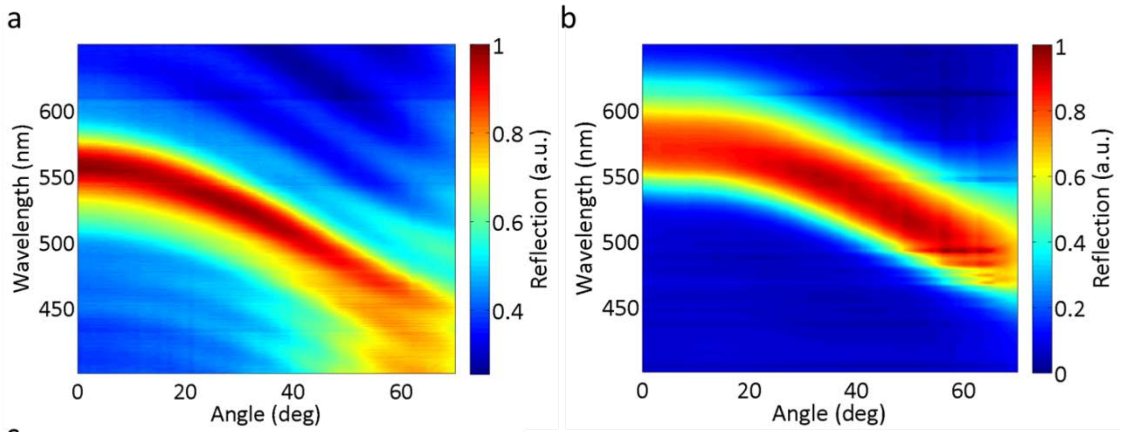

Figure 7.4. Reflection intensity of (a) $(AB)_6A$ film and (b) cuticle of *Crysochroa rajah* as function of wavelength and incident angle.

REFERENCES

[1] L. E. S. Brink, S. J. G. Elbers, T. Robbertsen, P. Both, *Journal of Membrane Science* **1993**, *76*, 281.

[2] H. C. Yang, K. J. Liao, H. Huang, Q. Y. Wu, L. S. Wan, Z. K. Xu, *Journal of Materials Chemistry A* **2014**, *2*, 10225.

[3] H. Valle, J. Sanchez, B. L. Rivas, *Journal of Applied Polymer Science* **2015**, *132*, 41272.

[4] S. J. Lee, A. Chang-Chien, S. W. Cha, R. O'Hayre, Y. I. Park, Y. Saito, F. B. Prinz, *Journal of Power Sources* **2002**, *112*, 410.

[5] J. M. Xu, L. Ma, H. L. Han, H. Z. Ni, Z. Wang, H. X. Zhang, *Electrochimica Acta* **2014**, *146*, 688.

[6] T. Yuan, L. J. Pu, Q. H. Huang, H. F. Zhang, X. M. Li, H. Yang, *Electrochimica Acta* **2014**, *117*, 393.

[7] J. Cho, J. K. Hong, K. Char, F. Caruso, *Journal of the American Chemical Society* **2006**, *128*, 9935.

[8] W. Joo, H. J. Kim, J. K. Kim, *Langmuir* **2010**, *26*, 5110.

[9] F. Trespidi, G. Timo, F. Galeotti, M. Pasini, *Microelectronic Engineering* **2014**, *126*, 13.

[10] G. W. Heffner, D. S. Pearson, *Macromolecules* **1991**, *24*, 6295.

[11] J. J. Jasieniak, J. Seifter, J. Jo, T. Mates, A. J. Heeger, *Advanced Functional Materials* **2012**, *22*, 2594.

[12] K. Kranthiraja, K. Gunasekar, W. Cho, M. Song, Y. G. Park, J. Y. Lee, Y. Shin, I. N. Kang, A. Kim, H. Kim, B. Kim, S. H. Jin, *Macromolecules* **2014**, *47*, 7060.

[13] P. C. Bessa, M. Casal, R. L. Reis, *Journal of Tissue Engineering and Regenerative Medicine* **2008**, *2*, 81.

[14] J. A. M. Steele, S. D. McCullen, A. Callanan, H. Autefage, M. A. Accardi, D. Dini, M. M. Stevens, *Acta Biomaterialia* **2014**, *10*, 2065.

[15] Y. Hu, X. Y. Gu, Y. Yang, J. Huang, M. Hu, W. K. Chen, Z. Tong, C. Y. Wang, *Acs Applied Materials & Interfaces* **2014**, *6*, 17166.

[16] J. Lange, Y. Wyser, *Packaging Technology and Science* **2003**, *16*, 149.

[17] K. K. Mokwena, J. M. Tang, *Critical Reviews in Food Science and Nutrition* **2012**, *52*, 640.

[18] I. Tawakkal, M. J. Cran, J. Miltz, S. W. Bigger, *Journal of Food Science* **2014**, *79*, R1477.

[19] M. R. Anderson, B. R. Mattes, H. Reiss, R. B. Kaner, *Synthetic Metals* **1991**, *41*, 1151.

[20] L. M. Robeson, *Journal of Membrane Science* **1991**, *62*, 165.

[21] L. M. Robeson, *J. Membr. Sci.* **2008**, *320*, 390.

[22] P. Bernardo, E. Drioli, G. Golemme, *Industrial & Engineering Chemistry Research* **2009**, *48*, 4638.

[23] R. W. Baker, *Industrial & Engineering Chemistry Research* **2002**, *41*, 1393.

[24] S. Yoo, C. Holloman, D. Tomasko, K. Koelling, M. A. Pascall, *Packaging Technology and Science* **2014**, *27*, 169.

[25] "Market Statistics and Future Trends in Global Packaging", World Packaging Organisation / PIRA International Ltda, 2008, p. 2012/.

[26] O. G. Piringer, A. L. Baner, "*Plastic packaging materials for food : barrier function, mass transport, quality assurance, and legislation"*, Wiley-VCH, Weinheim; New York, 2000, p. 605.

[27] G. Strupinsky, A. L. Brody, *Polymers, Laminations & Coatings Conference, Books 1 and 2* **1998**, 119.

[28] D. J. Safarik, R. B. Eldridge, *Industrial & Engineering Chemistry Research* **1998**, *37*, 2571.

[29] L. A. Cisternas, C. M. Vasquez, R. E. Swaney, *Aiche Journal* **2006**, *52*, 1754.

[30] A. Bieder, A. Gruniger, P. R. von Rohr, *Surface & Coatings Technology* **2005**, *200*, 928.

[31] S. Duttagupta, F. J. Ma, B. Hoex, A. G. Aberle, *Solar Energy Materials and Solar Cells* **2014**, *120*, 204.

[32] R. Sothornvit, S. I. Hong, D. J. An, J. W. Rhim, *Lwt-Food Science and Technology* **2010**, *43*, 279.

[33] H. Tetsuka, T. Ebina, H. Nanjo, F. Mizukami, *Journal of Materials Chemistry* **2007**, *17*, 3545.

[34] G. Decher, *Science* **1997**, *277*, 1232.

[35] M. Ferreira, M. Rubner, *Macromolecules* **1995**, *28*, 7107.

[36] M. A. Priolo, K. M. Holder, D. Gamboa, J. C. Grunlan, *Langmuir* **2011**, *27*, 12106.

[37] S. S. Shiratori, M. F. Rubner, *Macromolecules* **2000**, *33*, 4213.

[38] H. L. Tan, M. J. McMurdo, G. Pan, P. G. Van Patten, *Langmuir* **2003**, *19*, 9311.

[39] J. Irigoyen, L. Han, I. Llarena, Z. W. Mao, C. Y. Gao, S. E. Moya, *Macromolecular Rapid Communications* **2012**, *33*, 1964.

[40] K. Buscher, K. Graf, H. Ahrens, C. A. Helm, *Langmuir* **2002**, *18*, 3585.

[41] Z. Sui, D. Salloum, J. B. Schlenoff, *Langmuir* **2003**, *19*, 2491.

[42] Y. Shimazaki, R. Nakamura, S. Ito, M. Yamamoto, *Langmuir* **2001**, *17*, 953.

[43] D. A. Hagen, B. Foster, B. Stevens, J. C. Grunlan, *ACS Macro Letters* **2014**, *10*, 663.

[44] P. Bertrand, A. Jonas, A. Laschewsky, R. Legras, *Macromolecular Rapid Communications* **2000**, *21*, 319.

[45] Y. Lvov, K. Ariga, I. Ichinose, T. Kunitake, *Journal of the American Chemical Society* **1995**, *117*, 6117.

[46] W. B. Stockton, M. F. Rubner, *Macromolecules* **1997**, *30*, 2717.

[47] P. Kohli, G. J. Blanchard, *Langmuir* **2000**, *16*, 4655.

[48] K. Ariga, J. P. Hill, Q. Ji, *Physical Chemistry Chemical Physics* **2007**, *9*, 2319.

[49] R. A. Caruso, A. Susha, F. Caruso, *Chemistry of Materials* **2001**, *13*, 400.

[50] P. Kurt, D. Banerjee, R. E. Cohen, M. F. Rubner, *Journal of Materials Chemistry* **2009**, *19*, 8920.

[51] P. Podsiadlo, M. Michel, J. Lee, E. Verploegen, N. W. S. Kam, V. Ball, Y. Qi, A. J. Hart, P. T. Hammond, N. A. Kotov, *Nano Letters* **2008**, *8*, 1762.

[52] P. Podsiadlo, A. K. Kaushik, E. M. Arruda, A. M. Waas, B. S. Shim, J. D. Xu, H. Nandivada, B. G. Pumplin, J. Lahann, A. Ramamoorthy, N. A. Kotov, *Science* **2007**, *318*, 80.

[53] Y. Zou, L. X. Xie, S. Carroll, M. Muniz, H. Gibson, W. Z. Wei, H. P. Liu, G. Z. Mao, *Biomacromolecules* **2014**, *15*, 3965.

[54] M. Alba, P. Formentin, J. Ferre-Borrull, J. Pallares, L. F. Marsal, *Nanoscale Research Letters* **2014**, *9*, 210.

[55] E. C. Dreaden, S. W. Morton, K. E. Shopsowitz, J. H. Choi, Z. J. Deng, N. J. Cho, P. T. Hammond, *Acs Nano* **2014**, *8*, 8374.

[56] X. F. Su, B. S. Kim, S. R. Kim, P. T. Hammond, D. J. Irvine, *Acs Nano* **2009**, *3*, 3719.

[57] P. Podsiadlo, L. Sui, Y. Elkasabi, P. Burgardt, J. Lee, A. Miryala, W. Kusumaatmaja, M. R. Carman, M. Shtein, J. Kieffer, J. Lahann, N. A. Kotov, *Langmuir* **2007**, *23*, 7901.

[58] K. Manabe, S. Nishizawa, K. H. Kyung, S. Shiratori, *Acs Applied Materials & Interfaces* **2014**, *6*, 13985.

[59] Z. Wu, D. Lee, M. Rubner, R. Cohen, *Small* **2007**, *3*, 1467.

[60] Y. C. Li, S. Mannen, A. B. Morgan, S. Chang, Y. H. Yang, B. Condon, J. C. Grunlan, *Advanced Materials* **2011**, *23*, 3926.

[61] D. Patra, P. Vangal, A. A. Cain, C. Cho, O. Regev, J. C. Grunlan, *Acs Applied Materials & Interfaces* **2014**, *6*, 16903.

[62] Y. S. Kim, Y. C. Li, W. M. Pitts, M. Werrel, R. D. Davis, *Acs Applied Materials & Interfaces* **2014**, *6*, 2146.

[63] Y.-H. Yang, M. Haile, Y. T. Park, F. A. Malek, J. C. Grunlan, *Macromolecules* **2011**, *44*, 1450.

[64] T. Guin, M. Krecker, D. A. Hagen, J. C. Grunlan, *Langmuir* **2014**, *30*, 7057.

[65] Y. H. Yang, L. Bolling, M. A. Priolo, J. C. Grunlan, *Advanced Materials* **2013**, *25*, 503.

[66] M. A. Priolo, D. Gamboa, K. M. Holder, J. C. Grunlan, *Nano letters* **2010**, *10*, 4970.

[67] J. K. Mitchell, *Am. J. Med.* **1830**, *13*, 36.

[68] J. K. Mitchell, *Am. J. Med. Sci.* **1833**, *25*, 100.

[69] T. Graham, *Philos. Mag.* **1866**, *32*, 401.

[70] R. W. Baker, *Membrane Technology and Applications*, **2004**, *10*, 325.

[71] M. Knudsen, "*The kinetic theory of gases; some modern aspects"*, Methuen & co. ltd., London,, 1934, p. 7.

[72] A. Yamasaki, H. Inoue, *J Membrane Sci* **1991**, *59*, 233.

[73] N. N. Li, A. G. Fane, W. S. W. Ho, T. Matsuura, "*Advanced Membrane Technology and Applications"*, Wiley-VCH, Weinheim; New York, 2011, p. 65.

[74] H. Fujita, A. Kishimoto, K. Matsumoto, *T Faraday Soc* **1960**, *56*, 424.

[75] W. J. Koros, Polymer Chemistry Inc., "*Barrier polymers and structures"*, American Chemical Society, Washington, DC, 1990, p. 10.

[76] F. Gruen, *Experimenta* **1947**, *3*, 490.

[77] G. J. van Amerongen, *J. Appl. Phys.* **1946**, *17*, 972.

[78] R. D. Behling, Ohlrogge, K., Peinemann, K. V., Kyburz, E., "*The separation of hydrocarbons from waste vapor streams"*, AICHE, New York, 1989.

[79] R. M. Barrer, J. A. Barrie, J. Slater, *J Polym Sci* **1958**, *27,* 177.

[80] J. H. Petropoulos, *Journal of Polymer Science Part A-2: Polymer Physics* **1970**, *8*, 1797.

[81] W. J. Koros, D. R. Paul, A. A. Rocha, *Journal of Polymer Science Part B-Polymer Physics* **1976**, *14*, 687.

[82] S. S. Ray, M. Okamoto, *Progress in Polymer Science* **2003**, *28,* 1539.

[83] E. P. Giannelis, *Advanced Materials* **1996**, *8,* 29.

[84] L. A. Almeida, M. D. V. Marques, K. Dahmouche, *Journal of Nanoscience and Nanotechnology* **2015**, *15*, 2514.

[85] G. Choudalakis, A. D. Gotsis, *European Polymer Journal* **2009**, *45,* 967.

[86] T. Kashiwagi, R. H. Harris, X. Zhang, R. M. Briber, B. H. Cipriano, S. R. Raghavan, W. H. Awad, J. R. Shields, *Polymer* **2004**, *45*, 881.

[87] M. Sain, S. H. Park, F. Suhara, S. Law, *Polymer Degradation and Stability* **2004**, *83*, 363.

[88] B. Wang, K. Q. Zhou, S. H. Jiang, Y. Q. Shi, B. B. Wang, Z. Gui, Y. Hu, *Materials Research Bulletin* **2014**, *56*, 107.

[89] E. Picard, A. Vermogen, J. F. Gerard, E. Espuche, *Journal of Membrane Science* **2007**, *292*, 133.

[90] G. H. Fredrickson, J. Bicerano, *Journal of Chemical Physics* **1999**, *110*, 2181.

[91] S. Nazarenko, P. Meneghetti, P. Julmon, B. G. Olson, S. Qutubuddin, *Journal of Polymer Science Part B-Polymer Physics* **2007**, *45*, 1733.

[92] E. P. Giannelis, R. Krishnamoorti, E. Manias, *Adv Polym Sci* **1999**, *138*, 107.

[93] H. J. Ploehn, C. Y. Liu, *Industrial & Engineering Chemistry Research* **2006**, *45*, 7025.

[94] P. Dubois, M. Alexandre, *Materials Science & Engineering R-Reports* **2000**, *28*, 1.

[95] V. Mittal, *Materials* **2009**, *2*, 992.

[96] T. Lan, P. D. Kaviratna, T. J. Pinnavaia, *Chem Mater* **1995**, *7*, 2144.

[97] M. Biswas, S. S. Ray, *New Polymerization Techniques and Synthetic Methodologies* **2001**, *155*, 167.

[98] S. Takahashi, H. A. Goldberg, C. A. Feeney, D. P. Karim, M. Farrell, K. O'Leary, D. R. Paul, *Polymer* **2006**, *47*, 3083.

[99] L. E. Nielsen, *J. Macromol. Sci. (Chem).* **1967**, *A1*, 929.

[100] E. L. Cussler, S. E. Hughes, W. J. Ward, R. Aris, *Journal of Membrane Science* **1988**, *38*, 161.

[101] J. P. DeRocher, B. T. Gettelfinger, J. S. Wang, E. E. Nuxoll, E. L. Cussler, *Journal of Membrane Science* **2005**, *254*, 21.

[102] Y. Maeda, D. R. Paul, *Journal of Membrane Science* **1987**, *30*, 1.

[103] T. A. Barbari, W. J. Koros, D. R. Paul, *Journal of Membrane Science* **1989**, *42*, 69.

[104] S. A. Stern, Y. Mi, H. Yamamoto, A. K. Stclair, *Journal of Polymer Science Part B-Polymer Physics* **1989**, *27*, 1887.

[105] T. H. Kim, W. J. Koros, G. R. Husk, K. C. Obrien, *Journal of Membrane Science* **1988**, *37*, 45.

[106] T. Krug, Ludwig, R., Steiniger, G., "New developments in transparent barrier coatings", Society of Vacuum Coaters - 36th Annual Technical Conference Proceedings, 1993302.

[107] R. K. Bharadwaj, *Macromolecules* **2001**, *34*, 9189.

[108] S. S. Ray, K. Yamada, M. Okamoto, A. Ogami, K. Ueda, *Chemistry of Materials* **2003**, *15*, 1456.

[109] C. F. Yang, E. L. Cussler, *Journal of Membrane Science* **2004**, *231*, 1.

[110] M. A. Priolo, D. Gamboa, J. C. Grunlan, *Acs Applied Materials & Interfaces* **2010**, *2*, 312.

[111] W. J. Koros, G. K. Fleming, *Journal of Membrane Science* **1993**, *83*, 1.

[112] L. R. Xu, C. Zhang, M. Rungta, W. L. Qiu, J. Q. Liu, W. J. Koros, *Journal of Membrane Science* **2014**, *459*, 223.

[113] H. Lin, B. D. Freeman, *Journal of Membrane Science* **2004**, *239*, 105.

[114] M. Yan, T. W. Kim, A. G. Erlat, M. Pellow, D. F. Foust, H. Liu, M. Schaepkens, C. M. Heller, P. A. McConnelee, T. P. Feist, A. R. Duggal, *Proceedings of the Ieee* **2005**, *93*, 1468.

[115] J. R. Wagner, "*Multilayer Flexible Packaging: Technology and Applications for the Food, Personal Care, and Over-the-Counter Pharmaceutical Industries"*, Elsevier Science, Boston, 2009.

[116] Y. Leterrier, *Progress in Materials Science* **2003**, *48*, 1.

[117] C. Caner, R. J. Hernandez, B. R. Harte, *Packaging Technology and Science* **2004**, *17*, 23.

[118] J. M. S. Henis, M. K. Tripodi, *Separation Science and Technology* **1980**, *15*, 1059.

[119] D. L. Maclean, W. A. Bollinger, D. E. King, R. S. Narayan, *Abstracts of Papers of the American Chemical Society* **1981**, *182*, 118.

[120] V. Mittal, "*Barrier properties of polymer clay nanocomposite"*, Nova Science, New York, 2009, p. 271.

[121] S. M. Jickells, J. Poulin, K. A. Mountfort, M. Fernandez-Ocana, *Food Additives and Contaminants* **2005**, *22*, 768.

[122] M. Bientinesi, L. Petarca, *Chemical and Process Engineering*, **2011**, *10*, 763.

[123] A. Iulianelli, A. Basile, *Catalysis Science & Technology* **2011**, *1*, 366.

[124] M. Walther, M. Heming, M. Spallek, *Surf Coat Tech* **1996**, *80*, 200.

[125] C. F. Struller, P. J. Kelly, N. J. Copeland, V. Tobin, H. E. Assender, C. W. Holliday, S. J. Read, *Thin Solid Films* **2014**, *553*, 153.

[126] A. Morlier, S. Cros, J. P. Garandet, N. Alberola, *Thin Solid Films* **2014**, *550*, 85.

[127] S. I. Hong, J. H. Lee, H. J. Bae, S. Y. Koo, H. S. Lee, J. H. Choi, D. H. Kim, S. H. Park, H. J. Park, *Journal of Applied Polymer Science* **2011**, *119*, 2742.

[128] N. Yan, G. Buonocore, M. Lavorgna, S. Kaciulis, S. K. Balijepalli, Y. H. Zhan, H. S. Xia, L. Ambrosio, *Composites Science and Technology* **2014**, *102*, 74.

[129] J. T. Yeh, S. S. Huang, W. H. Yao, I. J. Wang, C. C. Chen, *J Appl Polym Sci* **2004**, *92*, 2528.

[130] J. B. Faisant, A. Ait-Kadi, M. Bousmina, L. Deschenes, *Polymer* **1998**, *39*, 533.

[131] L. Da Silva, R. E. S. Bretas, *Polym Eng Sci* **2000**, *40*, 1414.

[132] B. S. Minhas, T. Matsuura, S. Sourirajan, *Acs Symposium Series* **1985**, *281*, 451.

[133] B. S. Minhas, T. Matsuura, S. Sourirajan, *Industrial & Engineering Chemistry Research* **1987**, *26*, 2344.

[134] K. Mizoguchi, K. Terada, Y. Naito, Y. Kamiya, S. Tsuchida, S. Yano, *Colloid Polym. Sci.* **1997**, *275*, 86.

[135] S. H. Chen, M. H. Lee, J. Y. Lai, *European Polymer Journal* **1996**, *32*, 1403.

[136] D. R. Pesiri, B. Jorgensen, R. C. Dye, *Journal of Membrane Science* **2003**, *218*, 11.

[137] D. E. Sanders, Z. P. Smith, R. L. Guo, L. M. Robeson, J. E. McGrath, D. R. Paul, B. D. Freeman, *Polymer* **2013**, *54*, 4729.

[138] C. A. Scholes, C. P. Ribeiro, S. E. Kentish, B. D. Freeman, *Separation and Purification Technology* **2014**, *124*, 134.

[139] C. A. Scholes, C. P. Ribeiro, S. E. Kentish, B. D. Freeman, *Journal of Membrane Science* **2014**, *450*, 72.

[140] E. Finson, J. Felts, *Tappi Journal* **1995**, *78*, 161.

[141] G. Alefeld, J. Völkl, "*Hydrogen in Metals: Basic properties*", Springer-Verlag, New York, 1978.

[142] J. Philpott, *Platinum Metals Rev* **1985**, *29*, 12.

[143] J. T. Felts, A. D. Grubb, *Journal of Vacuum Science & Technology a-Vacuum Surfaces and Films* **1992**, *10*, 1675.

[144] C. Misiano, Simonetti, E., Cerolini, P., Staffetti, F., "Silicon oxide barrier improvement on plastic substrate", Society of Vacuum Coaters - 34rd Annual Technical Conference Proceedings, 2009, 1991105.

[145] L. Agres, Y. Segui, R. Delsol, P. Raynaud, *Journal of Applied Polymer Science* **1996**, *61*, 2015.

[146] T. Krug, "Transparent barriers for food packaging", Society of Vacuum Coaters - 33rd Annual Technical Conference Proceedings, 2008, 1990163.

[147] H. Chatham, *Surface & Coatings Technology* **1996**, *78*, 1.

[148] A. S. D. Sobrinho, G. Czeremuszkin, M. Latreche, G. Dennler, M. R. Wertheimer, *Surface & Coatings Technology* **1999**, *116*, 1204.

[149] J. Caro, M. Noack, P. Kolsch, R. Schafer, *Microporous and Mesoporous Materials* **2000**, *38*, 3.

[150] C. J. Brinker, C. Y. Tsai, Y. Lu, "Inorganic dual-layer microporous supported membranes", US Patent 6536604 B1, 2003.

[151] T. S. Chung, L. Y. Jiang, Y. Li, S. Kulprathipanja, *Progress in Polymer Science* **2007**, *32*, 483.

[152] T. H. Bae, J. S. Lee, W. L. Qiu, W. J. Koros, C. W. Jones, S. Nair, *Angewandte Chemie-International Edition* **2010**, *49*, 9863.

[153] J. N. Gavgani, H. Adelnia, M. M. Gudarzi, *Journal of Materials Science* **2014**, *49*, 243.

[154] F. Carosio, S. Colonna, A. Fina, G. Rydzek, J. Hemmerle, L. Jierry, P. Schaaf, F. Boulmedais, *Chemistry of Materials* **2014**, *26*, 5459.

[155] M. A. Osman, V. Mittal, M. Morbidelli, U. W. Suter, *Macromolecules* **2003**, *36*, 9851.

[156] J. K. Kim, C. G. Hu, R. S. C. Woo, M. L. Sham, *Compos Sci Technol* **2005**, *65*, 805.

[157] M. A. Osman, V. Mittal, U. W. Suter, *Macromol Chem Physic* **2007**, *208*, 68.

[158] S. S. Ray, K. Yamada, M. Okamoto, K. Ueda, *Nano Lett* **2002**, *2,* 1093.

[159] W. S. Jang, I. Rawson, J. C. Grunlan, *Thin Solid Films* **2008**, *516*, 4819.

[160] Z. Bartczak, A. Rozanski, J. Richert, *European Polymer Journal* **2014**, *61*, 274.

[161] B. Zeeb, C. Thongkaew, J. Weiss, *Journal of Applied Polymer Science* **2014**, *131,* 11.

[162] L. L. del Mercato, M. M. Ferraro, F. Baldassarre, S. Mancarella, V. Greco, R. Rinaldi, S. Leporatti, *Advances in Colloid and Interface Science* **2014**, *207,* 139.

[163] M. N. Antipina, M. V. Kiryukhin, A. G. Skirtach, G. B. Sukhorukov, *International Materials Reviews* **2014**, *59*, 224.

[164] J. Borges, L. C. Rodrigues, R. L. Reis, J. F. Mano, *Advanced Functional Materials* **2014**, *24*, 5624.

[165] F. Embs, D. Funhoff, A. Laschewsky, U. Licht, H. Ohst, W. Prass, H. Ringsdorf, G. Wegner, R. Wehrmann, *Advanced Materials* **1991**, *3*, 25.

[166] H. Fuchs, H. Ohst, W. Prass, *Advanced Materials* **1991**, *3*, 10.

[167] L. Q. Li, M. H. Kopf, S. V. Gurevich, R. Friedrich, L. F. Chi, *Small* **2012**, *8,* 488.

[168] R. K. Iler, *Journal of Colloid and Interface Science* **1966**, *21*, 569.

[169] R. K. Iler, *Journal of Colloid and Interface Science* **1971**, *37,* 364.

[170] R. K. Iler, *Journal of Colloid and Interface Science* **1973**, *43*, 399.

[171] G. Decher, J. D. Hong, *Makromolekulare Chemie-Macromolecular Symposia* **1991**, *46*, 321.

[172] G. Decher, J. D. Hong, J. Schmitt, *Thin Solid Films* **1992**, *210*, 831.

[173] S. A. Sukhishvili, S. Granick, *J Am Chem Soc* **2000**, *122*, 9550.

[174] F. M. Xiang, S. M. Ward, T. M. Givens, J. C. Grunlan, *Acs Macro Letters* **2014**, *3*, 1055.

[175] J. H. Dai, D. M. Sullivan, M. L. Bruening, *Industrial & Engineering Chemistry Research* **2000**, *39*, 3528.

[176] S. Moya, L. Dahne, A. Voigt, S. Leporatti, E. Donath, H. Mohwald, *Colloids and Surfaces a-Physicochemical and Engineering Aspects* **2001**, *183*, 27.

[177] D. E. Bergbreiter, K. S. Liao, *Soft Matter* **2009**, *5*, 23.

[178] K. M. Holder, B. R. Spears, M. E. Huff, M. A. Priolo, E. Harth, J. C. Grunlan, *Macromolecular Rapid Communications* **2014**, *35*, 960.

[179] P. T. Hammond, *Aiche Journal* **2011**, *57*, 2928.

[180] A. J. Svagan, A. Akesson, M. Cardenas, S. Bulut, J. C. Knudsen, J. Risbo, D. Plackett, *Biomacromolecules* **2012**, *13*, 397.

[181] M. A. Priolo, K. M. Holder, S. M. Greenlee, B. E. Stevens, J. C. Grunlan, *Chemistry of Materials* **2013**, *25*, 1649.

[182] M. A. Priolo, K. M. Holder, S. M. Greenlee, J. C. Grunlan, *Acs Applied Materials & Interfaces* **2012**, *4*, 5529.

[183] B. Stevens, E. Dessiatova, D. A. Hagen, A. D. Todd, C. W. Bielawski, J. C. Grunlan, *Acs Applied Materials & Interfaces* **2014**, *6*, 9942.

[184] P. Tzeng, C. R. Maupin, J. C. Grunlan, *Journal of Membrane Science* **2014**, *452,* 46.

[185] K. Tao, C. L. Kong, L. Chen, *Chemical Engineering Journal* **2013**, *220*, 1.

[186] J. S. McHattie, W. J. Koros, D. R. Paul, *Polymer* **1991**, *32*, 840.

[187] S. Basu, A. L. Khan, A. Cano-Odena, C. Q. Liu, I. F. J. Vankelecom, *Chemical Society Reviews* **2010**, *39*, 750.

[188] J. H. Zhou, X. Zhu, J. Hu, H. L. Liu, Y. Hu, J. W. Jiang, *Physical Chemistry Chemical Physics* **2014**, *16*, 6075.

[189] N. Joseph, P. Ahmadiannamini, R. Hoogenboom, I. F. J. Vankelecom, *Polymer Chemistry* **2014**, *5*, 1817.

[190] P. Stroeve, V. Vasquez, M. A. N. Coelho, J. F. Rabolt, *Thin Solid Films* **1996**, *284,* 708.

[191] J. M. Levasalmi, T. J. McCarthy, *Macromolecules* **1997**, *30*, 1752.

[192] D. M. Sullivan, M. L. Bruening, *Chemistry of Materials* **2003**, *15*, 281.

[193] A. S. Huang, Q. Liu, N. Y. Wang, Y. Q. Zhu, J. Caro, *Journal of the American Chemical Society* **2014**, *136*, 14686.

[194] J. Choi, M. Tsapatsis, *Journal of the American Chemical Society* **2010**, *132,* 448.

[195] D. Kim, P. Tzeng, K. J. Barnett, Y. H. Yang, B. A. Wilhite, J. C. Grunlan, *Advanced Materials* **2014**, *26*, 746.

[196] T. Ebina, F. Mizukami, *Advanced Materials* **2007**, *19*, 2450.

[197] M. A. Priolo, D. Gamboa, K. M. Holder, J. C. Grunlan, *Nano Letters* **2010**, *10*, 4970.

[198] Y. H. Yang, M. Haile, Y. T. Park, F. A. Malek, J. C. Grunlan, *Macromolecules* **2011**, *44*, 1450.

[199] S. L. Clark, P. T. Hammond, *Langmuir* **2000**, *16*, 10206.

[200] N. S. Zacharia, M. Modestino, P. T. Hammond, *Macromolecules* **2007**, *40*, 9523.

[201] H. J. Ploehn, C. Liu, *Industrial & Engineering Chemistry Research* **2006**, *45*, 7025.

[202] E. M. Liston, L. Martinu, M. R. Wertheimer, *Journal of Adhesion Science and Technology* **1993**, *7*, 1091.

[203] W. S. Jang, J. C. Grunlan, *Review of Scientific Instruments* **2005**, *76*.

[204] D. Gamboa, M. A. Priolo, A. Ham, J. C. Grunlan, *Review of Scientific Instruments* **2010**, *1*, 81.

[205] A. F. Xie, S. Granick, *Macromolecules* **2002**, *35*, 1805.

[206] J. Choi, M. F. Rubner, *Macromolecules* **2005**, *38*, 116.

[207] ASTM Standard D3985, Standard Test Method for Oxygen Gas Transmission Rate Through Plastic Film and Sheeting Using a Coulometric Sensor. ASTM International, West Conshohocken, PA, **2005**, DOI: 10.1520/D3985.

[208] G. Ladam, P. Schaad, P. Schaaf, G. Decher, J. C. Voegel, F. Cuisinier, *Langmuir* **2000**, *16*, 1249.

[209] C. Porcel, P. Lavalle, G. Decher, B. Senger, J. C. Voegel, P. Schaaf, *Langmuir* **2007**, *23*, 1898.

[210] E. Kharlampieva, S. A. Sukhishvili, *Langmuir* **2003**, *19*, 1235.

[211] C. J. Bloysvantreslong, *Recueil Des Travaux Chimiques Des Pays-Bas-Journal of the Royal Netherlands Chemical Society* **1978**, *97*, 13.

[212] E. J. Shepherd, J. A. Kitchener, *Journal of the Chemical Society* **1956**, 2448.

[213] S. Choosakoonkriang, B. A. Lobo, G. S. Koe, J. G. Koe, C. R. Middaugh, *Journal of Pharmaceutical Sciences* **2003**, *92*, 1710.

[214] O. E. Philippova, D. Hourdet, R. Audebert, A. R. Khokhlov, *Macromolecules* **1997**, *30*, 8278.

[215] A. I. Petrov, A. A. Antipov, G. B. Sukhorukov, *Macromolecules* **2003**, *36*, 10079.

[216] J. L. Lutkenhaus, K. McEnnis, P. T. Hammond, *Macromolecules* **2008**, *41*, 6047.

[217] X. Y. Lu, B. Z. Jiang, *Polymer* **1991**, *32*, 471.

[218] J. H. Lee, T. G. Park, H. S. Park, D. S. Lee, Y. K. Lee, S. C. Yoon, J. D. Nam, *Biomaterials* **2003**, *24*, 2773.

[219] L. Kolarik, D. N. Furlong, H. Joy, C. Struijk, R. Rowe, *Langmuir* **1999**, *15*, 8265.

[220] B. Schoeler, E. Poptoschev, F. Caruso, *Macromolecules* **2003**, *36*, 5258.

[221] J. Y. Lee, P. C. Painter, M. M. Coleman, *Macromolecules* **1988**, *21*, 954.

[222] X. Y. Lu, R. A. Weiss, *Macromolecules* **1995**, *28*, 3022.

[223] D. K. Kim, S. W. Han, C. H. Kim, J. D. Hong, K. Kim, *Thin Solid Films* **1999**, *350*, 153.

[224] R. M. Silverstein, G. C. Bassler, *Journal of Chemical Education* **1962**, *39*, 546.

[225] A. Walther, I. Bjurhager, J. M. Malho, J. Pere, J. Ruokolainen, L. A. Berglund, O. Ikkala, *Nano Letters* **2010**, *10*, 2742.

[226] J. C. Grunlan, A. Grigorian, C. B. Hamilton, A. R. Mehrabi, *Journal of Applied Polymer Science* **2004**, *93,* 1102.

[227] E. Cussler, S. E. Hughes, W. J. Ward III, R. Aris, *Journal of Membrane Science* **1988**, *38*, 161.

[228] K. S. Triantafyllidis, P. C. LeBaron, I. Park, T. J. Pinnavaia, *Chemistry of Materials* **2006**, *18*, 4393.

[229] A. Laachachi, V. Ball, K. Apaydin, V. Toniazzo, D. Ruch, *Langmuir* **2011**, *27*, 13879.

[230] A. P. Roberts, B. M. Henry, A. P. Sutton, C. R. M. Grovenor, G. A. D. Briggs, T. Miyamoto, A. Kano, Y. Tsukahara, M. Yanaka, *Journal of Membrane Science* **2002**, *208*, 75.

[231] N. Inagaki, S. Tasaka, H. Hiramatsu, *Journal of Applied Polymer Science* **1999**, *71*, 2091.

[232] M. Yanaka, B. M. Henry, A. P. Roberts, C. R. M. Grovenor, G. A. D. Briggs, A. P. Sutton, T. Miyamoto, Y. Tsukahara, N. Takeda, R. J. Chater, *Thin Solid Films* **2001**, *397*, 176.

[233] J. E. Mark, "*Polymer Data Handbook"*, Oxford University Press, Oxford, 2009.

[234] I. Baxter, "Advanced Resistance Deposition Technology for Productive Roll Coating", Society of Vacuum Coaters - 36th Annual Technical Conference Proceedings, 2011, 1993197.

[235] H. Jung, C. H. Jang, I. S. Yeo, T.-H. Song, *International Journal of Heat and Mass Transfer* **2013**, *56*, 436.

[236] C. Charton, N. Schiller, M. Fahland, A. Hollander, A. Wedel, K. Noller, *Thin Solid Films* **2006**, *502*, 99.

[237] C. A. Phillips, *International Journal of Food Science & Technology* **1996**, *31*, 463.

[238] S. Bhattacharya, R. Tummala, *Microelectronics Journal* **2001**, *32*, 11.

[239] D. Paul, L. Robeson, *Polymer* **2008**, *49*, 3187.

[240] T. Ebina, F. Mizukami, *Advanced Materials* **2007**, *19*, 2450.

[241] E. Jamieson, A. Windle, *Journal of Materials Science* **1983**, *18*, 64.

[242] A. Roberts, B. Henry, A. Sutton, C. Grovenor, G. Briggs, T. Miyamoto, M. Kano, Y. Tsukahara, M. Yanaka, *Journal of Membrane Science* **2002**, *208*, 75.

[243] K. Kalaitzidou, H. Fukushima, L. T. Drzal, *Carbon* **2007**, *45*, 1446.

[244] G. P. Carwford, "*Flexible Flat Panel Displays*", John Wiley & Sons, Ltd., Hoboken, NY, 2005.

[245] D. A. Hagen, C. Box, S. Greenlee, F. Xiang, O. Regev, J. C. Grunlan, *Rsc Advances* **2014**, *4*, 18354.

[246] F. M. Xiang, P. Tzeng, J. S. Sawyer, O. Regev, J. C. Grunlan, *Acs Applied Materials & Interfaces* **2014**, *6*, 6040.

[247] R. Rajasekar, N. H. Kim, D. Jung, T. Kuila, J. K. Lim, M. J. Park, J. H. Lee, *Composites Science and Technology* **2013**, *89*, 167.

[248] K. C. Krogman, J. L. Lowery, N. S. Zacharia, G. C. Rutledge, P. T. Hammond, *Nature Materials* **2009**, *8*, 512.

[249] A. J. Mateos, A. A. Cain, J. C. Grunlan, *Industrial & Engineering Chemistry Research* **2014**, *53*, 6409.

[250] J. B. Johnson, A. Pinto, "Ammonia synthesis process", US Patent 4695442, Imperial Chemical Industries Ltd., 1987.

[251] J. Woodtli, R. Kieselbach, *Engineering Failure Analysis* **2000**, *7*, 427.

[252] R. B. Gupta, "Hydrogen Fuel", CRC Press, Boca Raton, Florida, 2008, p. 451.

[253] L. Schlapbach, A. Zuttel, *Nature* **2001**, *414*, 353.

[254] P. P. Edwards, V. L. Kuznetsov, W. I. F. David, N. P. Brandon, *Energy Policy* **2008**, *36*, 4356.

[255] W. G. Bley, *Vacuum* **1993**, *44*, 627.

[256] H. D. Burger, "Method of leak testing a test container with a tracer gas", US Patent 4984450 A, Alcatel Cit, 1991.

[257] P. Jönsson, T. Eagar, J. Szekely, *Metallurgical and Materials Transactions B* **1995**, *26*, 383.

[258] J. E. Huheey, E. A. Keiter, R. L. Keiter, O. E. Medhi, *Pearson Education India* **2006**, *10*, 364.

[259] A. Cho, *Science* **2009**, *326*, 778.

[260] D. A. Shea, D. Morgan, "The helium-3 shortage: Supply, demand, and options for Congress", Congressional Research Service, Library of Congress, 2010.

[261] M. Linner, *ChemMatters* **1985**, 4.

[262] S. Zhang, "United States extends life of helium reserve", Nature News, 2013, *10*, 647.

[263] K. McDaniels, R. Downs, H. Meldner, C. Beach, C. Adams, *Cubic Tech Corp* **2009**, 1, 97.

[264] L. W. McKeen, "*Permeability properties of plastics and elastomers"*, William Andrew, Norwich, NY, 2011, p. 67.

[265] EVAL, "Hydrogen Fuel Cell Systems", Kuraray Co., 20071.

[266] S. Sinha Ray, M. Okamoto, *Progress in polymer science* **2003**, *28*, 1539.

[267] C. Tsai Boh, A. Wachtel James, "Barrier Properties of Ethylene-Vinyl Alcohol Copolymer in Retorted Plastic Food Containers", in *Barrier Polymers and Structures*, American Chemical Society, Washington, D.C., 1990, p. 192.

[268] W.-S. Jang, I. Rawson, J. C. Grunlan, *Thin Solid Films* **2008**, *516*, 4819.

[269] P. Tzeng, E. L. Lugo, G. D. Mai, B. A. Wilhite, J. C. Grunlan, *Macromolecular Rapid Communications* **2015**, *36*, 96.

[270] H. Czichos, T. Saito, L. Smith, L. R. Smith, "*Springer Handbook of Materials Measurement Methods"*, Springer, Berlin, Heidelberg, 2006, p. 106.

[271] G. Ladam, P. Schaad, J. C. Voegel, P. Schaaf, G. Decher, F. Cuisinier, *Langmuir* **1999**, *16*, 1249.

[272] E. H. H. Jamieson, A. H. Windle, *Journal of Materials Science* **1983**, *18*, 64.

[273] A. Arora, G. W. Padua, *Journal of Food Science* **2010**, *75*, R43.

[274] H. Wang, L. Z. Yang, Q. Chen, *Plasma Science & Technology* **2014**, *16*.

[275] Z. Liu, Z. H. Sun, X. X. Ma, C. L. Yang, *Packaging Technology and Science* **2013**, *26*, 70.

[276] K. Mueller, C. Schoenweitz, H. C. Langowski, *Packaging Technology and Science* **2012**, *25*, 137.

[277] M. Kamp, J. Bartsch, S. Nold, M. Retzlaff, M. Horteis, S. W. Glunz, *Proceedings of the Siliconpv Conference* **2011**, *8*, 558.

[278] J. D. Affinito, M. E. Gross, C. A. Coronado, G. L. Graff, E. N. Greenwell, P. M. Martin, *Thin Solid Films* **1996**, *290*, 63.

[279] Y. Leterrier, *Progress in Materials Science* **2003**, *48*, 1.

[280] K. K. Mokwena, J. Tang, *Critical Reviews in Food Science and Nutrition* **2012**, *52*, 640.

[281] B. C. Tsai, J. A. Wachtel, "*Barrier Properties of Ethylene Vinyl Alcohol Copolymer in Retorted Plastic Food Containers"*, Amer Chemical Soc, Washington, D.C., 1990, p. 192.

[282] S. G. Prolongo, R. Moriche, A. Jimenez-Suarez, M. Sanchez, A. Urena, *European Polymer Journal* **2014**, *61*, 206.

[283] D. Kim, H. Kwon, J. Seo, *Polymer Composites* **2014**, *35*, 644.

[284] K. S. Novoselov, A. K. Geim, S. V. Morozov, D. Jiang, M. I. Katsnelson, I. V. Grigorieva, S. V. Dubonos, A. A. Firsov, *Nature* **2005**, *438*, 197.

[285] S. Stankovich, D. A. Dikin, G. H. B. Dommett, K. M. Kohlhaas, E. J. Zimney, E. A. Stach, R. D. Piner, S. T. Nguyen, R. S. Ruoff, *Nature* **2006**, *442*, 282.

[286] C. Lee, X. D. Wei, J. W. Kysar, J. Hone, *Science* **2008**, *321*, 385.

[287] X. Zhao, Q. H. Zhang, D. J. Chen, P. Lu, *Macromolecules* **2010**, *43,* 2357.

[288] A. A. Balandin, S. Ghosh, W. Z. Bao, I. Calizo, D. Teweldebrhan, F. Miao, C. N. Lau, *Nano Letters* **2008**, *8,* 902.

[289] D. Li, M. B. Muller, S. Gilje, R. B. Kaner, G. G. Wallace, *Nature Nanotechnology* **2008**, *3*, 101.

[290] M. J. McAllister, J. L. Li, D. H. Adamson, H. C. Schniepp, A. A. Abdala, J. Liu, M. Herrera-Alonso, D. L. Milius, R. Car, R. K. Prud'homme, I. A. Aksay, *Chemistry of Materials* **2007**, *19*, 4396.

[291] M. B. Avinash, K. S. Subrahmanyam, Y. Sundarayya, T. Govindaraju, *Nanoscale* **2010**, *2*, 1762.

[292] G. Laufer, C. Kirkland, A. B. Morgan, J. C. Grunlan, *ACS Macro Letters* **2013**, *2*, 361.

[293] W. S. Jang, J. C. Grunlan, *Review of Scientific Instruments* **2005**, *76*, 4.

[294] P. Tzeng, C. R. Maupin, J. C. Grunlan, *Journal of Membrane Science* **2014**, *452*, 46.

[295] ISO Standard 15105-2, Plastics - Film and sheeting - Determination of gas-transmission rate - Part 2: Equal-pressure method. International Organization for Standardization, Geneva, Switzerland, **2003**.

[296] ASTM Standard F2476-05, Test Method for the Determination of Carbon Dioxide Gas Transmission Rate (CO_2TR) Through Barrier Materials Using An Infrared Detector. ASTM International, West Conshohocken, PA, **2005**, DOI: 10.1520/F2476-05.

[297] A. S. Michaels, *Industrial & Engineering Chemistry* **1965**, *57*, 32.

[298] L. Kai, "*Proceedings of the 2009 International Conference on Chemical, Biological and Environmental Engineering, CBEE 2009, Singapore, 9-11 October 2009*", World Scientific, 2009.

[299] R. A. Lusiana, D. Siswanta, Mudasir, T. Hayashita, *International Journal of Chemical Engineering and Applications* **2013**, *4*, 229.

[300] R. W. Baker, E. L. Cussler, W. Eykamp, W. J. Koros, R. L. Riley, R. H. Strathman, "*Membrane separation systems"*, Noyes Data Corporation; Park Ridge, NJ, 1991; pp 76.

[301] A. K. Pabby, S. S. H. Rizvi, A. M. S. Requena, "*Handbook of Membrane Separations"*, CRC Press; Boca Raton, FL, 2009; pp 62.

[302] S. K. Gupta, S. N. Sinha, A. K. Agarwal, *Indian Journal of Chemical Technology* **1994**, *1*, 135.

[303] R. Xing, W. S. W. Ho, *Journal of Membrane Science* **2011**, *367*, 91.

[304] N. Hallale, F. Liu, *Advances in Environmental Research* **2001**, *6*, 81.

[305] D. C. Elliott, *Energy & Fuels* **2007**, *21*, 1792.

[306] E. Jochem, E. Schirrmeister, "Potential economic impact of fuel cell technologies", in *Handbook of Fuel Cells*, John Wiley & Sons; Hoboken, NJ, 2010; pp105.

[307] N. W. Ockwig, T. M. Nenoff, *Chemical Reviews* **2010**, *110*, 2573.

[308] B. D. Freeman, *Macromolecules* **1999**, *32*, 375.

[309] S. M. Saufi, A. F. Ismail, *Carbon* **2004**, *42*, 241.

[310] M. A. Snyder, M. Tsapatsis, *Angewandte Chemie-International Edition* **2007**, *46*, 7560.

[311] M. Shah, M. C. McCarthy, S. Sachdeva, A. K. Lee, H. K. Jeong, *Industrial & Engineering Chemistry Research* **2012**, *51*, 2179.

[312] H. M. El-Kaderi, J. R. Hunt, J. L. Mendoza-Cortes, A. P. Cote, R. E. Taylor, M. O'Keeffe, O. M. Yaghi, *Science* **2007**, *316*, 268.

[313] B. J. Hinds, N. Chopra, T. Rantell, R. Andrews, V. Gavalas, L. G. Bachas, *Science* **2004**, *303*, 62.

[314] N. B. McKeown, P. M. Budd, *Macromolecules* **2010**, *43*, 5163.

[315] M. Carta, R. Malpass-Evans, M. Croad, Y. Rogan, J. C. Jansen, P. Bernardo, F. Bazzarelli, N. B. McKeown, *Science* **2013**, *339*, 303.

[316] H. B. Park, C. H. Jung, Y. M. Lee, A. J. Hill, S. J. Pas, S. T. Mudie, E. Van Wagner, B. D. Freeman, D. J. Cookson, *Science* **2007**, *318*, 254.

[317] D. A. Olson, L. Chen, M. A. Hillmyer, *Chemistry of Materials* **2008**, *20*, 869.

[318] A. J. Nolte, R. E. Cohen, M. F. Rubner, *Macromolecules* **2006**, *39*, 4841.

[319] A. J. Nolte, N. D. Treat, R. E. Cohen, M. F. Rubner, *Macromolecules* **2008**, *41*, 5793.

[320] T. Yamamoto, T. Kanda, Y. Nishihara, T. Ooshima, Y. Saito, *Journal of Polymer Science Part B-Polymer Physics* **2009**, *47*, 1181.

[321] V. A. Kusuma, B. D. Freeman, M. A. Borns, D. S. Kalika, *Journal of Membrane Science* **2009**, *327*, 195.

[322] H. Q. Lin, E. Van Wagner, B. D. Freeman, L. G. Toy, R. P. Gupta, *Science* **2006**, *311*, 639.

[323] R. D. Raharjo, H. Lin, D. E. Sanders, B. D. Freeman, S. Kalakkunnath, D. S. Kalika, *Journal of Membrane Science* **2006**, *283*, 253.

[324] S. L. Liu, L. Shao, M. L. Chua, C. H. Lau, H. Wang, S. Quan, *Progress in Polymer Science* **2013**, *38*, 1089.

[325] L. Li, J. T. Liu, Z. J. Ren, S. K. Yan, *Chinese Journal of Polymer Science* **2014**, *32*, 1199.

[326] P. Vukusic, J. R. Sambles, *Nature* **2003**, *424*, 852.

[327] A. J. Nolte, M. F. Rubner, R. E. Cohen, *Langmuir* **2004**, *20*, 3304.

[328] R. A. McAloney, M. Sinyor, V. Dudnik, M. C. Goh, *Langmuir* **2001**, *17*, 6655.